CORRIGENDA to thesis OPTICAL DIAGNOSTICS IN COMBUSTION SYSTEMS by M. J. R. Schwar, 1970

P6L8&9 reword: distribution of the molecules' energy between their translational motion and their internal degrees of freedom. The other is...

P16L4 change $(\phi_c+\phi_o+\phi_r)$ to: $(\phi_c-\phi_o+\phi_r)$

P22L9 insert ref. no. 7 immediately after coefficients.

P23L13 change serverely to: severely.

P33L7 change grain to: granularity.

P38L17 changefinite grain to: irregular.

P38L19 change circumstanstances to: circumstances.

P40L11 delete: quite.

P44L17 change $30 m.s^{-1}$ to: $300 m.s^{-1}$.

P47L23&25 change $+\theta$ to: $-\theta$.

P49L1 change 4.4 to 3.4 and 4.5 to 3.5.

P62L23 insert after fringes: (see equation 3.17b).

P72L8 change ν_1 to: ν_r.

P72L15 change to its direction to: to the direction.

P75L12 insert after made:,n has been defined on page 64,...

P76L7 change accurate to: precise.

P76L9 change error to: uncertainty.

P81L12 change object to: space.

P81L15 change space to: object.

P86L18 add after form: high intensity fringes...

P92L16 add after 0.04: $x10^4$...

P110L6 change p_o to: $\hat{p}_o$.

P114L3 delete: It is seen that.

P116L18 change practical limit to: limit to the minimum area of contact that can be used in practice...

P117L8, P123L14, P143L10 change dependant to: dependent.

P124L9 change the main requirement is to: it is useful.

P130L8 delete progressive.

P132L8 addafter background: , and by adjusting the position of the reflector plate the intensity of the progressive and standing sound waves could be made the same.

P132L21 change Figure 5.7 to: Figure 5.8.

P140L1 change nomimally to: nominally.

P156L8 change could to: cold.

P159L24 replace has by: appears to have[48] (but see Simpson and Chandler, Proc.Roy.Soc.Lond.A.317,265,1970)

P162L9 change voloumatric to: volumetric.

P162L23 add after temperature: in the case of argon and equation 5.9 in the case of air.

P180L12 change interferogram to: interferometer.

P170TABLE10 change 770 to 745 and 863 to 832.

P184L10 add to beginning of sentence: The exposure of...

OPTICAL DIAGNOSTICS IN COMBUSTION SYSTEMS

A thesis submitted for the degree

of Doctor of Philosophy of the

University of London

in the faculty of Science

by

M. J. R. SCHWAR, M. Sc., A. Inst. P.

Department of Chemical Engineering
and Chemical Technology,
IMPERIAL COLLEGE,
Prince Consort Road,
London, S.W.7

1970

OPTICAL DIAGNOSTICS IN COMBUSTION SYSTEMS

by

M. J. R. Schwar

A B S T R A C T

Because of the continuing need in combustion research for improved methods of investigating temperature, composition and velocity distributions the basis of a number of new optical diagnostic methods are proposed. The advent of lasers has made developments in this field particularly fruitful.

The construction, properties and use of holographic replicas of conventional optical components have been investigated. Holographic optical components may be a useful aid to optical diagnostic methods on account of their relative cheapness and large sizes possible.

A method of measuring the velocity of pure phase as well as solid objects and which combines the Doppler effect with schlieren and interferometric techniques is developed. Doppler shifts are measured using a beat frequency method and it is shown how the beat frequency signal may be interpreted as an interference fringe pattern moving across the front of a photodetector.

A combined optical and ultra-sonic method of gas diagnostics is proposed and described that is based on deducing the velocity of sound from a shadowgram of the pressure fronts of a high

frequency sound wave as it passes through a gas. The method has been used to measure gas temperatures up to 1000°K in systems in which the gas composition was known.

Another diagnostic aid that has been developed is a particularly simple form of interferometer. By using holographic methods it can form interferograms free from boundary effects even, for example, when windows of poor optical quality are in the test space.

All these methods have been tested experimentally and their limitations assessed.

CONTENTS

ABSTRACT 1

ACKNOWLEDGEMENTS 5

1. INTRODUCTION 6

2. HOLOGRAPHIC OPTICAL ELEMENTS

- 2.1. Intoduction 11
- 2.2. The holographic process 13
- 2.3. Size limitations 17
- 2.4. Making lens holograms 24
- 2.5. Using lens holograms 36
- 2.6. Conclusions 38

3. THE 'DOPPLER' METHOD OF VELOCITY MEASUREMENT

- 3.1. Introduction 42
- 3.2. Doppler shift equations 47
- 3.3. Interference between two waves of different frequency 53
- 3.4. Theory of the Doppler interferometer 59
- 3.5. Practical Doppler interferometers 69
- 3.6. Conclusions 73

4. 'DOPPLER' VELOCITY MEASUREMENTS

- 4.1. Introduction 77
- 4.2. Apparatus 77
- 4.3. Linear track velocity measurement of a radially ruled rotating grating 83
- 4.4. Velocity measurements of moving rods and discs 86
- 4.5. Velocity of sound measurement 91
- 4.6. Measurement of the velocity of a moving flame 92
- 4.7. Conclusions 96

5. THE ULTRA-SONIC METHOD OF GAS DIAGNOSTICS

5.1. Introduction 99
5.2. Propagation of sound waves in gases 101
5.3. Refractive index variations in an acoustic beam 107
5.4. The transducer 111
5.5. Visualization of sound waves 126
5.6. Summary 142

6. ULTRA-SONIC MEASUREMENTS

6.1. Introduction 144
6.2. The interaction problem 145
6.3. Solution of interaction problem 151
6.4. Temperature measurements in non-absorbing gases 160
6.5. Conclusions 172

7. SUBTRACTIVE INTERFEROMETRY

7.1. Introduction 173
7.2. Principles of subtractive interferometry 175
7.3. Design and performance of interferometer 187
7.4. Applications of subtractive interferometry 197
7.5. Conclusions 206

8. SUMMARY, POTENTIAL DEVELOPMENTS AND APPLICATIONS 208

APPENDIX 1 214

Relaxation frequency v. temperature for carbon dioxide, carbon monoxide, methane, oxygen and nitrogen.

APPENDIX 2 215

Heat transfer coefficient v. temperature and gas flow velocity for 36 swg in air and argon.

APPENDIX 3 217

List of symbols

REFERENCES 222

A C K N O W L E D G E M E N T S

I should like to thank Professor F. J. Weinberg for instilling in me an interest in combustion physics and in particular the optics of flames, for his supervision and guidance and for the numerous stimulating discussions we have had during the course of my researches. Thanks are also due to Dr. A. R. Jones who has shown much interest in my work and made many helpful suggestions.

I wish also to thank Professor A. R. Ubbelohde for all the interest he has shown in the progress of the research.

Finally I should like to acknowledge the various members of the workshop and electronics laboratory for their help and assistance in building and designing apparatus, and to Mr. L. Moulder for his photographic services and advice.

CHAPTER 1

INTRODUCTION

The subject of chemical kinetics in reacting gas flows has developed along two different paths. One involves studies at a molecular level and is concerned with the identification of intermediaries, including radicals, which are formed during reaction, the energy required to dissociate molecules, and the distribution of energy between the translational and various rotational, vibrational and excitational states. The other is more concerned with the macroscopic investigation of temperature, composition and velocity distributions, and overall heat release rates. There are numerous experimental techniques that may be used to obtain quantitative information on the magnitude of these various parameters. For present purposes they may be conveniently divided into optical and non-optical methods.

Optical diagnostic methods may be classified according to whether the observed light originates from within the system or from an external source. Examples of the former are emission spectroscopy and pyrometry. Gaydon[1], and Gaydon and Wolfhard[2] describe how spectroscopic methods may be used in combustion research, while Hottel and Sarofim[3], and Chandrasekhar[4] review the problems involved in radiative heat transfer studies. Examples in which the observed light originates from an external source are absorption spectroscopy, particle scattering including flow

visualisation by the particle track method, schlieren and interferometric methods. A review of light scattering by particles in flames has been given by Jones and Schwar[5], and Weinberg[6] discusses in detail the theory and practice of the schlieren and interferometric methods of studying combustion systems. Schwar and Weinberg[7] have reviewed numerous new optical methods that have become possible with the ready availability of laser light sources.

Non-optical methods generally necessitate the introduction of a solid body into the system being studied. Fristrom and Westenberg[8] have reviewed the whole subject of flame diagnostics and describe in detail the different methods that have been used including sampling probes, thermocouples, Pitot-tubes and electrical probes.

The perturbation caused by using optical diagnostic methods are usually insignificant in comparison with non-optical methods. They also have the advantage of being able to provide, in many cases, a permanent and instantaneous photographic record of the quantity being measured. There have not been many systematic comparisons between optical and non-optical diagnostic methods. This is partly due to the fact that the accuracy of the various methods are not generally comparable over the region in which they could both be applied. Bonne, Grewer and Wagner[9] have compared spectroscopic and thermocouple temperature measurements in a low pressure (8 torr) stoichiometric methane-oxygen flame and obtained agreement to within 20°C for temperatures greater than 1500°K. Their spectroscopic temperature determinations were made on the 0-0

OH absorption bands around 3064Å. Although the first comparison between a deflection mapping method and a thermocouple measurement of the temperature distribution within a slow burning, flat hydrogen-nitrogen-oxygen flame at atmospheric pressure, by Dixon-Lewis and Isles[10] was inconclusive a later study[11] by the same authors suggested that the optical method was the more reliable.

The tendency in combustion to work at ever higher temperatures and velocities (for example in augmented flames and standing detonations) has accentuated the need for new and improved methods of diagnostics. Fortunately the advent of the laser has helped to remedy this need. Their extreme brightness enables them to outshine highly luminous events, the possibility of Q-switching allows the photography of extremely rapid transient events, and their excellent coherency permits the development of a whole new range of optical interference methods. Three of the four major advances in optical diagnostics described in this thesis would not be possible without a light source having the excellent spatial coherency of a uniphase helium-neon gas laser. The fourth, although not relying on the special properties of a laser light source, would have its range of application considerably extended if, for example, a Q-switched ruby laser were used instead of the argon jet spark light source.

The advances described in this thesis are concerned with improvements in instrumentation and with the development of new diagnostic methods involving velocity measurements of one sort or another.

It is shown how conventional optical components such as lenses

can be replaced by their holographic equivalents. These have advantages over conventional components both from the point of view of cheapness and in relative ease of manufacture. They are, however, less efficient. Nevertheless if they are used in conjunction with a very bright light source they could, in certain circumstances, be more convenient than lenses or mirrors. One instance would be in optical systems used for studying unconfined explosions where components are likely to become damaged during the experiment.

Another advance in optical instrumentation that is described is the design and performance of a particularly simple interferometer. It is shown that by using holographic techniques the instrument can be used to obtain aberration free 'infinite fringe' interferograms and hence eliminate the problem of residual fringes that are usually present in other more conventional interferometers.

Normally optical diagnostic methods for measuring the velocity of moving phase objects such as propagating flame fronts, detonation fronts, or shock waves involve using some form of visualization in conjunction with high speed cine or steak photography. Here a completely new method of measuring the velocity of phase objects is described. It has the added advantage of being applicable to moving solid objects. The method depends on using a schlieren system to select the angle through which a transluminating light beam is deflected. The angle of deflection is accurately defined by using a suitably designed selective schlieren blind, and the shift in frequency is measured by the method of beats using an interference technique.

The limitations of the method lie in the required accuracy of the velocity measurement $\Delta u/u$ and the restrictions in the distance w_o over which the velocity measurement is made. It is shown that the product $w_o(\Delta u/u)$ is of the order of λ/θ, where λ is the wavelength of the transluminating light and θ is the angle of deflection.

Another diagnostic method that is described is based on the instantaneous photography of high frequency ultra-sonic waves using a shadow method of visualization. Temperature measurements have been made using this technique up to almost 1000°K and they agree favourably with thermocouple measurements. The method has an advantage over other purely optical diagnostic methods in that by employing sound waves the markings are particularly easy to interpret and correspond to the positions of the pressurefronts ; it does not require any inversion procedure as is necessary when interpreting, for example, interferograms of axially symmetric systems.

A list of the more important symbols used in the text is given in Appendix 3.

CHAPTER 2

HOLOGRAPHIC OPTICAL ELEMENTS

2.1. INTRODUCTION.

The simplicity and cheapness of construction of holographic optical elements makes them a possible substitute for lenses or even mirrors. The great advantage of this in combustion research is that expensive schlieren lenses may be replaced by their holographic equivalent. Applications in which this facility is highly desirable are the study of hot and explosive systems which, for one reason or another, need to be in close proximity to otherwise costly optical components. The possibility of making very large holographic copies of lenses makes them particularly suited for studying combustion processes occupying large test spaces.

It is demonstrated that the wavefront emerging from a lens can be stored as a hologram on a plane photographic plate and that because of the inherent focusing properties of a hologram the curvature of the reconstructed wavefront can be controlled by varying the curvature of the illuminating wavefront - see Figure 2.1 . In other words a hologram of a lens not only contains the information about the original wavefront emerging from the lens, but it also behaves like a lens and can therefore be used in the same way as a conventional imaging device. It differs from a lens or mirror in the way in which changes in wavefront curvature are brought about, i.e. by diffraction rather than by refraction or reflection.

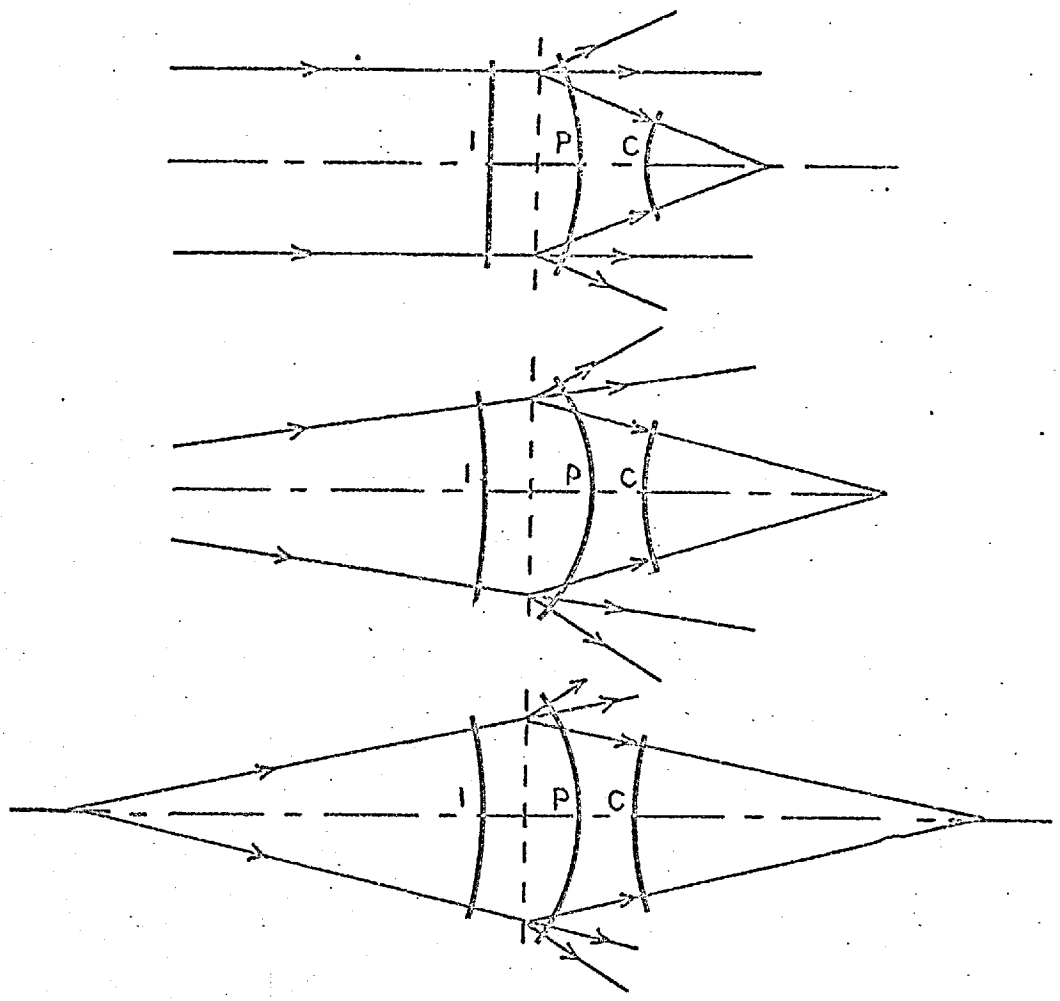

Focusing properties of a point hologram showing the change in curvature of the primary, P, and conjugate, C, waves with change in curvature of the incident wave, I.

FIGURE 2-1

The magnitude of the various disturbing effects introduced during the recording and illumination of a lens hologram are assessed together with an examination of the aberrations that may arise during its use. It is shown that as far as their application to schlieren systems are concerned these perturbing effects are usually quite small. It is also shown that lens holograms can be made very easily using either a Mach-Zehnder interferometer or the very much simpler type of interferometer described in Chapter 7. Examples are given illustrating the use of lens holograms for aiding in the visualization of both phase and solid objects.

2.2. THE HOLOGRAPHIC PROCESS.

2.2.1. Introduction.

The principle of reconstructing wavefronts by the process known as holography was first proposed and demonstrated by Gabor[12] in 1948. Lieth and Upatnieks[13] revived general interest in the subject during the sixties and the theory of holography is now well established[14,15,16].

The first step of the process involves recording the phase distribution of an object wave on a photographic plate by interference with a reference wave. When the processed plate, which is now refered to as a hologram, is illuminated by the original reference wave only, part of the light transmitted by the plate has a phase distribution identical to that which radiated from the original object. This reconstructed wave is known as the primary wave. There is also another wave, known as the conjugate wave, that forms an image of the object at a distance beyond the hologram equal to the distance

between the object and original recording plane.

When the wave illuminating the hologram has a curvature that is different from the original reference wave there is a change in direction of propagation of the primary and conjugate waves[17]. These changes in direction are most conveniently expressed in terms of the focal length of the hologram. Below a lens hologram equation is derived that is analogous to the well known lens and mirror equations relating object and image distances to the focal length of the optical element being considered.

2.2.2. The basic hologram equation.

In this section it is convenient to assume the focal region of a lens to be a point. This then allows one to consider that the wavefront emerging from a lens is part of a perfect sphere. The analysis given here, therefore, strictly applies to a point hologram. However, this does not matter as it is a simple matter to extend the final result to a lens hologram by considering the Airy disc at the focus of a lens to be simply a large collection of points.

The shape of a reconstructed wavefront can be described in terms of its phase distribution over the plane of the hologram. It will be shown how this phase distribution is related to the phase distributions of the reference and illuminating waves.

Using Cartesian coordinates let the hologram be recorded in the plane $z = 0$. The object point source at (x_o, y_o, z_o) and reference point source at (x_r, y_r, z_r) produce complex amplitude distributions $O(x,y)$ and $R(x,y)$ in the recording plane. Reconstruction is obtained using illumination from a point source at (x_c, y_c, z_c) producing an amplitude distribution $C(x,y)$ at the hologram. If the phase

distributions of the object, reference, and illuminating waves at the recording plane are respectively $\phi_o(x,y)$, $\phi_r(x,y)$, and $\phi_c(x,y)$ one may write

$$O = O_o \exp(j\phi_o) \qquad \ldots 1a$$

$$R = R_o \exp(j\phi_r) \qquad \ldots 1b$$

$$C = C_o \exp(j\phi_c) \qquad \ldots 1c$$

The resultant amplitude distribution at the recording plane is due to the combined effect of the object and reference waves so that the distribution in exposure, $E(x,y)$, over the photographic plate is given by

$$E(x,y) = (O + R)(O^* + R^*) \qquad \ldots 2$$

where the asterisk implies taking the complex conjugate. By operating on the linear portion of the plate's amplitude transmittance characteristic the resulting distribution of amplitude transmittance $T(x,y)$ of the hologram is given by

$$T(x,y) = k(O + R)(O^* + R^*) \qquad \ldots 3$$

The complex amplitude distribution transmitted by the hologram when illuminated by the reconstructing wave is therefore

$$A(x,y) = kC(O + R)(O^* + R^*) \qquad \ldots 4$$

Substituting equations 1 into equation 4 gives

$$\begin{aligned} A(x,y) = k \{ & C_o O_o^2 \exp(j\phi_c) + C_o R_o^2 \exp(j\phi_c) \\ & + C_o R_o O_o \exp(j(\phi_c + \phi_o - \phi_r)) \\ & + C_o R_o O_o \exp(j(\phi_c - \phi_o + \phi_r)) \}, \end{aligned} \qquad \ldots 5$$

which is the basic hologram equation. It is seen that the phase distributions of the last two terms are related to the original object wave - they are not, however, equal to it unless ϕ_c is made equal to ϕ_r.

2.2.3. Focusing properties of a point hologram.

The hologram theory proposed by Meier[18] can be used as a basis for deriving a lens hologram imaging equation. To a first order approximation $(\phi_c + \phi_o - \phi_r)$ and $(\phi_c + \phi_o + \phi_r)$ represent the phase distribution of spherical wavefronts. However, this is only an approximation and is exactly true only when $\phi_c = \phi_r$. When this does not hold aberrations always exist in the reconstructed wavefronts.

The phase distribution $(\phi_c + \phi_o - \phi_r)$ corresponds to the primary wave which has centre coordinates (X_p, Y_p, Z_p) given by

$$\frac{1}{Z_p} = \frac{1}{z_o} - \frac{1}{z_r} + \frac{1}{z_c} \qquad \ldots 6a$$

$$\frac{1}{X_p} = \frac{1}{Z_p}\left[\frac{x_o}{z_o} - \frac{x_r}{z_r} + \frac{x_c}{z_c}\right]^{-1} \qquad \ldots 6b$$

$$\frac{1}{Y_p} = \frac{1}{Z_p}\left[\frac{y_o}{z_o} - \frac{y_r}{z_r} + \frac{y_c}{z_c}\right]^{-1} \qquad \ldots 6c$$

The phase distribution $(\phi_c - \phi_o + \phi_r)$ corresponds to the conjugate wave and has centre coordinates (X_c, Y_c, Z_c) given by

$$\frac{1}{Z_c} = \frac{1}{z_c} - \frac{1}{z_o} + \frac{1}{z_r} \qquad \ldots 7a$$

$$\frac{1}{X_c} = \frac{1}{Z_c}\left[\frac{x_c}{z_c} - \frac{x_c}{z_o} + \frac{x_r}{z_r}\right]^{-1} \qquad \ldots 7b$$

$$\frac{1}{Y_c} = \frac{1}{Z_c}\left[\frac{y_c}{z_c} - \frac{y_o}{z_o} + \frac{y_r}{z_r}\right]^{-1} \qquad \ldots 7c$$

By analogy with the definition of the focal length of a lens an expression for the hologram's focal length can be found by locating the points corresponding to the centre of curvature of the reconstructed waves when the hologram is illuminated with a plane wave, i.e. by a point source at $z_c = \pm \infty$. The primary and conjugate

focal points, f_p and f_c, are therefore given by equations 6a and 7a by putting $z_c = +\infty$, and $Z_p = f_p$ and $Z_c = f_c$. It follows that the hologram's focal lengths are given by

$$\frac{1}{f_p} = \frac{-1}{f_c} = \frac{1}{z_o} - \frac{1}{z_r} = \pm \frac{1}{f} \qquad \ldots 8$$

If equation 8 is substituted into equation 6a and equation 7a and if Z_p and Z_c are considered as image distances v and z_c is the object distanceu the following equation is arrived at

$$\frac{1}{v} - \frac{1}{u} = \pm \frac{1}{f} \qquad \ldots 9$$

Thus a point hologram behaves exactly like a lens except that it simultaneously possesses a positive and negative focal length.

2.3. SIZE LIMITATIONS.

2.3.1. Introduction.

The sensitivity of a schlieren system depends on the diameter of the focal spot at the focus of the schlieren optical element. In the case of a lens hologram this spot size is determined by the effective dimensions of the hologram, the dimensions of the object, reference and illuminating sources, and by the aberrations of the lens hologram. The contribution that these various factors make to size of the focal spot of a lens hologram are examined below.

2.3.2. Diffraction limitations.

When an idealized lens hologram, i.e. a point hologram, is illuminated with a spherical wave the reconstructed waves are never perfectly spherical, even for an aberration free hologram, because of diffraction effects caused by the hologram's finite size. The effective diameter of a point hologram may be governed by the limiting

aperture during the recording or reconstructing process or by the resolving power of the recording medium. If a point hologram of effective radius r_h is illuminated by a plane wave the spot diameter s formed by the reconstructed wave is given by[14]

$$s = \frac{0.61 \lambda f}{r_h}, \qquad \ldots 10$$

where f is the focal length of the hologram and s is defined as the radius at which the first minimum in the Airy disc occurs.

If the reference and object beams completely fill the recording medium the effective size of the point hologram will then be determined by either the dimensions of the recording medium or by α, the maximum spatial frequency that the medium can faithfully record. Providing $r^2/2z_r^2$ and $r^2/2z_o^2 \ll 1$ the radius of the p^{th} bright fringe measured from the centre of the point hologram, having a focal length f, is given by

$$r_p^2 = 2\lambda pf. \qquad \ldots 11$$

The fringe separation Δr at a radius r is, therefore,

$$\Delta r = \frac{\lambda f}{r} \qquad \ldots 12$$

providing $\Delta r/r \ll 1$. The smallest Δr that an emulsion can resolve is $1/\alpha$ and so the maximum radius r_h up to which fringes can be recorded is[19]

$$r_h = \alpha \lambda f \qquad \ldots 13$$

When the spot size is emulsion limited and when the point hologram is illuminated by a plane wave the spot diameter is found by combining equations 10 and 13 to give

$$s = \frac{0.61}{\alpha} \qquad \ldots 14$$

Equation 14 gives the diameter of the focal spot corresponding to an ideal point object. In the case of a lens hologram the object is an Airy disc and this equation represents the additional spread brought about by the holographic process. If r_L is the radius of the lens (assumed to be perfect) the spot diameter at the focus of the lens hologram is

$$s = 0.61\lambda\left[\frac{f_L}{r_L} + \frac{f}{r_h}\right] \qquad \ldots 15$$

when the reference and reconstruction beams are planar. When the size of the hologram is limited by the width of the wavefront emerging from the lens $f_L/r_L = f/r_h$ and so the spot diameter becomes

$$s = 1.22\lambda\frac{f_L}{r_L} \qquad \ldots 16$$

where f_L and f are the focal lengths of the lens and the lens hologram respectively.

2.3.3. Source size.

So far it has been assumed that a hologram can be made by interfering the wave radiating from the object with a perfectly spherical reference wave, and that the reconstruction is obtained using a perfectly spherical illuminating wave. In pactice, however, both reference and illuminating sources have a finite size and this too contributes to the spread in the diameter of the focal spot formed by the reconstructed waves.

In the absence of other limiting effects the focal spot diameter formed by the reconstructed waves is of the order of the sum of the diameters of the reference and illuminating sources[15]. The diameter, s_r, of the focal spot formed by focusing a Gaussian laser beam of diameter 2w using a lens of focal length f_r is given by[20]

$$s_r = 0.63 \frac{\lambda f_r}{w} \qquad \ldots 17$$

If f_r/w is made much smaller than f_L/r_L the effect of a finite source size becomes negligible.

2.3.4. Source line-width.

When a light source of frequency ν has a finite line-width $\Delta\nu$ only a limited number of fringes $\nu/\Delta\nu$ can be recorded. Therefore, the finite line-width may determine the maximum radius of a point hologram. From equation 11, it follows that in the absence of other limiting factors this radius is given by

$$r_h = \left[2\lambda f \frac{\nu}{\Delta\nu}\right]^{\frac{1}{2}} \qquad \ldots 18$$

and, from equation 10 the spot size diameter formed when the hologram is illuminated with a plane wave is

$$s = 0.43 \left[\lambda f \frac{\Delta\nu}{\nu}\right]^{\frac{1}{2}} \qquad \ldots 19$$

A spread in the spot diameter also occurs during the reconstruction process whenever the illuminating source has a finite line-width. This spread increases with increase in the hologram's spatial frequency, i.e. with increase in the angle between the reference and object wave. If the maximum angle between these two waves is θ_m the spot size diameter in the absence of other limiting factors when a point hologram is illuminated by a plane wave is [15]

$$s = \frac{\Delta\nu}{\nu} f \sin\theta_m \qquad \ldots 20$$

Providing θ_m is not too large $\sin\theta_m \simeq \theta_m = r_h/f$. If the same source is used for the construction and reconstruction processes r_h is given by equation 18 and equation 20 then reduces to

$$s = 1.41\left[\lambda f \frac{\Delta\nu}{\nu}\right]^{\frac{1}{2}} \qquad \ldots 21$$

The total spread resulting from using a source of finite line-width in the constructing and reconstructing processes is given by the sum of equations 19 and 21, i.e.

$$s = 1.84\left[\lambda f \frac{\Delta\nu}{\nu}\right]^{\frac{1}{2}} \qquad \ldots 22$$

2.3.5. Hologram aberrations.

Whenever a hologram is illuminated by a wave having a curvature or angle of incidence different from that of the original reference wave the reconstructed wave will suffer from aberrations. Meier[7] has examined in some detail the aberrations produced by a hologram in terms of the phase difference Ψ between the reconstructed wavefront and a perfectly spherical aberration free wavefront.

From a practical point of view aberrations in a schlieren system will affect the size of the focal spot and the quality of the resulting record of the test space. According to Rayleigh's criterion for aberration free imagery the phase difference Ψ should not exceed $\frac{1}{2}\pi$ (see for example refs 21 and 22). Holder and North[23] have found from their practical experience that a phase difference of the order π is tolerable for most schlieren applications.

It follows from Meier's analysis that in the case of a point hologram Ψ increases with increasing radius and that if changes between the reference and illuminating beams occur in only one plane Ψ is given by

$$\Psi = \frac{2\pi}{\lambda}\left[-\frac{r^4}{8}S + \frac{r^3}{2}C - \frac{r^2}{2}A - \frac{r^2}{4}F + \frac{r}{2}D\right] \qquad \ldots 23$$

where S, C, A, F and D are the five coefficients for spherical, coma, astigmatism, field curvature and distortion aberration respectively.

If a point hologram is used to replace a schlieren lens in a parallel beam system the radius of curvature, z_c, of the illuminating beam is infinity. If this illuminating beam is inclined to the z-axis at an angle θ, and the coordinates of the point object and reference source are $(0,0,z_o)$ and $(0,0,z_r)$ respectively the five aberration coefficients reduce to the expressions tabulated in Table 1.

TABLE 1

Generalized aberration coefficients for a point hologram when illuminated by a parallel beam.

S	$-\frac{3}{z_o z_r}\left[\frac{1}{z_o}-\frac{1}{z_r}\right]$	C	$-\tan\theta\left[\frac{1}{z_o^2}-\frac{1}{z_r^2}\right]$
A	$\tan^2\theta\left[\frac{1}{z_o}-\frac{1}{z_r}\right]$	F	$\tan^2\theta\left[\frac{1}{z_o}-\frac{1}{z_r}\right]$

The distortion coefficient, D, is zero.

When the reference wave is plane S is zero and the dominant aberration is coma. On the other hand if the curvatures of the reference wave and illuminating wave are vastly different the dominant aberration is spherical. Table 2 lists the aberration coefficients when the radius of curvature of the reference wave is equal to infinity and to -2f for a point hologram illuminated by a parallel beam. The angle θ may be interpreted as representing the angle of deflection produced by the test object and is usually

sufficiently small for tanθ to be put equal to θ. Making this approximation and substituting these coefficients into

TABLE 2

Aberration coefficients for a point hologram illuminated by a parallel beam when the radius of curvature of the reference wave equals ∞ and -2f.

$z_r = \infty$		$z_r = -2f$	
S	0	S	$3/4f^3$
C	$-\tan\theta/f^2$	C	$-\tan\theta/2f^2$
A	$\tan^2\theta/f$	A	$\tan^2\theta/f$
F	$\tan^2\theta/f$	F	$\tan^2\theta/f$

equation 23 then gives

$$\phi_{z_r=\infty} = -\frac{2\pi}{\lambda}\frac{r^3\theta}{2f^2}\left[1 + \frac{3f\theta}{2r}\right] \qquad \ldots 24a$$

$$\phi_{z_r=-2f} = -\frac{2\pi}{\lambda}\frac{3r^4}{32f^3}\left[1 + \frac{8f\theta}{3r} + \frac{8\theta^2f^2}{r^2}\right] \qquad \ldots 24b$$

For small deflections $f\theta/r \ll 1$. Therefore the radius for which the total phase aberration is less than π is given in these two cases by

$$r \leqslant \left[\frac{\lambda f^2}{\theta}\right]^{1/3}, \text{ for } z_r = \infty \qquad \ldots 25a$$

$$r \leqslant \left[\frac{16\lambda f^3}{3}\right]^{1/4}, \text{ for } z_r = -2f \qquad \ldots 25b$$

Equation 25b shows that when a parallel beam schlieren point hologram is made using a spherical reference and object wave of radius -2f and +2f respectively its maximum aperture must be serverely limited in order to keep the total phase aberration below π. On the

other hand equation 25a shows that if the point hologram is made using a plane reference wave and the angle of deflection produced by the test object is small, very large point holograms can be made whilst still keeping the total phase aberration less than π. The minimum angular deflection that can be detected is given by

$$\theta_{min} = \frac{0.61\lambda}{r_h} \qquad \ldots 26$$

Substituting this value of θ into equation 25a therefore gives an expression for the maximum radius of a point hologram having a total phase aberration less than π, i.e.

$$r_{h,max} = 1.28\, f \qquad \ldots 27$$

The magnitude of all these limiting factors are evaluated for a number of practical systems in the next section dealing with the experimental aspects of making lens holograms.

2.4. MAKING LENS HOLOGRAMS.

2.4.1. Introduction.

From the expressions just derived it would appear that the F-number ($f/2r_h$) of a lens hologram may have a value less than unity (see equations 13, 18 and 25a). However, this would generally require an object lens having a similar F-number and in practice a spherically corrected lens having an F-number less than unity is unlikely to be readily available. As diagnostic methods in combustion do not usually require optical components having such exotic dimensions only the properties and construction of holograms of conventional lenses will be considered. Before describing experimental details the order of magnitude of the quantities discussed in the previous section are

calculated.

The light source used was a Scientifica and Cook Electronics B16/2 helium-neon d.c. gas laser set to give a uniphase output of approximately 1mW. As the Doppler width of the neon line is of the order of 1.5×10^{9}Hz the output frequency, centred on 6328Å (i.e. 4.7×10^{14}Hz), consisted of about five axial modes each separated by about 3.0×10^{8}Hz. The beam emerging from the laser cavity had a radius of 0.3mm and was expanded using a microscope objective of 2cm focal length. From equation 17 it follows that the source has an effective diameter of 2.7×10^{-4}cm.

In Table 3 are listed the various numerical quantities associated with making lens holograms from two spherically corrected lenses using the above B16/2 laser. The maximum fringe frequency corresponding to the edge of the lens hologram can easily be recorded by a variety of commercially available photographic emulsions[7a]; in fact it is possible to record spatial frequencies in excess of 3×10^{4}cm^{-1} using suitable plates. Although the spread in the diameter of the lens hologram's focal spot due to the laser's finite line width is negligible it is not so from the point of view of its finite effective diameter. Apart from this it is seen that the hologram's focal spot diameter is at least equal to twice the diameter of the Airy disc of the lens and is independent of the focal length of the lens hologram.

These calculations show that sufficiently good quality lens holograms are a practical possibility and can be made using a B16/2 laser and commercially available photographic plates. Although a

TABLE 3

Three examples of the properties of lens holograms

Parameter	Focal length of lens hologram		
	20cm	50cm	173cm
Focal length of object lens	50cm	50cm	173cm
Radius of object lens	3cm	3cm	7.5cm
Spread in diameter of focal spot of lens hologram due to			
i) finite size of source used for object and reference beams	5.4μm	5.4μm	5.4μm
ii) diffraction by object lens	6.4μm	6.4μm	8.9μm
iii) diffraction by lens hologram	6.4μm	6.4μm	8.9μm
iv) finite line width of laser light source	0.04μm	0.1μm	0.3μm
Resultant diameter of focal spot of lens hologram	18.3μm	18.4μm	23.5μm
Maximum fringe frequency	948cm^{-1}	948cm^{-1}	687cm^{-1}
Maximum aberration free deflection	15.0mRd	5.8 mRd	4.5 mRd
Minimum detectable deflection	92μRd	37μRd	14μRd

lens hologram is not as perfect as the original object lens it can be used as a substitute for the lens and is capable of detecting deflections up to about 10mRd and is therefore suitable for using in a schlieren system for combustion diagnostics.

2.4.2. Mach-Zehnder method - plane reference wave.

To test the feasibility of the proposed method of making holographic replicas of lenses using a plane reference wave the Mach-Zehnder interferometer shown in Figure 2.2 was set up.

The beam from the 1mW B16/2 laser was expanded using a 2cm focal length microscope objective, L, and collimated by a 5ft focal length schlieren mirror M. The expanded beam was made parallel by adjusting the lateral position of the microscope objective until a single broad interference fringe was obtained as a result of interference between the beams reflected off the back and front faces of the first beam splitter. An object lens, L_o, was rigidly mounted in the test beam between M_1 and S_2 so that it brought the parallel test beam to a focus beyond S_2. By adjusting the orientations of the mirrors and beam splitters the axes of the test and reference beams could be made parallel or inclined to one another. The recording plate H was mounted perpendicular to the reference beam beyond the focal point P at a distance equal to the required focal length of the lens hologram. A stop was also placed beyond the object lens in the test beam to avoid light from the edge of the test beam passing around the object lens and falling onto the plate, H.

With the arrangement shown in Figure 2.2 the centres of the reference wavefront and the spherical wavefront emerging from the object lens coincide and the resulting hologram has the appearance

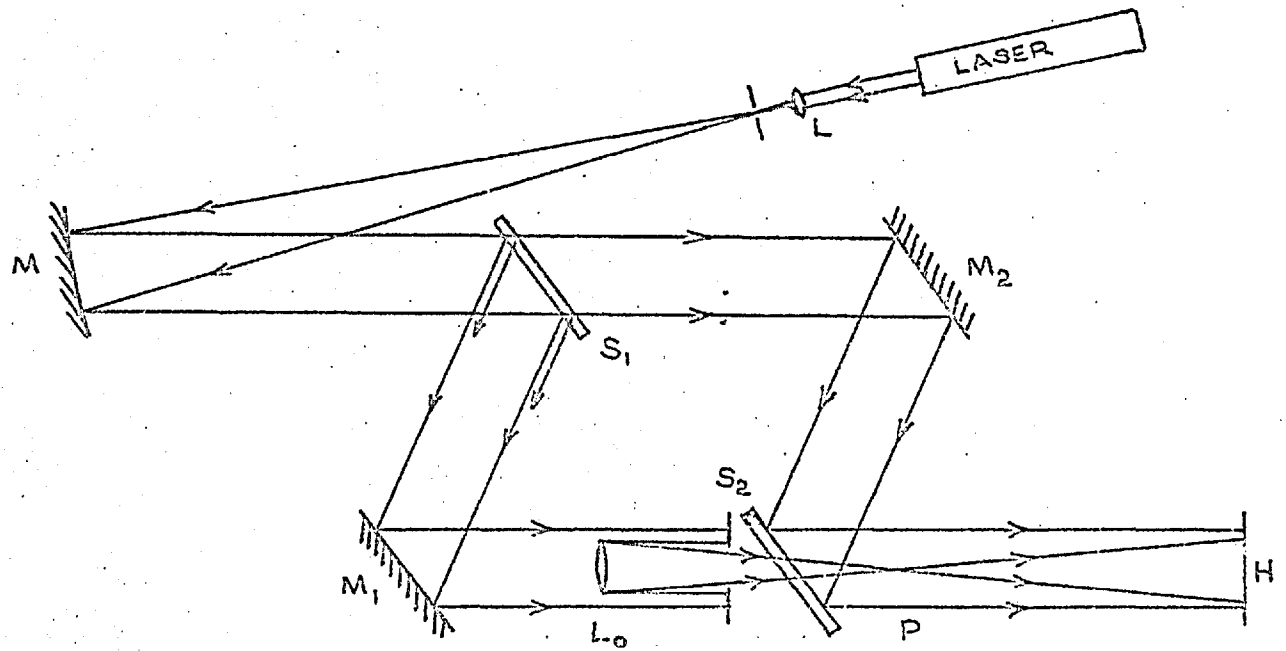

FIGURE 2-2

Optical arrangement for making lens holograms using a Mach-Zehnder interferometer. L, short focal length lens; M, M_1, M_2, mirrors; S_1, S_2, beam splitters, L_o, object lens; P, focal point; H, recording plane.

of a set of concentric interference fringes with its centre falling on the optic axis of the system. When the axes of the test and reference beams are inclined to one another the interference pattern still consists of a set of concentric fringes but now the centre of the circular fringe pattern no longer coincides with the centre of the test beam. If the angle of inclination between the two beams is $2r_L/f_L$ the centre of the concentric fringe pattern falls at the edge of the lens hologram.

A number of lens holograms were made with this arrangement using a 50cm focal length telescope objective as an object lens and Ilford R52 plates, having a quoted resolving power of 180 line pairs/mm, as a recording medium.

2.4.3. Simplified method - curved reference wave.

As the construction of a Mach-Zehnder interferometer of large aperture requires adjustable yet rigidly mounted large flat beam splitters and mirrors a simpler optical system for making lens holograms was designed.

Figure 2.3 illustrates the design of a simple system used for making off axis lens holograms. The beam splitter S was a thin wedge prism while the reflector M was the plane face of a plano-convex lens. The advantage of using these components was that it was particularly easy to remove the disturbing effects caused by back reflections. The method of mounting adopted was the same as that used in the interferometer described in Chapter 7. It is seen from the diagram that the object lens, L_o, provides both the object wave and the reference wave. If d is the separation between S and M, and

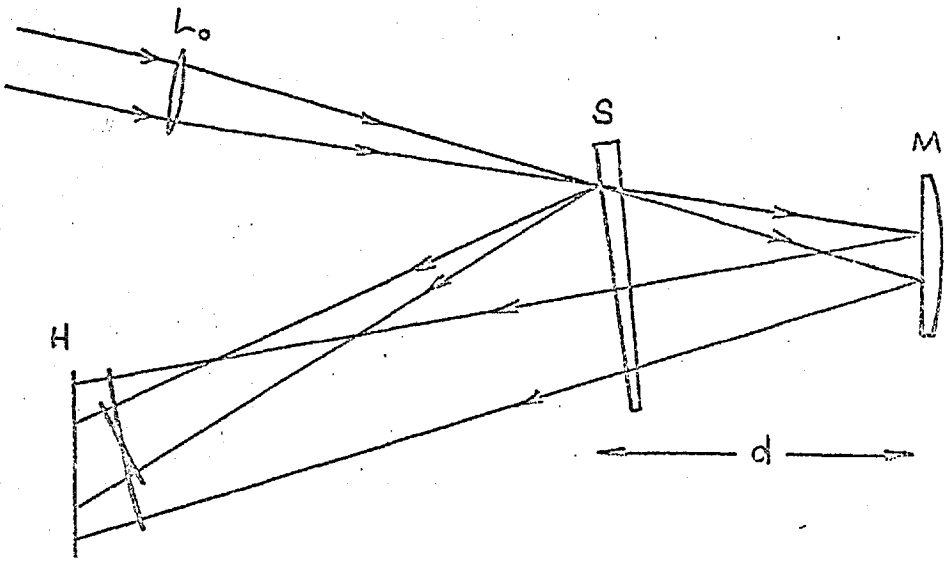

FIGURE 2-3

Optical arrangement for making lens holograms using a simplified form of interferometer. L_o, object lens; S, thin wedge beam splitter; M, plane glass reflector; H recording plane; d, separation between S and M.

the beam is brought to a focus on S, the focal length of the lens hologram so formed is

$$\pm \frac{1}{f} = \frac{1}{SH} - \frac{1}{SH + d} \qquad \ldots 28$$

Again using Ilford R52 plates and a 50cm focal length telescope objective as an object lens a number of lens holograms were made. By making d small it was possible to make holograms of very long focal length. It was also possible to make lens holograms having a focal length as small as 20cm. It was not possible to make lens holograms of focal length much smaller than this on account of the differences in intensity of the two interfering waves.

One consequence of this method of making lens holograms is that its F-number is always greater than that of the object lens. In general it is given by

$$F_h = F_L \left[1 + \frac{HS}{2d}\right] \qquad \ldots 29$$

When d = oo this reduces to the Mach-Zehnder case in which $F_h = F_L$.

2.4.4. Fringe structure.

Figure 2.4a shows how the separation between the fringes of a lens hologram becomes progressively less on moving out from the centre of the interference pattern. This photograph is a x5 enlargement of part of the original lens hologram recorded on an R52 plate using the optical system shown in Figure 2.3. The focal length is of the order of 6 meters and the maximum spatial frequency of the fringes corresponds to about 8/mm in the original.

Ideally the variation of transmittance of the plate should be proportional to the amplitude variations of the interference pattern incident on the plate during the recording process. Fortunately in

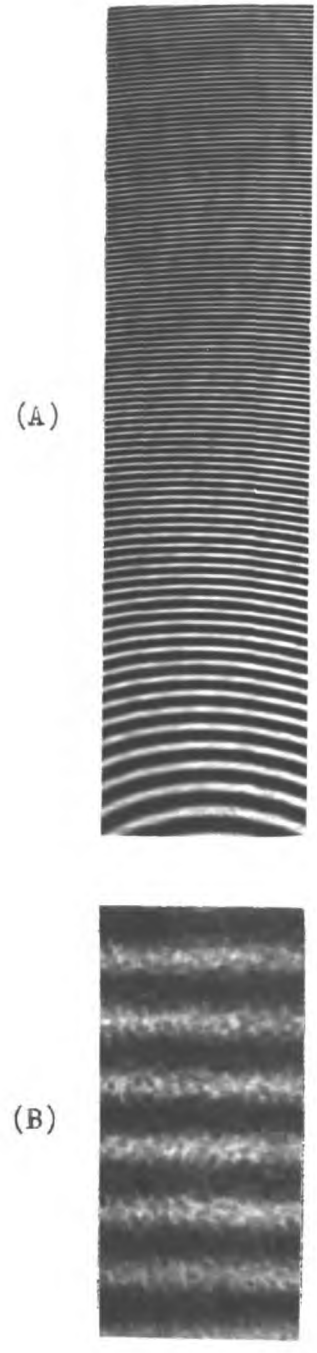

Fringe structure of a lens hologram. (A) part of a x5 enlargement of a 6meter f.l. lens hologram. (B) enlargement of 28 fringes/mm on Ilford R52 plate.

FIGURE 2.4

off axis systems it is not necessary[15] to process the plate precisely so as to fall on the linear portion of its amplitude transmittance characteristic[24] - it is more important to avoid excessive granularity and to keep the profile smooth. Figure 2.4b shows a x230 microscope enlargement of the fringe structure recorded on an Ilford R52 plate, corresponding to an original fringe frequency of about 28/mm. The grain is just becoming comparable to the fringe width and this represents perhaps the maximum spatial frequency that can be recorded on these plates without introducing too much irregularity into the profile of the fringes. Random irregularities of this nature result in unwanted scattered light, in the form of background speckle, being superimposed on the transmitted and reconstructed waves.

Operating on the non-linear part of the plate's amplitude transmittance characteristic results in a 'squaring up' of the fringe profile and theoretically[25] should manifest itself by the appearance of subsidiary foci. This has in fact been observed[19]. Examination of the light intensity along the optic axis of such a non-linearly processed lens hologram has revealed subsidiary foci at f/2, f/3, f/4, etc. This contrasts with the positions of the subsidiary foci for a Fresnel zone plate which occur at f/3, f/5, etc. Although the fraction of the incident light that is diffracted into the primary focus of a Fresnel zone plate is greater than for an ordinary lens hologram[25,26,27] the opaque rings of the Fresnel zone plate must mask out some of the information present in the illuminating wavefront and so produce a poorer quality image.

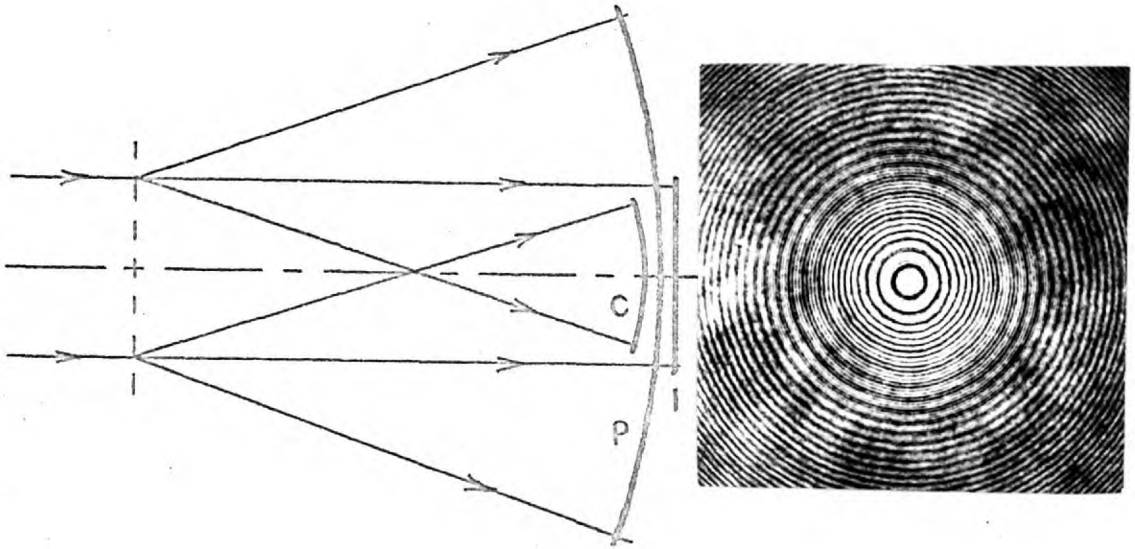

FIGURE 2-5

Interference pattern formed by the mutual interference of the transmitted illuminating wave, I, and the primary and conjugate waves, P and C.

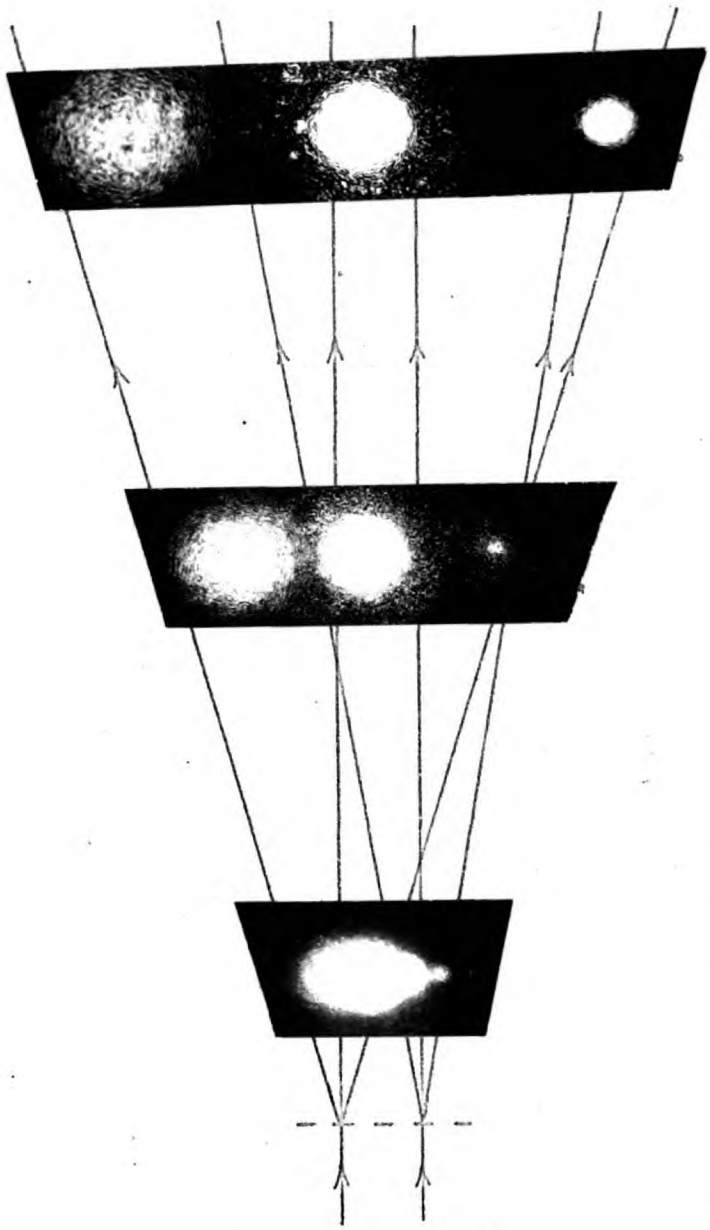

Separation of primary and conjugate waves by illuminating a lens hologram off-axis.

FIGURE 2.6

Converting the lens hologram into a phase lens hologram should theoretically increase its diffraction efficiency to approximately 2.5 times that of a Fresnel zone plate without this loss of image quality. [25-27]

2.5. USING LENS HOLOGRAMS.

2.5.1. Introduction.

To test the usefulness and quality of lens holograms as optical elements a number of simple optical systems were set up consisting solely of lens holograms recorded on Ilford R52 plates. Because it was impractical to make lens holograms with focal lengths smaller than $\pm$ 20cm using these plates it was not possible to transluminate objects much wider than a few centimeters.

2.5.2. Wavefront reconstruction.

Figure 2.5 illustrates what happens when an on axis lens hologram is illuminated by a planar wavefront. The interference pattern shown is the resultant intensity distribution brought about by the mutual interference between the two reconstructed waves and the illuminating wave. Figure 2.6 shows how these three waves can be separated by using an off axis lens hologram.

2.5.3. Use of lens holograms for visualization.

The simplest method for visualizing changes in refractive index is shadowgraphy. Figure 2.7a shows the optical system used to obtain the shadowgram illustrated in Figure 2.8a of a coal gas diffusion flame stabilized on a bat's wing burner. In this case an 8mW helium-neon laser was used to illuminate H_1 and the shadowgram was recorded

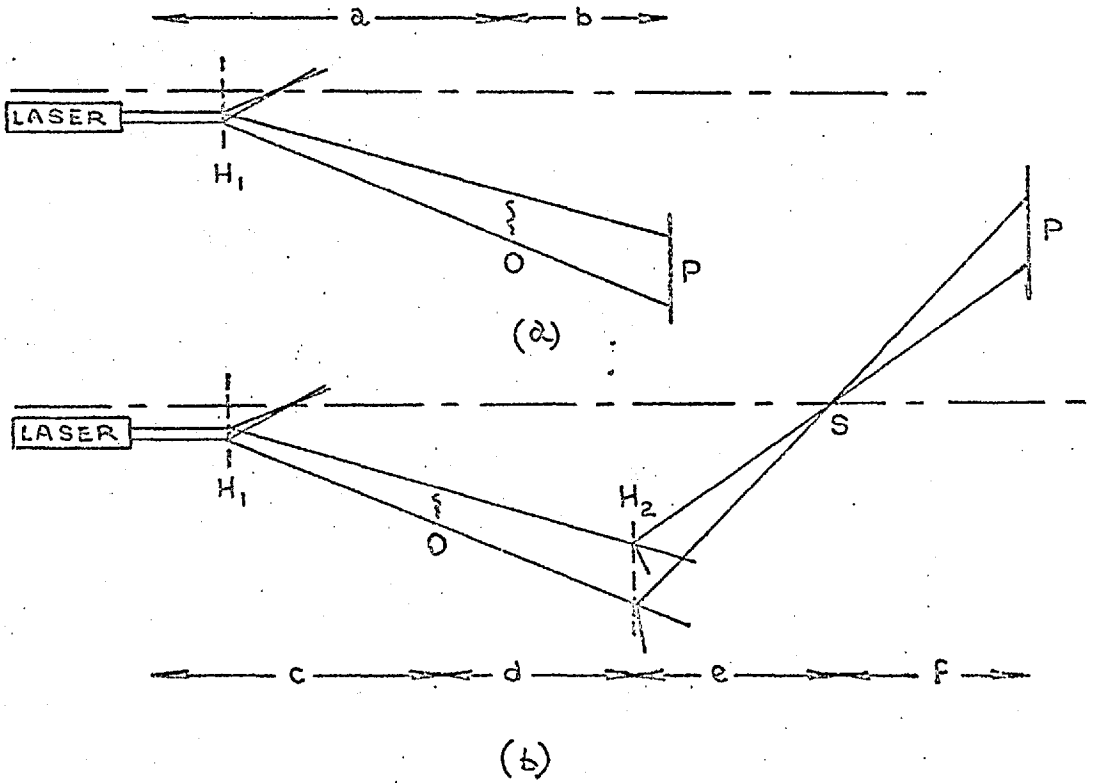

FIGURE 2-7

Optical systems used for the visualization of the phase and solid objects illustrated in Figure 2.8. (a) shadow system. (b) schlieren and ordinary imaging system. H_1, H_2, off-axis lens holograms; O, object; P, recording plane; S, position of schlieren stop. H_1, f.l. = ± 20cm. H_2, f.l. = ± 50cm. a = 475cm, b = 125cm, c = 350cm, d = 125cm, e = 70cm, f = 60cm.

on an R52 plate in approximately 1/5th second.

By placing a suitable schlieren stop at S in Figure 2.7b a premixed coal gas diffusion flame stabilized on a micro-burner and standing sound waves developed in air between a ½MHz transducer and a reflector plate were photographed. These are shown in Figures 2.8b and 2.8c. Figure 2.8d shows an image of an OBA nut and bolt photographed using the optical system in Figure 2.7b but without the schlieren stop. The flame and the bolt were recorded on R52 plates using an 8mW laser while the sound waves were recorded on an FP4 plate using a 2mW laser. The exposure time was the same in each case and equal to 10 minutes.

The comparatively good quality of the photographs in Figures 2.8c and 2.8d was because the objects were sufficiently small for it to be possible to select a reasonably uniform part of the transluminating beam. The speckle in Figures 2.8a and 2.8b arises from nonuniformities in the lens hologram's fringe pattern as well as from the finite grain structure of the fringes themselves.

2.6. CONCLUSIONS.

Under certain circumstanstances it has been shown that the aberrations of a lens hologram are for most practical purposes insignificant and it has been demonstrated experimentally that they can be used to replace conventional optical elements. One consequence of this is that one could arrange to have a pile of photographic copies of lens holograms for use under adverse conditions of, for example, extreme heat or in the event of explosion and simply replace them whenever they become too badly damaged. Also

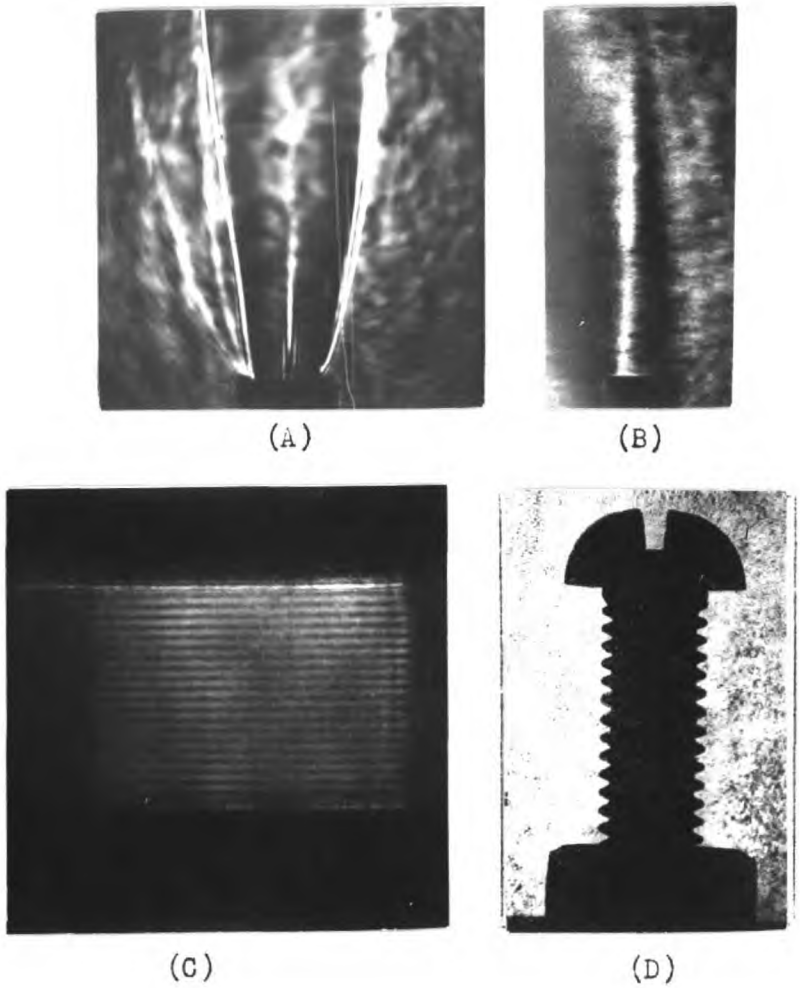

Photographs taken using lens holograms. (A) shadow of bat's wing diffusion flame. (B) schlieren of a premixed flame on a microburner. (C) schlieren of $\frac{1}{2}$MHz standing sound waves. (D) profile image of an OBA nut and bolt.

FIGURE 2.8

the theoretical possibility of making large diameter lens holograms suggests that it should be possible to make cheap substitutes for large schlieren lenses and mirrors. One application is to combustion rigs or wind tunnels of large working sections in which optically flat viewing windows could be made to incorporate the holographic elements. A suitable optical system is shown in Figure 2.9. Among other advantages of this scheme is that it avoids long path lengths of the parallel beam in the laboratory.

From the exposure times used in Figure 2.8 it was estimated that approximately 1.2joules are required for an exposure on FP4 plates for unit magnification. As this is quite readily available from a quite modest Q-switched ruby laser pulse lasting as little as a few tens of nanoseconds it implies that lens holograms can be used, in spite of their inefficiency, for studying extremely fast transient events such as for example travelling detonations.

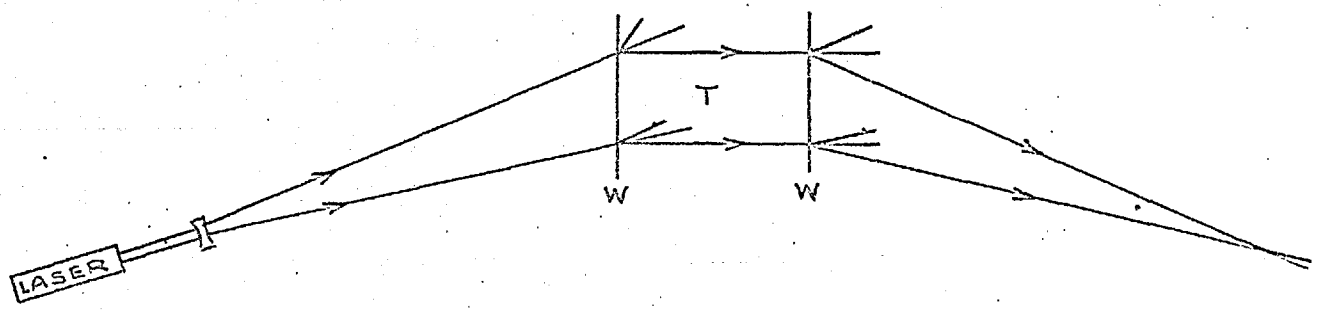

FIGURE 2-9

An example of an application of lens holograms for studying large cross sections such as in wind tunnels. W, window incorporating lens hologram; T, test section.

CHAPTER 3

THE 'DOPPLER' METHOD OF VELOCITY MEASUREMENT.

3.1. INTRODUCTION.

Velocity measurements are of vital importance in combustion research as they are essential for the understanding of moving phenomena such as lamina and turbulent gas flows, the flow of particulate fuels and aerosols, the propagation of flame fronts, detonation fronts, and shock ffonts. The various techniques that exist for making such measurements all require the simultaneous recording of both a distance and time interval. Until now the velocity of moving phenomena of interest in combustion has generally been deduced by measuring the time of traversal of a known distance, using methods such as ciné or streak schlieren photography, timing between ionization probes a known distance apart, or repetitive illumination of particles suspended in a gas. The new method proposed here can be thought of in terms of using interference fringes to mark a phase or solid object and then recording the fringe separation and the beat frequency as a measure of respective distance and time intervals. In these terms its merit lies in the non-interfering nature of the well articulated distance marker and the use of the beat wave as a convenient clock.

The theory of this method of measuring the velocity of any moving object by applying schlieren-interferometry to Doppler-shifted

laser light is given. It is shown how the microscopic shifts in frequency may most conveniently be measured by the method of beats and that the observed beat frequency may be interpreted as the motion of interference fringes across the front of a photodetector. Apart from the simplicity of the method it has the great advantage of not requiring any other optical components than are necessary in a conventional schlieren system.

The Doppler velocity method can be used for measuring the velocity of flows and propagating phenomena of interest in combustion. In the former case one is concerned with the physical motion of a medium (e.g. a cloud of fuel droplets) while in the latter in the motion of some phenomenon through a medium (e.g. a flame).

The Doppler principle has been applied to the study of moving objects since its formulation by C. J. Doppler[28] in 1842, who developed a theory to explain the colour of the light coming from moving stars. In the presentation of his theory he drew an analogy between light and sound waves and showed that if a source of radiation moves towards a stationary observer the observed frequency, ν_{ob}, is given by

$$\nu_{ob} = \nu_1 \left[\frac{c}{c - u}\right] \qquad \ldots 3.1$$

where u is the velocity of the source, c is the velocity of the radiation and ν_1 is the observed frequency when u = 0. On the other hand if the observer moves towards a stationary source the observed frequency is

$$\nu_{ob} = \nu_1 \left[\frac{c + u}{c}\right] \qquad \ldots 3.2$$

Although both these equations may be correctly applied to sound waves only the first may be applied to light waves since for light only relative velocities are meaningful, and in the case of a moving observer the source always appears to move relative to the observer. However, in practice this difference is of little consequence in practically all cases of interest in combustion as u/c is generally very much less than unity and equation 3.1 approximates to

$$\nu_{ob} = \nu_1\left[1 + \frac{u}{c}\right] \qquad \ldots 3.3$$

which is identical to equation 3.2.

A. H. L. Fizeau[29] in 1849 was the first to apply the Doppler principle for estimating the velocity of a moving star by measuring the shift in wavelength of the spectrum lines emitted by the star. Conventional spectroscopic techniques are probably capable of resolving[30] spectrum shifts in the visible of down to about 0.005Å and so the minimum velocity that can be measured this way is of the order of $30 m.s^{-1}$. In more recent years the velocity of rapidly expanding plasmas formed by the focusing of laser radiation into a gas has been determined (for example by Ramsden and Davies[31]) by direct spectroscopic measurement of the wavelength shift of light scattered off the plasma front. The 3Å wavelength shift, which was observed by Ramsden and Davies was well within the capabilities of standard spectroscopic methods and corresponded to a velocity of the order of $10^5 m.s^{-1}$. Their method differs fundamentally from Fizeau's because it makes use of an external light source and does not have to rely on any spectral emission from the moving body itself.

The microscopic wavelength shifts caused by slowly moving bodies cannot be measured directly. Instead, it is more convenient to use an interference method. Thus when two waves of different frequency are superimposed interference occurs and a beat frequency develops. The advent of lasers has made this method of measuring Doppler shifts particularly simple and the method to be described here may be applied to any moving body that either scatters, reflects or refracts light. This is in contrast to all previous beat frequency methods (for example refs 32 - 37) which have only been applied to moving scatterers.

Yeh and Cummins[32] were the first to used beats for measuring the change in frequency of light scattered off small moving particles suspended in water. Figure 3.1 shows that in this and subsequent[33-37] applications of the method the direction of the reference beam was always arranged to coincide at the photodetector with the direction of the scattered beam. Alignment difficulties exist in all those methods, except perhaps in the system used by Rudd[37]. Problems of alignment do not occur in the method proposed here as there is no necessity to ensure that the angle between the deflected and reference waves is zero at the photodetector. Whether the moving object is a scatterer, reflector or refractor the angle of deflection may be precisely defined using a parallel beam schlieren system in which the schlieren blind has a suitably positioned selective aperture - see Figure 3.1h. It is this utilization of the schlieren principle[38,39] that provides such great versatility to the proposed method and enables it to be applied to

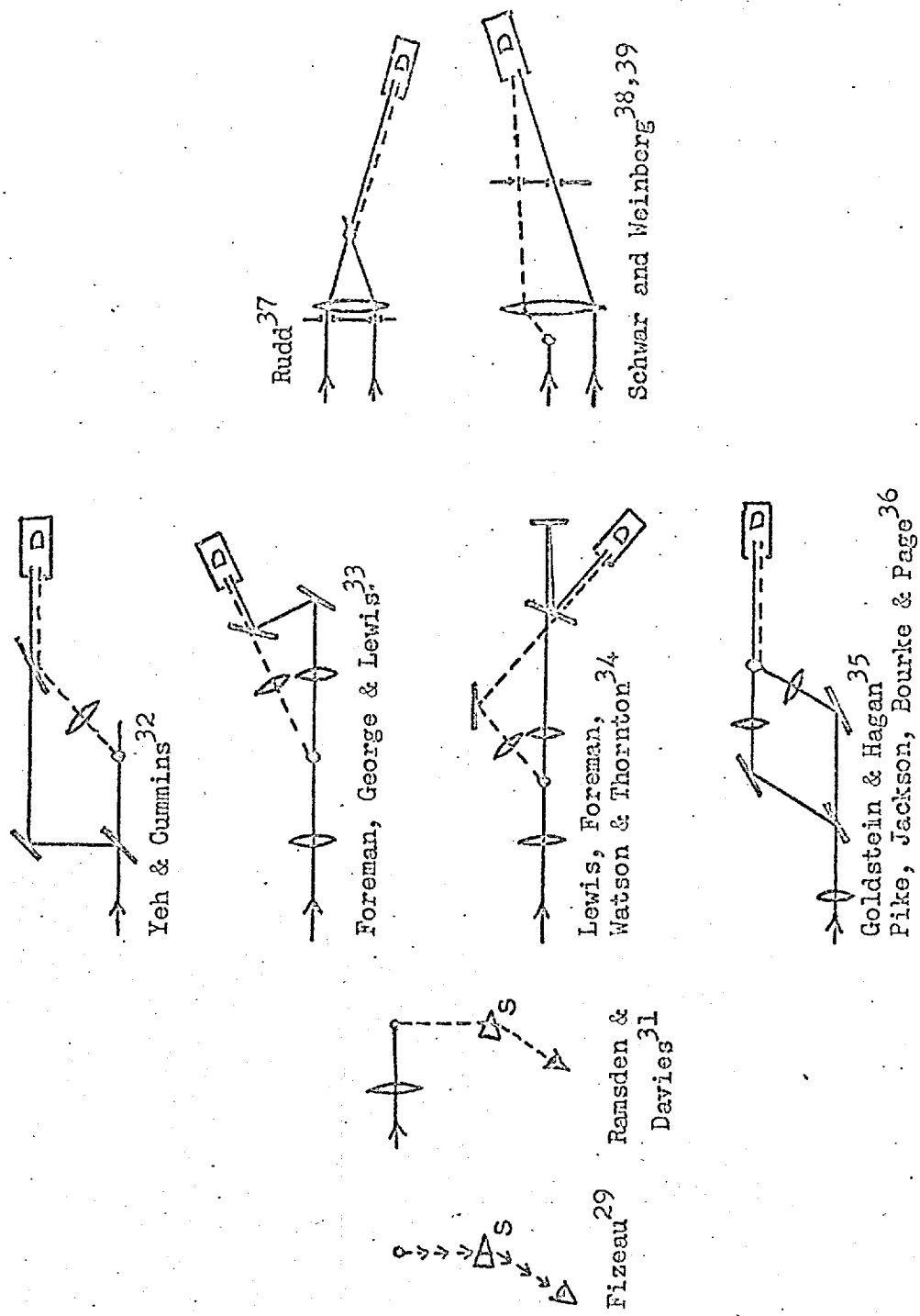

Evolution of Doppler velocity methods. →→→ emission from a luminous object; ▷S, spectroscope, ——— incident and reference light beam; ----- scattered Doppler shifted beam; [D], photo-detector; ∘ moving body.

FIGURE 3-1

both moving solid and phase objects.

3.2. DOPPLER SHIFT EQUATIONS.

3.2.1. Introduction.

In this section a general Doppler shift equation is first derived and then applied to a number of systems of interest in combustion. When a moving body is illuminated or transluminated by a stationary source equation 3.3 must be slightly modified as it is then necessary to take into account both the motion of the body relative to the source as well as its motion relative to the observer. Consider Figure 3.2 in which the source is situated in a medium of absolute refractive index $_{o}n_1$ and the observer is in a medium of absolute refractive index $_{o}n_2$. If the interface (which may be either discontinuous of diffuse) between the two media moves with a velocity u in a direction inclined at an angle γ to the interface's normal the source will appear to approach a point in the surface of the interface at a velocity $u \cos(\frac{1}{2}\pi - \phi + \gamma)$, where ϕ is the angle between the incident beam and the surface of the interface. The frequency of the radiation emitted by the source, providing $u/c \ll 1$, will therefore appear to the point in the surface to be given by

$$\nu_p = \nu_1 \left[1 + \frac{u}{c_1} \cos(\tfrac{1}{2}\pi - \phi + \gamma) \right] \quad \ldots 3.4$$

Similarly this point will appear to move away from the observer situated in medium 2 at a velocity $u \cos(\frac{1}{2}\pi - \phi + \gamma + \theta)$ and so the radiation coming from the point will have a frequency given by

$$\nu_2 = \nu_p \left[1 - \frac{u}{c_2} \cos(\tfrac{1}{2}\pi - \phi + \gamma + \theta) \right] \ldots 3.5$$

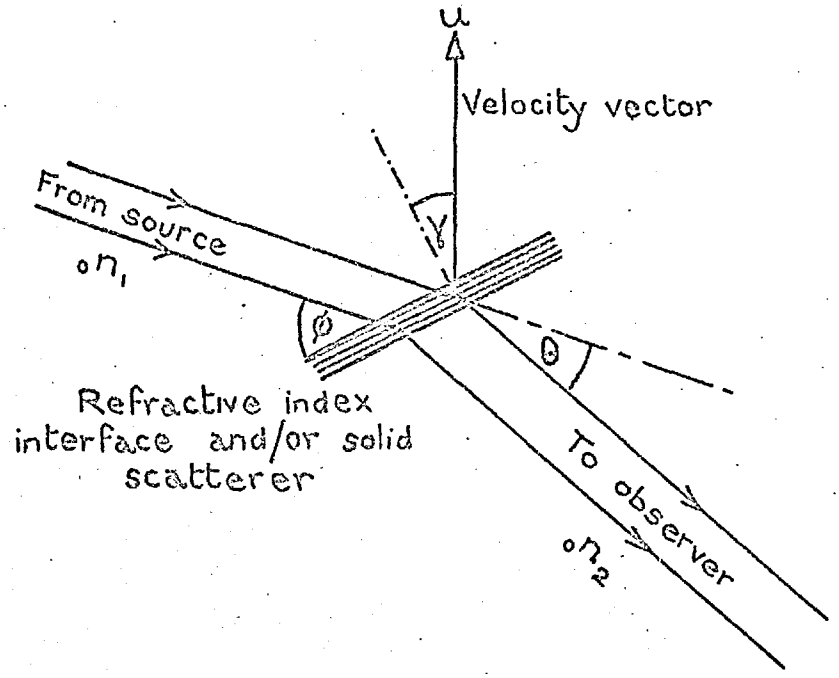

Diagram showing notation used to define the directions of the incident and deflected beams relative to the direction of a moving interface.

FIGURE 3-2

Substituting equation 4.4 into equation 4.5 and writing c_1/c_2 as $_1n_2$ therefcre gives

$$\nu_2 = \nu_1\left\{1 + \frac{u}{c_1}\left[\sin(\phi - \gamma) - {}_1n_2\sin(\phi + \theta - \gamma)\right]\right\} \quad \ldots 3.6$$

which is the general Doppler shift equation.

Frequently it is possible to greatly simplify this equation for in many practical cases of interest in combustion γ and ϕ may be made equal to zero. In the case of a solid object moving in the same medium as the source and observer a further simplification can be made as $_1n_2$ is equal to unity. Further simplification can be made in the case of gaseous phase objects by making use of the fact that for gases $(n - 1) \ll 1$ and hence the angle of deflection θ must always be small.

3.2.2. Doppler shift equations for a scatterer.

Equation 3.6 may be applied to a scatterer moving in the same medium as that containing the source and observer without any loss of generality by putting $\gamma = 0$ and $_1n_2 = 1$. A practical application is, for example, the motion of fuel droplets in air. The observed frequency is in this case

$$\nu_{ob} = \nu_1\left\{1 + \frac{u}{c_1}\left[\sin\phi - \sin(\phi + \theta)\right]\right\} \quad \ldots 3.7a$$

As it is proposed to select the light scattered through a particular angle using a selective aperture in a schlieren blind it is possible to define the angle of deflection very accurately even when θ is made very small. In this case

$$\nu_{ob} = \nu_1\left[1 - \frac{u}{c_1}\theta\cos\phi\right] \quad \ldots 3.7b$$

A further simplification can be made by arranging for the illuminating beam to be perpendicular to the direction of motion. When this is

done $\phi = 0$ and so

$$\nu_{ob} = \nu_1\left[1 - \frac{u}{c_1}\theta\right] \qquad \ldots 3.7c$$

It is a simple matter to extend the application of equation 3.7a to a scatterer moving in a medium of refractive index different to that containing the source and the observer. This would be of value when monitoring gas flows using tracer particles.

3.2.3. Doppler shift equations for phase objects.

Equation 3.6 is now applied to the three moving phase objects illustrated in Figure 3.3. In all cases the source and the observer are in a medium of refractive index ${}_on_1$.

Example 1:

An isolated phase object moving through its surroundings.

The analysis given here could, with slight modification, be applied to turbules or large transparent fuel droplets. In Figure 3.3a $\phi = 0$ and $\gamma = 0$ at the interface at A. Equation 3.6 therefore reduces to

$$\nu_2 = \nu_1\left[1 - \frac{u}{c_1}\,{}_1n_2\sin\theta_1\right] \qquad \ldots 3.8$$

At the second interface B $\phi_2 = \frac{1}{2}\pi + \theta_1$ and $\gamma_2 = \frac{1}{2}\pi$ and so the observed frequency is given by

$$\nu_{ob} = \nu_2\left\{1 + \frac{u}{c_2}\left[\sin\theta_1 - {}_2n_1\sin(\theta_1 + \theta_2)\right]\right\} \qquad \ldots 3.9$$

where ${}_2n_1 = c_2/c_1$. Combining these last two equations gives

$$\nu_{ob} = \nu_1\left[1 - \frac{u}{c_1}\sin\theta\right] \qquad \ldots 3.10a$$

where $\theta = \theta_1 + \theta_2$, the total angle of deflection. When θ is small this reduces to

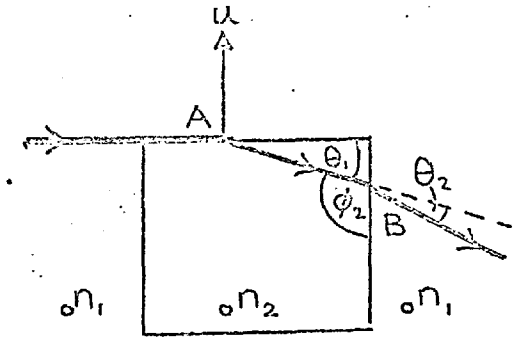

(A)

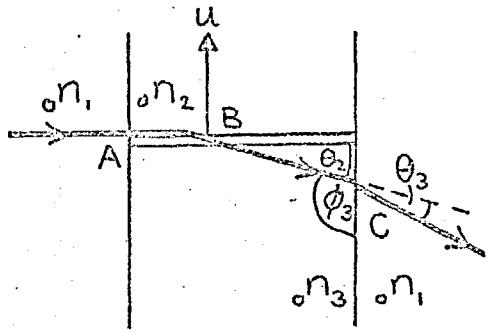

(B)

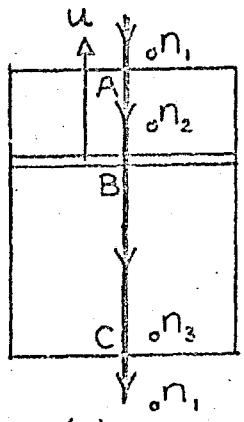

(C)

Examples of various moving phase objects

FIGURE 3-3

$$\nu_{ob} = \nu_1\left[1 - \frac{u}{c_1}\theta\right] \qquad \ldots 3.10b$$

Example 2:

Interface between medium 2 and medium 3 moving relative to medium 1. Grazing incidence.

This situation applies to propagating or moving flame, detonation and shock fronts with the transluminating beam incident tangentially. At the interface A in Figure 3.3b $\phi_1 = 0$ and $u_1 = 0$ and so there is no change in frequency on crossing the interface. At the next interface B $\phi_2 = 0$ and $\gamma_{\phi 2} = 0$ and so the frequency in medium 3 is given by

$$\nu_3 = \nu_1\left[1 - \frac{u}{c_2}\ {}_2n_3 \sin\theta_2\right] \qquad \ldots 3.11a$$

where ${}_2n_3 = c_2/c_3$. There can be no change in frequency on crossing the interface at C as $u_3 = 0$ and so equation 3.11a represents the frequency observed in medium 1. It may be put in a more convenient form by expressing θ_2 in terms of the total angle of deflection θ where $\theta = \theta_3 + \theta_2$. If Snell's law can be applied to the interface at C $\sin\theta_2 = {}_3n_1 \sin\theta$, where ${}_3n_1 = c_3/c_1$. The Doppler shift equation then becomes

$$\nu_{ob} = \nu_1\left[1 - \frac{u}{c_1}\sin\theta\right] \qquad \ldots 3.11b$$

If the total angle of deflection is small this reduces to

$$\nu_{ob} = \nu_1\left[1 - \frac{u}{c_1}\theta\right] \qquad \ldots 3.11c$$

Example 3:

Interface between medium 2 and medium 3 moving relative to medium 1. Normal incidence.

As $u_1 = 0$ there is no change in frequency on crossing the

interface at A in Figure 3.3c. The frequency in medium 3 after crossing the interface B where $\phi_2 = \frac{1}{2}\pi$ and $\gamma_2 = 0$ is given by

$$\nu_3 = \nu_1\left[1 + \frac{u}{c_2}\left(1 - {}_2n_3\right)\right] \qquad \ldots 3.12a$$

where ${}_2n_3 = c_2/c_3$. As $u_3 = 0$ there is no change in frequency on crossing the interface C and so this last equation also represents the observed frequency. Replacing c_2 by $c_1/{}_1n_2$ therefore gives

$$\nu_{ob} = \nu_1\left[1 - \frac{u}{c_1}\,{}_1n_2({}_2n_3 - 1)\right] \qquad \ldots 3.12b$$

In examples 1 and 2 it has been shown that the observed frequency is independent of the refractive index of the phase object except in so far as it determines the angle of deflection of the transluminating beam. Also for a given angle of deflection the expressions that have been derived are the same for both phase objects and solid scatterers. It is shown later in section 3.5 that the result in example 3 is consistent with conventional interferometry theory.

3.3. INTERFERENCE BETWEEN TWO WAVES OF DIFFERENT FREQUENCY.

3.3.1. Introduction.

Expressions have been derived in section 3.2 relating the observed Doppler shifted frequency to the original frequency of the incident beam. In all the cases of interest it has been shown that the observed frequency is given by

$$\nu_{ob} = \nu_1\left[1 - \frac{u}{c_1}\theta\right] \qquad \ldots 3.13a$$

(see equations 3.7c, 3.10b and 3.11c). Solving for u gives

$$u = -\frac{c_1}{\nu_1\theta}(\nu_{ob} - \nu_1) \qquad \ldots 3.13b$$

$(\nu_{ob} - \nu_1)$ is simply the beat frequency, ν_b, that arises when two waves of frequency ν_1 and ν_{ob} are interfered with one another. Equation 3.13b can therefore be put in the form

$$u = -\frac{\lambda_1}{\theta}\nu_b \qquad \ldots 3.13c$$

where $\lambda_1 = c_1/\nu_1$. Thus knowing λ_1, u can be determined by selecting θ and measuring ν_b.

3.3.2. Theory of interference.

In Figure 3.4 S represents a schlieren blind with a selective point aperture S_{ob} and a reference point source S_1. PP' represents a viewing screen and X is the distance along the optic axis between the screen and the schlieren blind. y is the distance of the point of observation P from the optic axis measured along the screen, and ξ is the angle the screen makes with the normal to the optic axis. m and l are the distances between P and S_{ob} and S_1 respectively. ϕ is the angle between the two interfering beams at the point P. The distance between S_{ob} and S_1 is d and between S_1 and the optic axis is a.

The resultant amplitude A at P is equal to the sum of the amplitudes originating from S_{ob} and S_1, i.e.

$$A = A_{ob}\cos 2\pi\left(\nu_{ob}t - \frac{m}{\lambda_{ob}} + \phi_{ob}\right) + A_1\cos 2\pi\left(\nu_1 t - \frac{l}{\lambda_1} + \phi_1\right) \qquad \ldots 3.14$$

The instantaneous illumination I at P is given by A^2 hence

$$\begin{aligned} I = {} & A_{ob}^2\cos^2 2\pi\left(\nu_{ob}t - \frac{m}{\lambda_{ob}} + \phi_{ob}\right) + A_1^2\cos^2 2\pi\left(\nu_1 t - \frac{l}{\lambda_1} + \phi_1\right) \\ & + A_{ob}A_1\cos 2\pi\left[(\nu_{ob}+\nu_1)t - \left(\frac{m}{\lambda_{ob}} + \frac{l}{\lambda_1}\right) + (\phi_{ob} + \phi_1)\right] \\ & + A_{ob}A_1\cos 2\pi\left[(\nu_{ob}-\nu_1)t - \left(\frac{m}{\lambda_{ob}} - \frac{l}{\lambda_1}\right) + (\phi_{ob} - \phi_1)\right] \end{aligned} \qquad \ldots 3.15$$

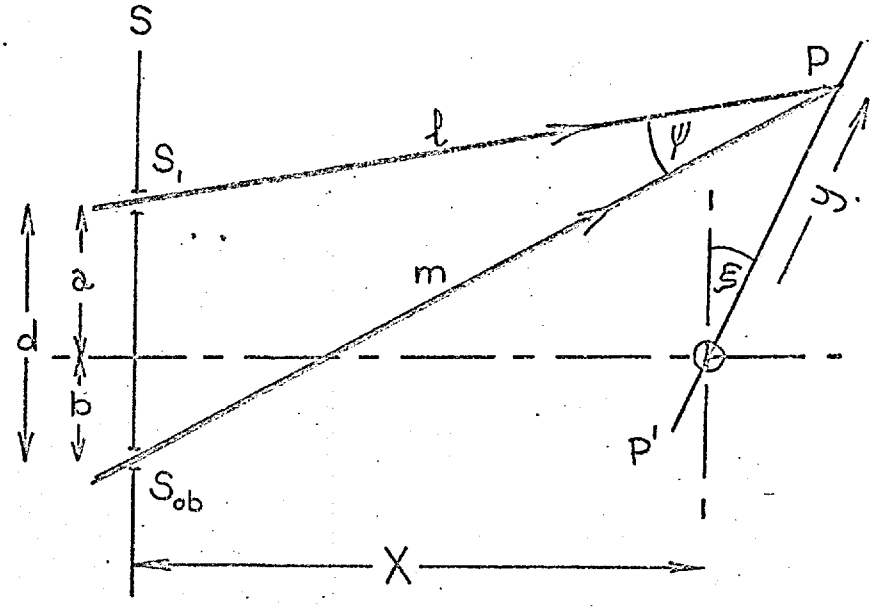

Co-ordinate system used in the theory of interference between two waves of different frequency. S_1, S_{ob}, point sources of light of frequency ν_1 and ν_{ob}; P, point of observation; P'P, viewing screen.

FIGURE 3-4

When the time constant of the photodetector is much larger than ν_{ob}^{-1} and ν_1^{-1} but smaller than $(\nu_{ob} - \nu_1)^{-1}$ the observed illumination at P becomes

$$I = I_{ob} + I_1 + 2(I_{ob}I_1)^{\frac{1}{2}}\cos 2\pi\left[(\nu_{ob} - \nu_1)t - \left(\frac{m}{\lambda_{ob}} - \frac{1}{\lambda_1}\right) + (\phi_{ob} - \phi_1)\right] \quad \ldots 3.16a$$

where $I_{ob} = A_{ob}^2/2$ and $I_1 = A_1^2/2$.

From Figure 4 and using equation 3.13a it can be shown that if $(y\cos\Sigma + (d-a))^2/(X + y\sin\Sigma)^2 \ll 1$ and $(y\cos\Sigma - a)^2/(X + y\sin\Sigma)^2 \ll 1$

$$I = I_{ob} + I_1 + 2(I_{ob}I_1)^{\frac{1}{2}}\cos 2\pi\left[\nu_b t - \frac{y}{\lambda^*} + \phi^*\right] \quad \ldots 3.16b$$

where

$$\nu_b = (\nu_{ob} - \nu_1) \quad \ldots 3.17a$$

$$\lambda^* = \frac{\lambda_1}{\beta}\left(\cos\Sigma - \frac{u}{c}\frac{\theta}{\beta}\sin\Sigma\right)^{-1} \quad \ldots 3.17b$$

$$\beta = \frac{d}{X} \quad \ldots 3.17c$$

$$\phi^* = \phi_{ob} - \phi_1 + \frac{d^2}{2X\lambda_1} - \frac{ad}{X\lambda_1} - \frac{Xu\theta}{\lambda_1 c_1} \quad \ldots 3.17d$$

3.3.3. Fringe velocity.

Equation 3.16b is a progressive wave and represents an interference fringe pattern travelling in the y-direction. λ^* represents the fringe spacing in the interference pattern. If the photodetector is to record the motion of the fringe pattern its entrance aperture should ideally be less than $\frac{1}{2}\lambda^*$. If ϕ^* is independent of time the fringe velocity v_f is given by

$$v_f = \nu_b\lambda^* \quad \ldots 3.18a$$

Substituting for ν_b from equation 3.13c and for λ^* from

equation 3.17b gives

$$v_f = - \frac{u\theta}{\emptyset\left(\cos\xi - \frac{u\theta}{c_1\emptyset}\sin\xi\right)} \qquad \ldots 3.18b$$

When $\xi = \frac{1}{2}\pi$ this reduces to

$$v_f = c_1 \qquad \ldots 3.18c$$

and represents the velocity of the interference pattern along the optic axis.

When $\xi = 0$, i.e. the viewing screen is perpendicular to the optic axis, the ffinge velocity becomes

$$v_f = - \frac{u\theta}{\emptyset} \qquad \ldots 3.18d$$

The ratio v_f/u represents a velocity magnification produced by the interference process. This is discussed further in section 3.4.

3.3.4. Moiré fringe analogy.

The physical sigrificance of the equations derived in this section can perhaps be better understood by considering the Moiré pattern produced by overlapping two gratings inclined at a small angle to each other. The angle of inclination is analogous to $\emptyset$, the line spacing is analogous to wavelength, and the Moiré fringes are analogous to the interference fringes.

Figure 3.5 illustrates the Moiré patterns produced when the two overlapping gratings differ in line spacing by 0, $\Delta\lambda$, and $2\Delta\lambda$ respectively. Whatever the difference in spacing of the two overlapping gratings is it is seen that the Moiré fringe spacing viewed on a screen perpendicular to the optic axis is always the same. This is in agreement with equations 3.17b and 3.13c. When the differencein line spacing is doubled it is seen from Figure 3.5

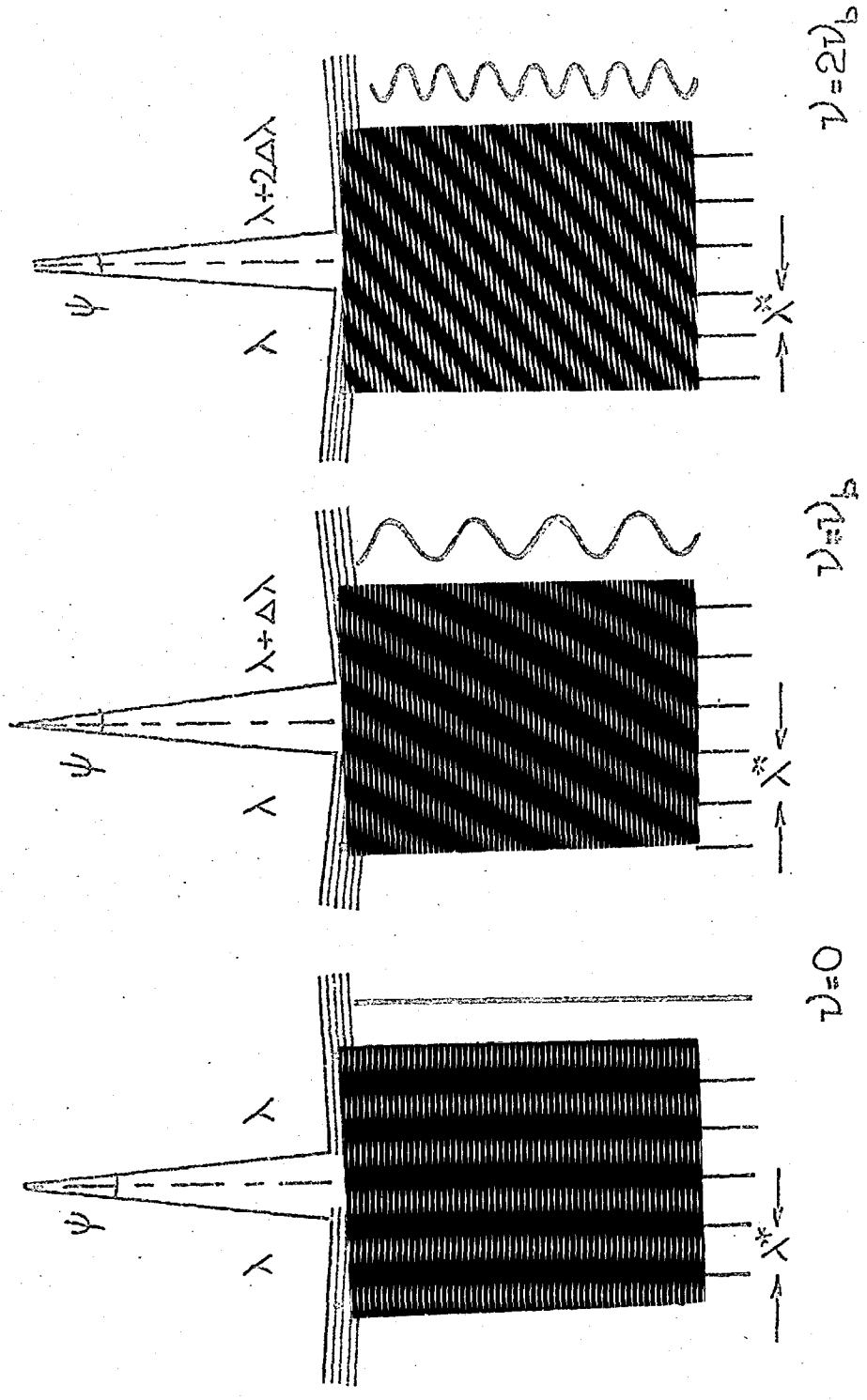

Moiré fringe analogy of the Doppler effect.

FIGURE 3-5

that the angle the Moiré fringes make with the viewing screen is also doubled. Therefore, as the fringe pattern propagates along the optic axis there must be a doubling in the observed beat frequency. As the Moiré pattern propagates along the optic axis it also appears to move across the viewing screen whenever there is a difference in line spacing of the two overlapping gratings. This is in agreement with equation 3.16b.

3.4. THEORY OF THE DOPPLER INTERFEROMETER.

3.4.1. Introduction.

Figure 3.6 represents the simplest form of Doppler interferometer. S_{ob} is an aperture in the schlieren blind S placed in the focal plane of the schlieren lens L in such a position that it selects light deflected through an angle Θ. S_1 represents a reference point light source which may be either independent of, an unperturbed part of, or a perturbed (i.e. deflected) part of the transluminating beam. The only requirement concerning its origin is that it and the Doppler shifted beam should contribute to ϕ^* in such a way as to make it independent of time.

In order that ϕ^* should be independent of time it is seen from equation 3.17d that restrictions must be placed on both $(\phi_{ob} - \phi_1)$ and $Xu\Theta/\lambda_1 c_1$. As u/c_1 and Θ are always very small the fifth term in the equation is negligible and so the effect of any time variation in u is generally insignificant. Therefore the problem becomes one of ensuring that $(\phi_{ob} - \phi_1)$ is independent of time. $(\phi_{ob} - \phi)$ represents the phase difference between the Doppler shifted beam and the reference beam at S_{ob} and S_1 and is

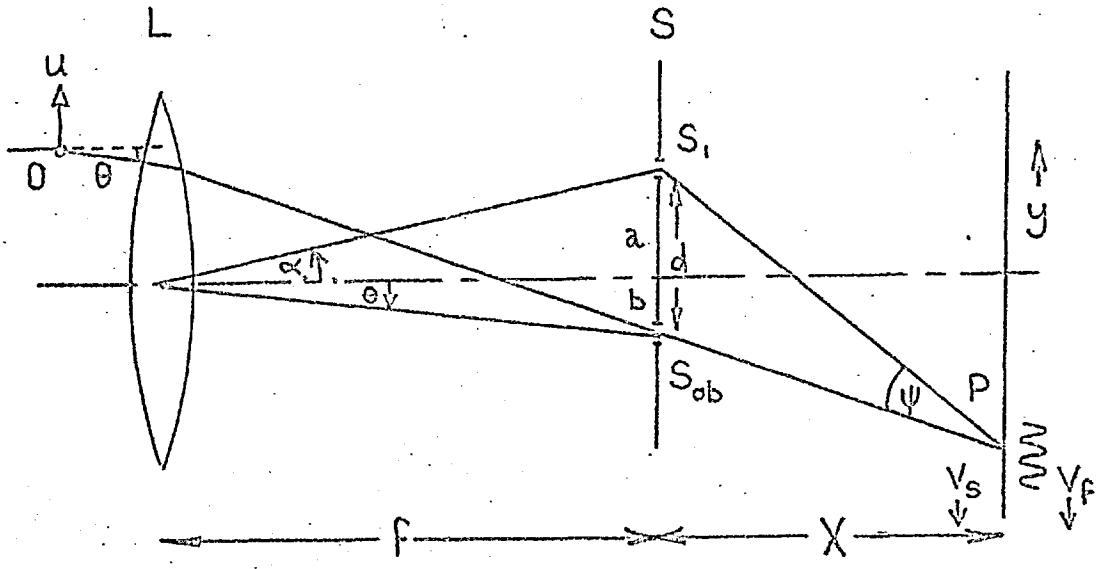

Essential elements of a Doppler interferometer. S_1, S_{ob}, selective apertures in a schlieren blind S; θ, angle light is deflected by a moving object; α, angle reference beam makes with the optic axis.

FIGURE 3-6

given by

$$\phi_{ob} - \phi_1 = \int_0^{S_{ob}} \frac{dx}{\lambda_{ob}(x)} - \int_0^{S_1} \frac{dx}{\lambda_1(x)} \quad \ldots 3.19$$

If $\lambda_{ob}(x)$ or $\lambda_1(x)$ varies with time so will the phase difference. For changes in this phase difference to be unimportant it is essential that the optical structure of the phase object, whose velocity is being measured, relative to the optical structure of the reference beam should change, if at all, only slowly in comparison with ν_b. I.e.

$$\frac{d}{dt}(\phi_{ob} - \phi_1) \ll \nu_b \quad \ldots 3.20$$

3.4.2. Shadow velocity.

In Figure 3.6 S_{ob} only transmits light that has been deflected through an angle θ by the test object O. The illumination on the screen may therefore be thought of as a selective shadow showing only the regions in the test object which are capable of producing deflections through an angle θ.

If u is the velocity of the object and M is the magnification of the system the velocity of the shadow v_s is given by

$$v_s = Mu \quad \ldots 3.21$$

When the shadow at P is conjugate with O the magnification of this optical system may be defined as the ratio of viewing distance to object distance (measured from the schlieren lens). By applying the lens equation ($M = 1 - v/f$) it immediately follows that

$$M = -X/f \quad \ldots 3.22$$

By similar triangles it can also be shown that when P is not conjugate with O the magrification is still given by this last expression. In this case M may be interpreted as being the ratio of distances between P and the optic axis and O and the optic axis.

The shadow velocity may be related to the fringe velocity by eliminating u between equations 3.18d and 3.21 to give

$$v_s = -\frac{M\,\phi'}{\theta} v_f \qquad \ldots 3.23$$

This can be put in a more convenient form by expressing ϕ' in terms of the angles θ and α used in Figure 3.6. For paraxial rays it is immediately obvious from Figure 3.6 that

$$\phi' = \frac{d}{X} \qquad \ldots 3.24a$$

$$\theta = \frac{b}{f} \qquad \ldots 3.24b$$

$$b = d - a \qquad \ldots 3.24c$$

$$\alpha = \frac{a}{f} \qquad \ldots 3.24d$$

Eliminating a, b and d from these four equations, making use of equation 3.22, and solving for ϕ' then gives

$$\phi' = -\frac{(\theta + \alpha)}{M} \qquad \ldots 3.25$$

When this is substituted into equation 3.23 one finally obtains

$$v_s = v_f\left[1 + \frac{\alpha}{\theta}\right] \qquad \ldots 3.26$$

It follows that when the reference source S_1 falls on the optic axis (i.e. $\alpha = 0$) the interference fringes travel in the same direction and with the same velocity as the shadow. When α is finite and positive the fringes become narrower and the fringes move slower than the shadow. As S_1 moves closer to S_{ob} the

interference fringes become wider and the fringe velocity is greater than the shadow velocity. Thus, whatever the fringe width one can see qualitatively that the rate of passage of fringes past any fixed point always tends to remain constant.

3.4.3. Minimum beam width.

Clearly beats can be observed only while the object is still within the transluminating beam. The number of beats, and hence the accuracy of the beat frequency measurement, will therefore depend on the width of the beam. As the time required to observe N beats is $N\nu_b^{-1}$ an object having a velocity u will move a distance w_o given by

$$w_o = \frac{u N}{\nu_b} \qquad \ldots 3.27a$$

during the period of observation. Thus for N beats to be observed the transluminating beam must have a width at least equal to w_o. w_o may be interpreted as representing the minimum beam width necessary to obtain a beat frequency measurment to a given accuracy. By making use of equation 3.13c it may be expressed in a more convenient form. i.e.

$$w_o = \frac{\lambda_1}{\theta} N \qquad \ldots 3.27b$$

The application of equation 3.27 implicitly assumes that the shadow is capable of forming N fringes if allowed to interfere with a reference beam originating from a point source on the optic axis in the schlieren blind. To calculate the number of fringes so formed it is necessary to consider the diffraction effects produced by the selective aperture S_{ob}. Diffraction is important because S_{ob} has to

be made very small so that the angle of deflection Θ is defined as accurately as possible. The width of a selective shadow of a phase object having a continuously changing refractive index gradient formed using an infinitesimally small selective aperture would be zero using a geometric theory but infinity wide using a wave theory. The angular width Ω of a selective shadow broadened by diffraction - see Figure 3.7 - as a result of using a selective aperture having a finite diameter s_{ob} is approximately given by

$$\Omega = \frac{2\lambda_1 n}{s_{ob}} \qquad \ldots 3.28$$

where n is the number of diffraction orders (including the central maximum) that the detector can see. The width of the shadow w_s is given by

$$w_s = \Omega X \qquad \ldots 3.29$$

and the time T it takes to pass a small photodetector is

$$T = \frac{w_s}{v_s} \qquad \ldots 3.30$$

In general v_f is not equal to v_s and so the distance w_f the fringe pattern moves during this time is

$$w_f = v_f T \qquad \ldots 3.31$$

The number of fringes seen by the photodetector in this time interval is

$$N = \frac{w_f}{\lambda^*} \qquad \ldots 3.32$$

where λ^* is given by equation 3.17b. When the viewing plane is perpendicular to the optic axis

$$\lambda^* = \frac{\lambda_1}{\emptyset} \qquad \ldots 3.33$$

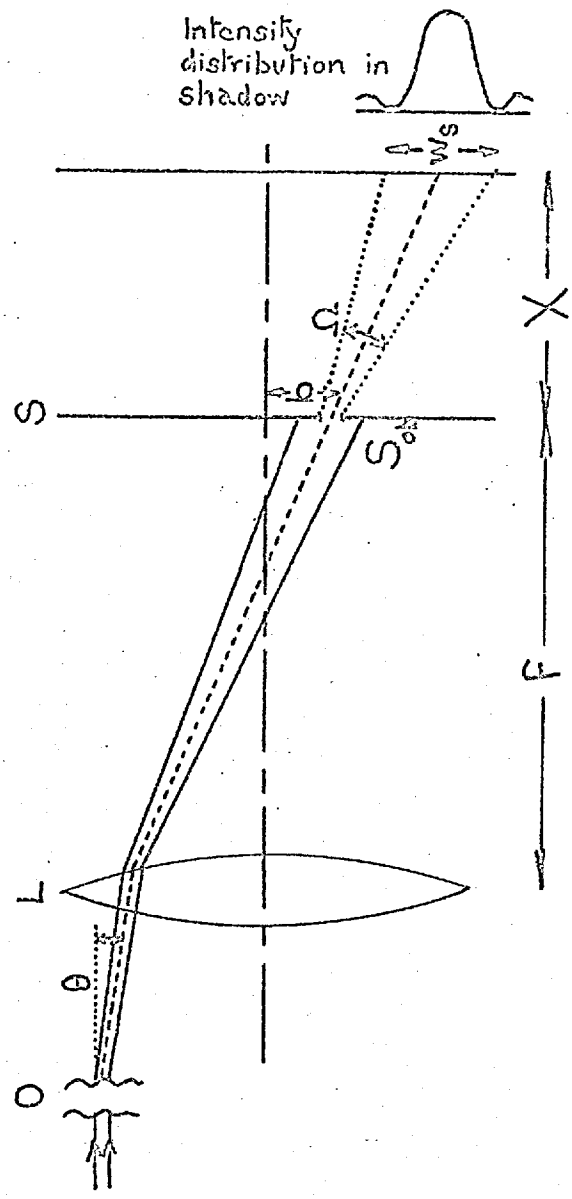

Increase in the width of a geometric shadow as a result of diffraction by the selective aperture, S_{ob}.

FIGURE 3-7

Combining equations 29 to 32 one obtains

$$N = \frac{v_f X\Omega}{v_s \lambda^*} \qquad \ldots 3.34$$

Substituting equations 3.26, 3.28 and 3.33 into equation 3.34 and then making use of equations 3.25, 3.24b and 3.22 one finally obtains

$$N = \frac{2nb}{s_{ob}} \qquad \ldots 3.35$$

which is independent of both θ and α. Thus, by making s_{ob} very much smaller than b, N can be made large; it also minimizes the error in θ.

There is no point, however, in making N greater than $w_o\theta/\lambda_1$ (see equation 3.27b) as beats cannot be detected once the object has moved out of the transluminating beam. If N, given by equation 3.35, is less than $w_o\theta/\lambda_1$ the number of beats recorded is 'diffraction' limited while if it is greater than $w_o\theta/\lambda_1$ it is beam width limited.

About 84% of the light in the selective shadow falls in the central maximum and unless the sensitivity range of the photo-detector is very large n appearing in equations 3.28 and 3.35 may be taken to be slightly less than unity

The fractional error in the beat frequency measurement is of the order of $1/N$. If the accuracy is to be increase for example by a factor of two in a diffraction limited system by doubling the number of beats equation 3.35 indicates that it would be necessary to halve the diameter s_{ob}. However, the lower limit of s_{ob} is set by the sensitivity of the photodetector. Halving s_{ob} will reduce

the flux passing through the aperture by a factor of 4 and (according to equation 3.28) increase the angular divergence by a factor of 2. If the incident beam completely fills the selective aperture there will consequently be a total reduction in fringe intensity by a factor of 16. This may be below the threshold of the photodetector's response and so simply reducing the diameter of S_{ob} may not in practice correspondingly increase the accuracy of the frequency measurement indefinitely.

Figure 3.8 illustrates how the accuracy of a diffraction limited system can be increased even when there is a loss in fringe intensity. G is a ruled grating or instantaneous photograph of the moving fringe pattern itself. The lens L projects all the light transmitted by the grating onto the photodetector P which records a signal each time the fringe system moves a distance equal to one grating spacing. The size of the signal is the same as that produced by a single fringe multiplied by the number of fringes covering the grating at any particular time. If there are N fringes in the interference pattern and M clear rulings in the grating the number of beats seen by the detector is increased from N to (N + M - 1).

If s_{Lt} represents the smallest selective aperture that can be used with a particular detector the accuracy of the beat frequency measurement can be increased as follows. In a diffraction limited system the number of beats may be doubled by halving the selective aperture diameter. From what has been said before this will immediately result in a fall in intensity of each fringe by a factor of 16. If the photodetector can just detect a single fringe when

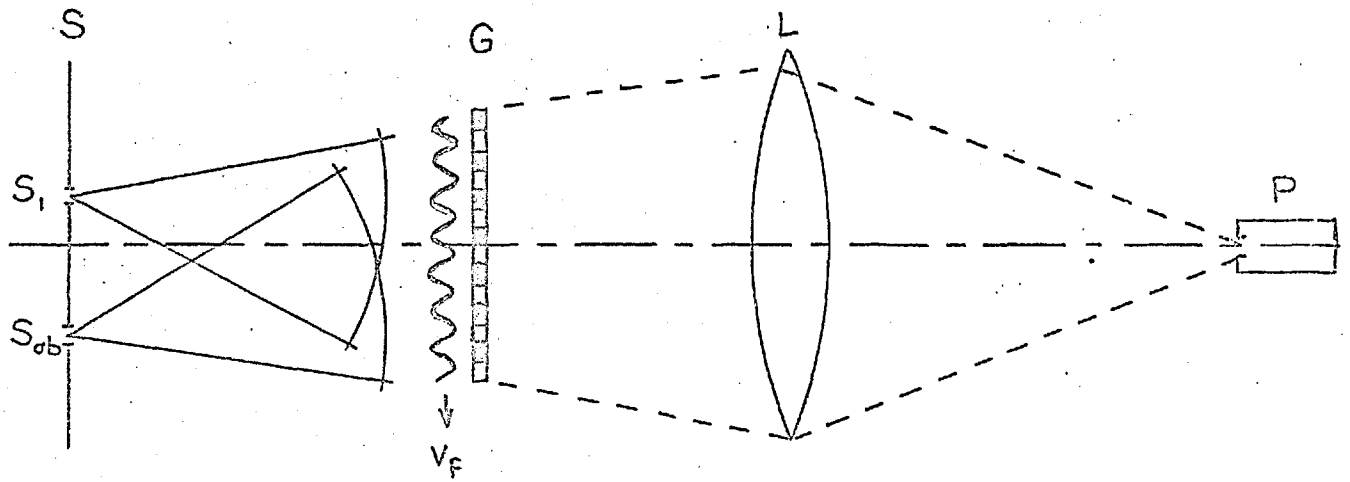

FIGURE 3-8

Use of grid, G, to increase the flux of light falling on the photodetector, P.

the selective aperture has a diameter s_{Lt} it requires at least 16 fringes in front of G before it can respond when the aperture is reduced to $\frac{1}{2}s_{Lt}$. In other words the first and last 15 fringes passing the grid do not contribute to the recorded beat frequency signal. Therefore, the effective number of beats is in this case given by (N + M - 1 - 30) and for N fringes to contribute to the beat frequency signal M must be chosen such that

$$N = N + M - 1 - 30,$$

i.e. M must be made equal to 31.

Whenever a grating is used to increase the accuracy of a frequency measurement in a diffraction limited system N appearing in equations 3.27, 3.34 and 3.35 should be replaced by (N + M - 1 -K) where K is a factor that depends on the diameter s_{ob} and the sensitivity of the photodetector and may be calculated as indicated in the above example.

3.5. PRACTICAL DOPPLER INTERFEROMETERS.

3.5.1. Introduction.

Doppler interferometers may be classified according to how the reference beam is introduced into the system. Figure 3.9 illustrates the three basic types of interferometer in which the reference beam is (a) independent of, (b) an unperturbed part of and (c) a perturbed part of the transluminating beam.

3.5.2. Independent reference beam.

By using the system in Figure 3.9a the width of the reference beam can be adjusted independently of the test beam and it is possible to obtain a region of overlap almost anywhere. The

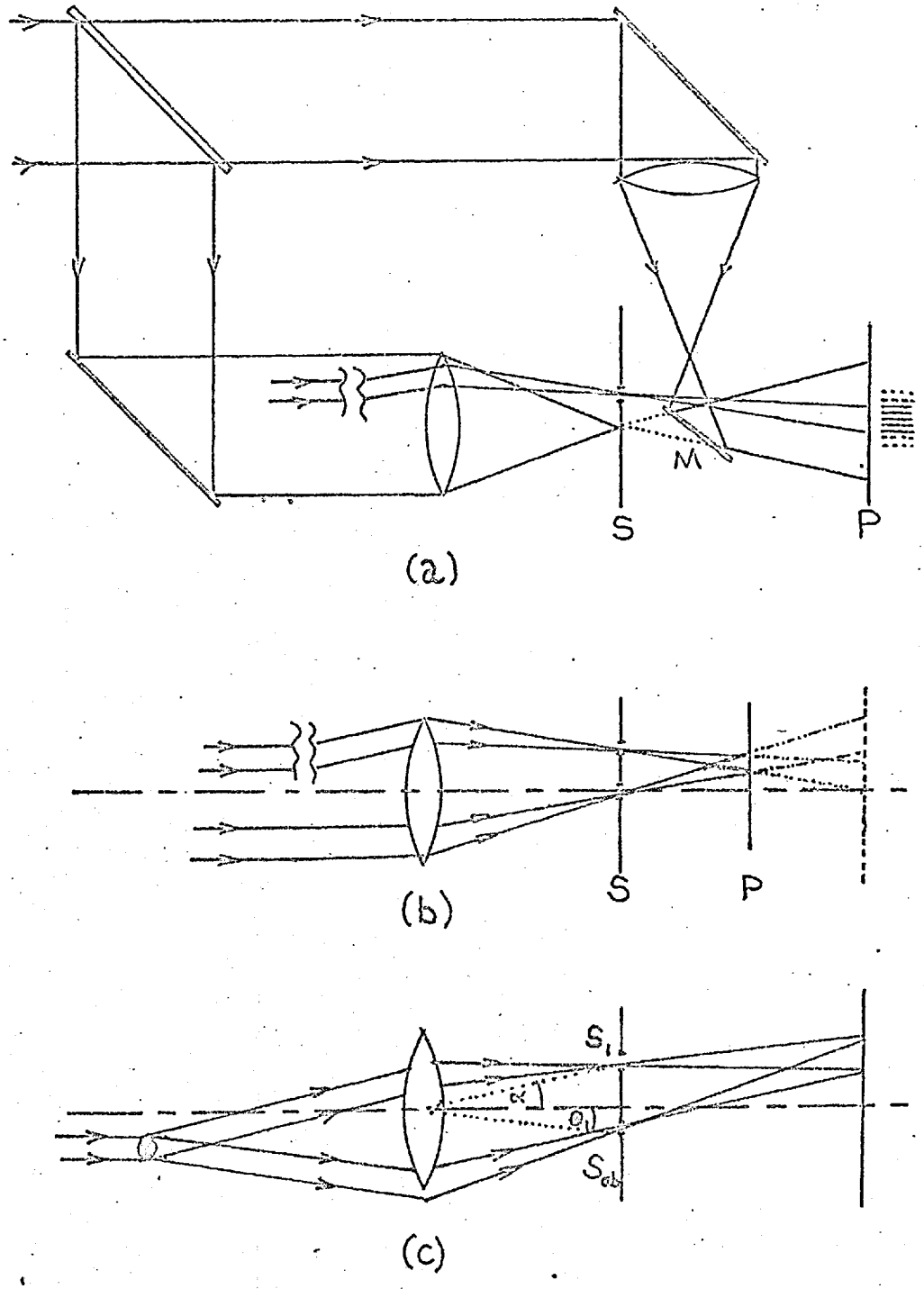

Three basic types of Doppler interferometers. (a) independent reference beam. (b) unperturbed reference beam. (c) perturbed reference beam.

FIGURE 3-9

alignment of the mirror M is not at all critical as the foregoing analysis has shown the method to be independent of the orientation of the axis of the reference beam. The longitudinal position of the detector will depend on the width of the entrance aperture and on the fringe spacing of the interference pattern. By adjusting the effective distance between P and S, possibly using an auxiliary lens or lenses, a position can always be found where the fringe spacing is at least equal to twice the width of the photodetector's entrance aperture.

3.5.3. Unperturbed reference beam.

Many of the mounting and alignment problems of the previous system are absent in the unperturbed reference beam arrangement illustrated in Figure 3.9b. In this case the reference beam is of limited width and so the region of overlap in which interference can be observed is more restricted. When auxiliary lenses are used to achieve the desired overlap the fringe spacing is still given by $\lambda_1 X/d$ but the actual distance X of the schlieren blind from the viewing plane must be replaced by its image distance.

3.5.4. Perturbed reference beam.

In the previous two systems it may be necessary to attenuate the reference beam somewhat in order to match its intensity with the deflected beam. Figure 3.9c illustrates a particularly simple system for measuring the velocity of solid particles in which the intensities of the deflected beam and the so called perturbed reference beam can easily be made equal. This is achieved by arranging for the apertures S_{ob} and S_1 to select light symmetrically scattered in the forward and backward directions. With this arrangement the best position for the photodetector is in the conjugate plane of the object for it is here that the two scattered beams exactly overlap.

In the equations derived earlier it was always assumed that the reference beam was unperturbed and of exactly the same frequency of the transluminating beam. However, in this case both beams are Doppler shifted. The frequency of the deflected beam and the reference beam are given by

$$\nu_{ob} = \nu_1\left[1 - \frac{u}{c_1}\theta_1\right] \qquad \ldots 3.36$$

$$\nu_r = \nu_1\left[1 + \frac{u}{c_1}\alpha\right] \qquad \ldots 3.37$$

and so the observed beat frequency $(\nu_{ob} - \nu_1)$ is given by

$$\nu_b = -\frac{u\theta}{\lambda_1} \qquad \ldots 3.38$$

where $(\theta_1 + \alpha)$ has been replaced by θ, the total angle between the reference and deflected beams.

3.5.5. Consistency between interferometry and the Doppler effect.

In section 3.2.3 an expression was derived for the Doppler shift in frequency produced when a light beam passes both normal to its direction of motion and its refractive index interface. When this Doppler shifted wave is combined with an unperturbed reference wave a beat frequency $\nu_b = (\nu_{ob} - \nu_1)$ develops. Rearranging equation 3.12b, which was derived by applying the Doppler principle, one obtains

$$\nu_b = -\frac{u}{\lambda_1}\,{}_1n_2({}_2n_3 - 1) \qquad \ldots 3.39a$$

On expressing all quantities in terms of free space values this reduces to

$$\nu_b = -\frac{u}{\lambda_o}\,({}_on_3 - {}_on_2) \qquad \ldots 3.39b$$

It is easily shown that the same result can be arrived at

by applying conventional interferometry theory to the system illustrated in Figure 3.10. Under static conditions the optical path difference between the reference beam and the test beam is given by

$$ {}_{o}n_1 L - {}_{o}n_2(L - x) - {}_{o}n_3 x = p\lambda_o \qquad \ldots 3.40 $$

Clearly as x increases so p will change and for every integral change in p there will be a corresponding cyclic change in intensity which passes through a maximum and minimum. The rate of change of p with time that occurs when x changes with time may be considered analogous to ν_b. Solving equation 3.40 for p and then differentiating both sides with respect to time one obtains

$$ \frac{dp}{dt} = - \frac{1}{\lambda_o} ({}_{o}n_3 - {}_{o}n_2) \frac{dx}{dt} \qquad \ldots 3.41 $$

On replacing dp/dt and dx/dt by ν_b and u respectively equation 3.41 then becomes identical to equation 3.39b.

3.6. CONCLUSIONS.

A self consistent theory has been given describing in detail the nature and limitations of a new method for measuring the velocity of moving objects by applying schlieren-interferometry to Doppler-shifted laser light. This is particularly useful in combustion research because it now provides a very simple means of measuring the velocity of phase objects such as propagating flames and detonations. The fact that it is also capable of measuring local velocities has the added advantage of being able to detect local fluctuations in velocity that may be associated with various instabilities in flame and detonation propagation.

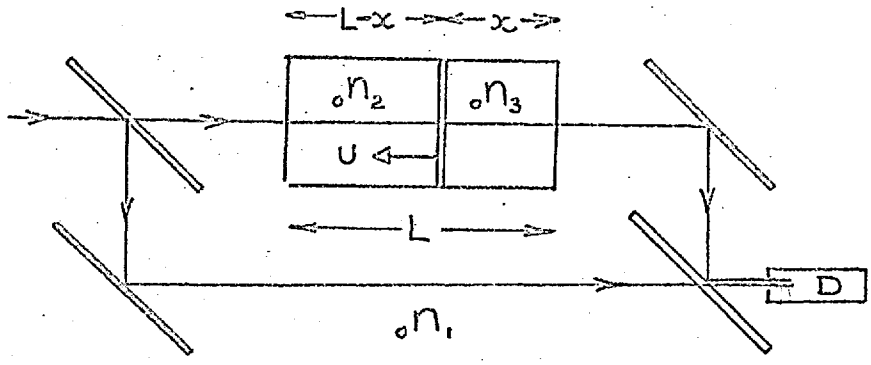

Interferometer for observing the beat frequency signal produced by an interface moving parallel to the trans-luminating beam.

FIGURE 3-10

It has been shown that the limitations of the method depend on the accuracy of the angle of deflection and of the beat frequency measurements as well as on the threshold sensitivity of the photodetector. For the most accurate velocity measurements it is necessary to use a diffraction limited rather than a beam width limited system. However, this will give a velocity value averaged over a comparatively large distance. In a diffraction limited system this limitation may be conveniently summarized by the expression

$$w_o \frac{\Delta u}{u} = \frac{\lambda_1}{\theta}(1 + 2n) \qquad \ldots 3.42a$$

where w_o is the distance over which the velocity measurement is made and $\Delta u/u$ represents the fractional uncertainty of the velocity measurement. Spatial and velocity uncertainties can be kept to a minimum by making the right hand side of equation 3.42a as small as possible. In the first place this may be done by making n small. In practice this this means that s_{ob} must be made very small so as to diffract the light over a large area. However, there is no point in making n much smaller than 1/2 as its effect then will not appreciably contribute to reducing the uncertainty. Under the most favourable conditions (i.e. s_{ob} very small and hence n small) the uncertainty equation becomes

$$w_o \frac{\Delta u}{u} = \frac{\lambda_1}{\theta} \qquad \ldots 3.42b$$

In the case of gaseous phase objects usually encountered in combustion research θ does not generally exceed 1/50 radians and so for such objects this uncertainty becomes, at best

$$w_o \frac{\Delta u}{u} = 50\lambda_1 \qquad \ldots 3.42c$$

Thus a measurement in u correct to 1% cannot be made unless the transluminating beam width is at least of the order of $5\times10^3\lambda_1$. When the wavelength of the beam is 6×10^{-5}cm w_o must be at least 3mm. These expressions do seem to indicate that previous Doppler velocity measurements using focused laser beams cannot possibly give very accurate results. Thus if the beam is focused down to a beam width of the order of $10\lambda_1$ and the angle of deflection is $\pm\gamma$ the velocity error must be at least 10%.

Apart from describing the behaviour of the Doppler interferometer the theory presented here can be used to explain the motion of interferogram fringes of a moving phase object in which the reference beam is inclined to the test beam.

CHAPTER 4

'DOPPLER' VELOCITY MEASUREMENTS

4.1. INTRODUCTION.

The combination of high brightness and good spatial coherency of a gas laser makes it an ideal light source for Doppler shift measurements and permits the Doppler method of measuring velocities proposed in Chapter 3 to be tested. A number of practical systems relevant to combustion are described and it is demonstrated that the method may be successfully applied both to moving solid objects, in the form of a rotating grating, wires and discs simulating clouds of particles, and to moving phase objects in the form of progressive sound waves and moving flame fronts.

4.2. APPARATUS.

4.2.1. Introduction.

One great advantage of the Doppler velocity method is that no more optical components are needed than are already used in a conventional parallel beam schlieren system. The only other accessaries required are a photodetector of suitable sensitivity and frequency response, and some form of frequency meter.

4.2.2. Light source.

The coherency requirements of the light source can be estimated by considering the interference process which results

in the formation of fringes in the Doppler interferometers illustrated in Figure 3.9. Fringes can only be formed in the region of overlap of the two interfering beams when they are coherent both spatially and temporally[40a].

A helium-neon gas laser, giving a uniphase output, may be used in all three of the interferometers illustrated as they have effectively perfect spatial coherence and even under the worst possible conditions have a temporal coherence distance longer than 30cm[41]. However, such good coherency is not absolutely essential for the Doppler velocity method.

Spatial and temporal coherence requirements are a minimum in the Doppler interferometer illustrated in Figure 3.9a because of the point to point correspondence between the test and reference beams and because of the facility of being able to arrange for zero optical path difference between the two beams. The perturbed reference beam interferometer in Figure 3.9c requires the transluminating beam to be spatially coherent over the cross section of the object producing the selected deflections. In the case of a solid object this distance is zero. The essentials of this interferometer are very similar to Young's two aperture interference experiment in which it is well known that some interference fringes can be formed using even white light[40b]. Ideally to obtain a large number of sharp fringes the beam must be highly spatially coherent over the cross section producing the deflection; this requires the source to have a very small effective size[40a]. Temporal coherence of the source is important only in so far as it must be capable of

forming a finite number of fringes. Even a 50Å wide line source can form over 100 fringes. The temporal coherence length of such a source is less than 0.1mm and so the optical path difference between the test and reference beams must always be kept less than this. In principle, therefore, it would appear that thermal sources could be used for the Doppler velocity method but because of alignment problems and their low power outputs (because of their small effective size) the availability of gas lasers with vastly superior properties makes them redundant. However, if a gas laser is unavailable it is possible in certain circumstances to make a useful velocity measurement using a tungsten filament lamp as a light source.

Apart from the preliminary work a Scientifica and Cook Electronics B18/3 8mW d.c. uniphase helium-neon gas laser was used for all the velocity measurements described here. The laser cavity supports about five axial modes separated in frequency by approximately 3×10^{8}Hz and each having a line width less than 10^{6}Hz. The exact line width of each mode depends on the power output, the cavity length and stability, and the reflectivity of the cavity mirrors. The output from the laser is, therefore, modulated at a number of beat frequencies as a result of mutual interference between the various axial modes[41]. In this case the lowest beat frequency would be of the oder of 3×10^{8}Hz.

4.2.3. Detector.

The two requirements governing the choice of detector are sufficiently high sensitivity and high frequency response. An

An upper limit for the Doppler beat frequencies likely to be encountered in combustion studies may be estimated by considering a discontinuous refractive index interface travelling at sonic velocity perpendicular to the diagnostic beam. The beat frequency in this case is given by

$$\nu_b = \frac{u(2\delta)^{\frac{1}{2}}}{\lambda_1} \qquad \ldots 4.1$$

If $u = 3.4\times10^{4}\,cm.s^{-1}$, $\delta = 2.9\times10^{-4}$, and $\lambda_1 = 6.3\times10^{-5}cm$ the upper limit of ν_b is of the order of $1.3\times10^{7}Hz$. This is twenty times smaller than the minimum beat frequency of the laser output and so the presence of axial modes should cause no difficulty in measuring frequency shifts by the method of beats. If it is intended to work at beat frequencies as high as $10^{7}Hz$ the response time of the detector must be at least 100ns. A detector that satisfies this response time requirement and which is also extremely sensitive to very low levels of illumination is a photomultiplier. The detector used in all the measurements described here was an EMI 9529B photomultiplier with an S10 cathode having a spectral response up to 7500Å.

4.2.4. Frequency metering.

The most convenient method of measuring the frequency of a limited train of beats is to display and photograph the beat signal using a cathode ray oscilloscope. Alternatively an electronic timer can be used. Such an instrument counts the number of beats seen by the detector in a preset time interval. This method is particularly suitable for examining a continuous train of beats. Another method would be to measure the time interval for a preset number of beats

to pass in front of the photodetector. Both these methods of frequency measurement may be performed using an Advance TC3 Timer Counter.

4.2.5. Optical apparatus.

Figure 4.1 illustrates the essential features of the optical apparatus used in all the Doppler velocity measurements described here.

The beam emerging from the laser was focused onto a small pinhole P of the order of 50μm diameter. This had the effect of eliminating[7b] any diffraction rings caused by dust on the cavity mirrors and on the short focal length lens L_1. After collimation the beam was passed through the test object and brought to a focus on the optic axis using a schlieren lens of focal length between 50cm and 200cm (depending on the sensitivity required). Deflections produced in the test space could be selected by making two pin holes in the schlieren blind S as shown. These were usually about 0.1mm in diameter and 1cm separation. It was found convenient to first form a fringe pattern close to the schlieren blind using a short focal length lens L_4 ($\sim$10cm focal length) and then to enlarge this using another short focal length lens L_5 ($\sim$1cm focal length) to any desired size suitable for the detector. If necessary the position of the fringes could be calculated from the lens equation by considering the object to be located at the point of intersection O of the back projection of the test and reference rays. However, in practice this was often found to be unnecessary as the region of overlap of the test and reference beams

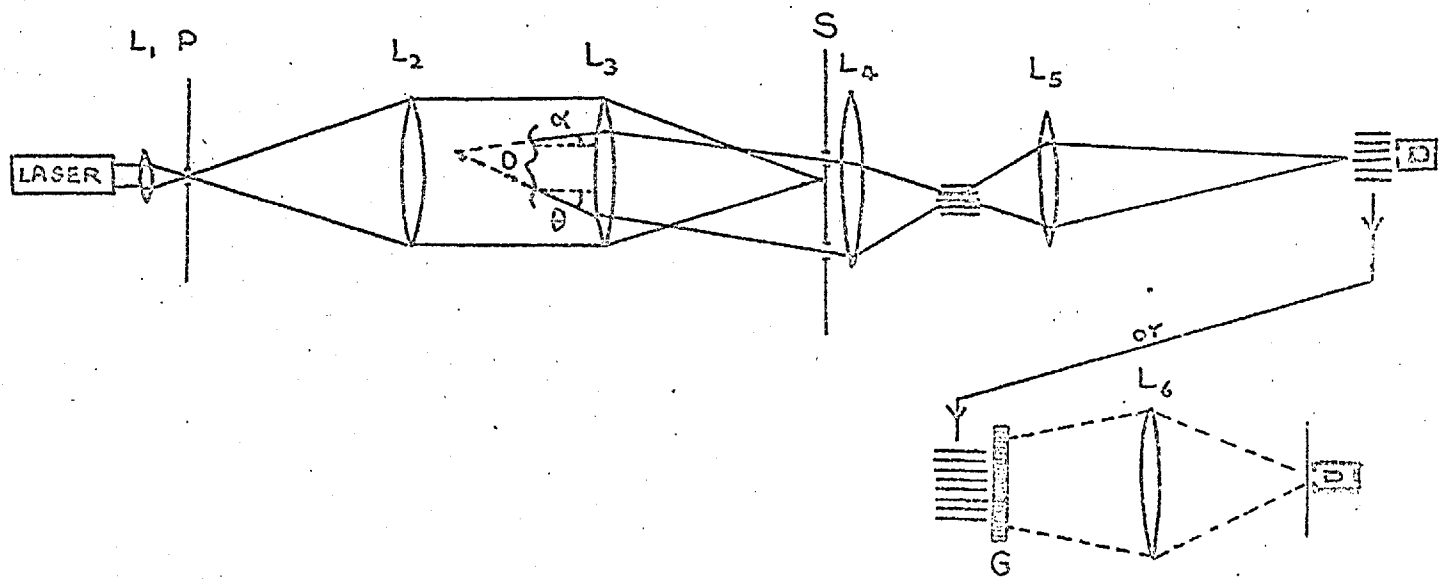

FIGURE 4.1

A practical perturbed reference beam Doppler interferometer.

was usually quite large as a result of diffraction by the selective apertures and could, therefore, be located without much difficulty. Whenever a grid G was used to increase the flux of light falling on the photodetector, it was placed in line with the fringe pattern and the lens L_6 was used to form a reduced image of the grid either directly onto the detector or onto a ground glass screen immediately in front of the detector.

4.3. LINEAR TRACK VELOCITY MEASUREMENT OF A RADIALLY RULED ROTATING GRATING.

4.3.1. Experimental details.

A preliminary test of the Doppler velocity method was made using a Scientifica and Cook Electronics B16/2 d.c. helium-neon gas laser, set to give a uniphase output of about ½mW. As the output from this laser was very low the first test had to be made on an object that was very efficient in scattering light into at least one well defined direction. A linear optical grating is ideal from this point of view. So that the Doppler shift in frequency could be continuously monitored and to make the initial setting up of the system as easy as possible, it was considered that the most suitable test object would be an effectively infinitely long continuously moving grating.

For all these reasons the first test of the Doppler velocity method was made on a radially ruled rotating grating made by Optical Measuring Tools Ltd., High Wycombe, Bucks. This grating

had 5600 lines, a mean track diameter of 9.7cm, a track width of 1.4cm, and could be rotated using a variable speed motor up to about 600 rpm. Figure 4.2 shows the optical system and illustrates how two pin holes in the schlieren blind, separated by about 1.2cm, were used to select the light scattered by the grating into the +1 and -1 diffraction orders. The width of the transluminating beam was about 4mm and the focal length of the schlieren lens was 50cm. The two diffraction orders were allowed to interfere with one another and the resulting interference pattern magnified and projected onto a 0.5mm wide entrance aperture placed in front of the photomultiplier using the two lens combination illustrated in Figure 4.1. With the motor running at approximately half speed the beat frequency signal developed across a 100kΩ resistor of the photomultiplier, set to an anode voltage of 0.7kV, was displayed on a Telequipment oscilloscope, set to a sensitivity of 0.01V/cm, and was found to correspond to approximately 50kHz.

4.3.2. Results.

The optical system illustrated in Figure 4.2 is in fact a 'perturbed reference beam' Doppler interferemeter and so the linear track velocity of the moving grating may be estimated by applying equation 3.38. Substituting $\nu_b = 5\times10^{4}$Hz, $\lambda_1 = 6.3\times10^{-5}$cm, and $\theta = d/f = 2.4\times10^{-2}$Rd into this equation gives a velocity of 130cm.s^{-1} which corresponds to a rotation of about 260 rpm. This is consistant with the speed rating of the motor.

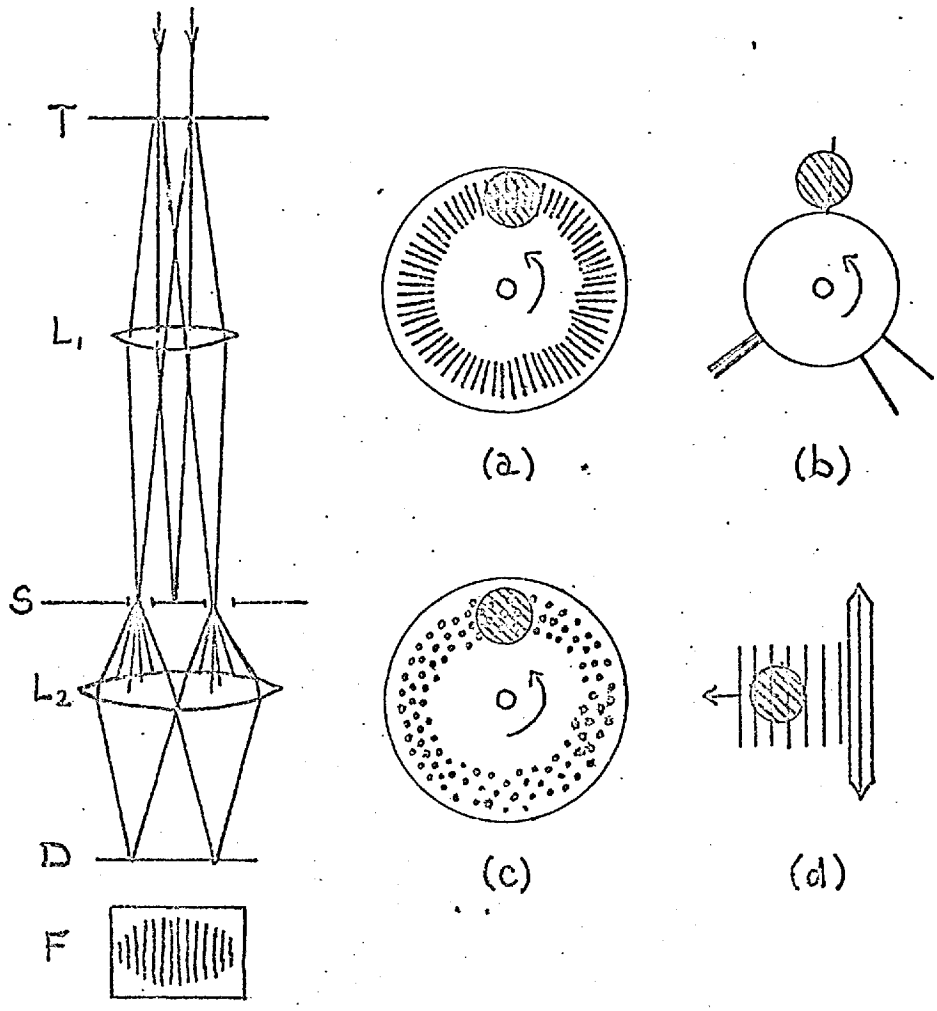

Optical system used for separating the + and - diffraction orders produced by
(a) a rotating grating,
(b) rotating spokes,
(c) rotating discs, and
(d) progressive sound waves.
T, position of test object; L_1, schlieren lens; S, schlieren blind; D, viewing plane; F, frozen fringe pattern.

FIGURE 4.2

4.4. VELOCITY MEASUREMENTS OF MOVING RODS AND DISCS.

4.4.1. Experimental details.

In this and all subsequent experiments an 8mW B18/3 laser was used. The apparatus was essentially the same as that illustrated in Figure 4.2b and c. The object whose velocity was being measured was either a wire spoke or spokes, or a transparency of an array of discs attached to the periphery of a fly wheel that was fixed to the spindle of the variable speed motor. The diameter of the wire spokes was about 0.3mm and the diameter of the discs was about 0.5mm. Figure 4.3 shows a projected image of these two objects with and without the schlieren blind in place. In both cases the two apertures in the schlieren blind selected light that was diffracted symmetrically about the optic axis. The line joining the centres of the two apertures was set parallel to the direction of motion during the time the objects were traversing the 3mm wide laser beam. To increase the sensitivity of the optical system selecting the angle of deflection a schlieren lens having a focal length of 173cm was used. In order to form fringes of good visibility in the interference pattern it was necessary to arrange the selective apertures to both coincide with the intensity maxima of the diffraction pattern ; i.e. the illumination of each pin hole should ideally be the same.

Beat frequency measurements were made by displaying and then photographing the output from the photomultiplier on a 547 Tektronix oscilloscope fitted with a 1A7 plug-in amplifier. Figure 4.4 shows oscillogram traces of the beat frequency signals obtained a) during the transit of a single spoke and b) and c) during the successive transit of two spokes. In b) the spoke separation was equal to the beam diameter and in c) equal to a spoke diameter. In all cases the anode voltage applied to the photomultiplier was 0.8kV and the

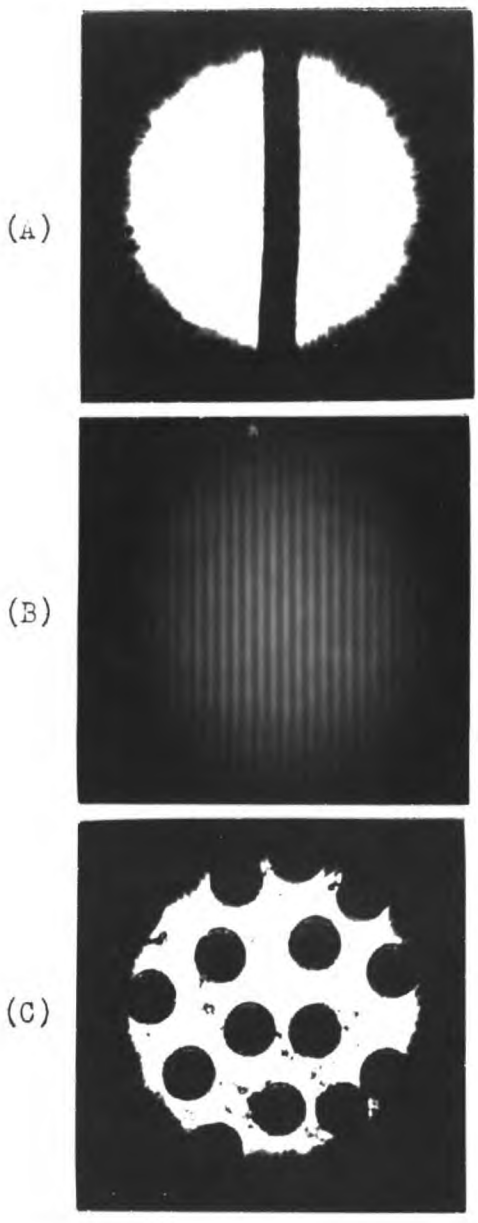

Projected image of (A) a wire and (C) an array of discs. (B) is a selective shadow of these objects obtained using the optical system in Figure 4.2

FIGURE 4.3

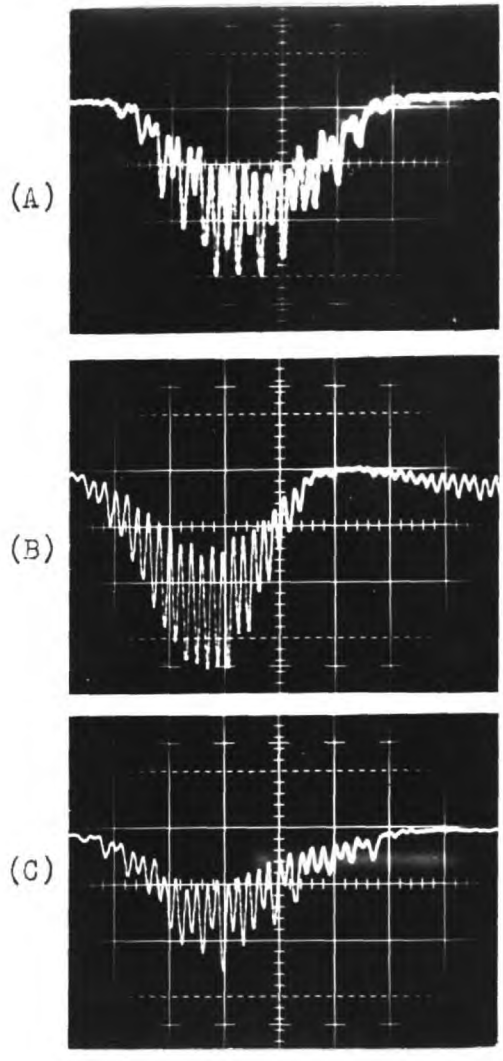

Oscillogram traces of Doppler beat frequency signals produced by (A) a single spoke, (B) two spokes separated by one laser beam diameter and (C) two spokes separated by one spoke diameter.

FIGURE 4.4.

oscilloscope sweep speed was 0.5ms/cm. The oscilloscope sensitivity in Figure 4.4a was 0.05V/cm and in Figures 4.4b and c was 0.1V/cm.

4.4.2. Results.

The beat frequency was determined from the oscillograms illustrated in Figure 4.4 by measuring the distance in which 15 oscillations occured. Assuming that the turning points of an oscillation could be determined to 1/10th of a cycle the beat frequencies were estimated to be a) 1.00×10^4Hz, b) 1.04×10^4Hz and c) 1.07×10^4Hz, all $\pm$ 1.3%.

Measurements made on the schlieren blind gave a selective aperture separation d equal to 0.772cm $\pm$ 0.2% and a mean aperture diameter of 0.041cm $\pm$ 2%. Although the distance between the schlieren blind and the schlieren lens could be measured to $\pm$ 0.2% the actual focal length of the lens cannot be defined much better (according to the manufacturer) than $\pm$ 1%.

The mean angular separation θ between the two deflected beams is given by d/f and is equal to 4.46×10^{-3}Rd. The finite size of the two pin holes makes the range of angular acceptance equal to 4.46×10^{-3}Rd $\pm$ 5.3%. If the uncertainty in the mean pin hole separation and the focal length of the schlieren lens as also taken into account the uncertainty in θ is increased by a further 1.2%.

A pin hole of finite size must transmit a range of Doppler shifted frequencies as a result of accepting a finite range of angular deflections. The frequency range $\Delta\nu'$ is equal to $u\Delta\theta/\lambda_1$. If the frequency spectrum is spread symmetrically about the centre of the pin hole the transmitted light will behave as if it is of a

single pure frequency equal to the centre frequency of the spectrum. However, this additional spread in the line width of the source works out to be less than or at most of the order of the Doppler line width of neon line of the laser and is of little consequence. It would appear from this that it is the error in measuring the mean separation of the two selective apertures that determines the uncertainty in Θ rather than the finite size of the pin holes themselves. In view of this the value of Θ is taken to be equal to 4.46×10^{-3} Rd $\pm$ 1.2%.

Substituting the above values for ν_b and Θ into equation 3.38 therefore gives for the linear velocity of the moving spokes: a) 142cm.s^{-1}, b) 148cm.s^{-1} and c) 152cm.s^{-1}, all $\pm$ 2.5%.

Examination of Figure 4.4a shows that the number of oscillations in the beat frequency signal corresponds to roughly N = 20. According to equation 3.27b if the system is beam width limited the number of recorded oscillations should be about 22. If the system is diffraction limited equation 3.35 predicts that the maximum number of oscillations that one should be able to detect in the system used here is of the order of 38 (where n has been put equal to 1 and b = d). It appears, therefore, that the system used was beam width limited and that an improvement in the accuracy of the velocity measurement could be made most easily by increasing the width of the laser beam.

4.5. VELOCITY OF SOUND MEASUREMENT.

4.5.1. Experimental details.

The Doppler velocity method was next applied to a moving phase object in the form of a progressive sound wave. This method of measuring the velocity of sound could possibly be used in the development of the 'ultra-sonic' diagnostic method described in the next chapter.

The apparatus used was the same as described in the previous section except that in this case the laser beam passed through an acoustic field generated by a 498.6kHz x-cut quartz crystal - see Figure 4.2d. Again the +1 and -1 diffraction orders were selected using a schlieren blind with two appropriately spaced selective apertures.

It was necessary to increase the frequency response of the photomultiplier circuit by reducing its load resistor from 100k to 1kΩ. To restore the output signal to a reasonable value it was necessary to increase the anode voltage applied to the photomultiplier to 1.2kV. This then gave an output beat frequency signal of approximately 0.1V peak to peak. Rather than displaying and measuring the beat frequency signal on an oscilloscope the output from the photomultiplier was fed into an Advance Electronics TC3 Timer-Counter which gave a digital record of the beat frequency accurate to 1 part in 10^6. It was found that if there was any high frequency noise on the beat frequency signal the Timer-Counter gave eratic readings. This problem was overcome by reducing the noise level of the signal fed into the Timer-Counter by first passing the

output from the photomultiplier through a wide band tuned filter.

4.5.2. Results.

The mean separation d of the two selective apertures was 3.15mm $\pm$ 0.2%. This was found from a measurement of the separation of an enlarged projection of the two diffraction orders, formed in the focal plane of the schlieren lens, using a projection system of known magnification. The foacl length of the schlieren lens was 173cm $\pm$ 1% and so the angular separation between the two diffraction orders was estimated to be 1.83×10^{-3}Rd $\pm$ 1.2%.

The beat frequency measured using the Timer-Counter was found to be 997.2kHz $\pm$ 0.0001% . This was obtained using a scan time of 10sec.

Substituting the above values for θ and ν_b into equation 3.38 gives for the velocity of sound in air, at a measured room temperature of 21.5°C, 3.47×10^4cm s^{-1} $\pm$ 1.2% (i.e. $\pm$ 0.04cm.s^{-1}). This is in good agreement with the accepted value of 3.45×10^4cm.s^{-1}.

4.6. MEASUREMENT OF THE VELOCITY OF A MOVING FLAME.

4.6.1. Experimental details.

The method was next applied to a flame, as another example of a phase object. A coal gas diffusion flame stabilized on a 'bat's wing' burner was made to move across the test space by the mechanical device illustrated in Figure 4.5. It was the aim of this study to measure the velocity of some facet of the flame, defined by the selective aperture in the schlieren blind, as it passed a

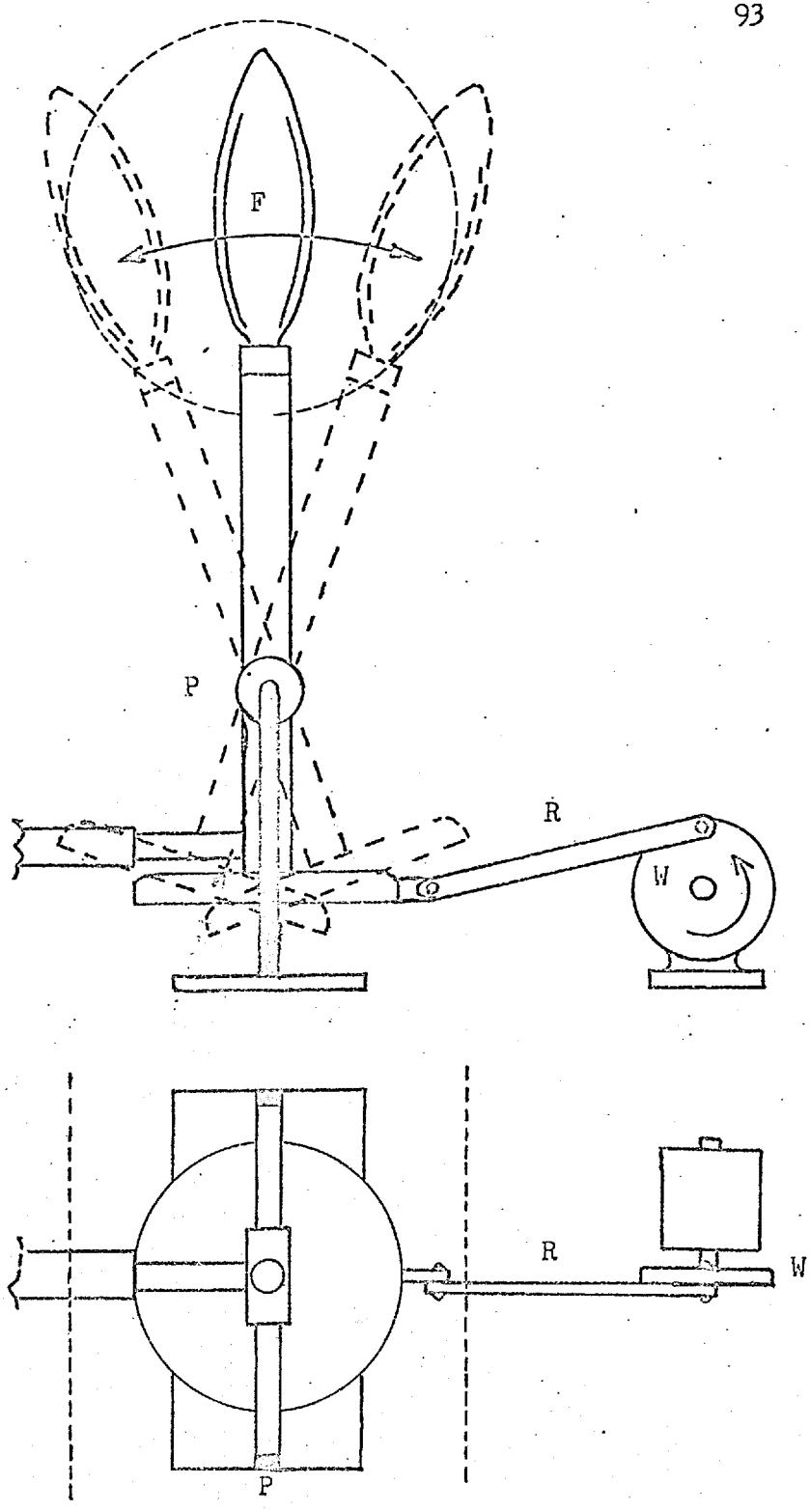

Device for mechanically moving a flame front across a transluminating light beam. F, end on view of bat's wing flame; W, fly-wheel; P, pivot; R, push rod.

FIGURE 4.5

region close to the centre of the transluminating beam.

Again a perturbed reference beam Doppler interferometer was used for this measurement. However, unlike all the previous systems used the reference beam was only very slightly perturbed. Figure 4.6 illustrates the plan view of the optical system and shows which parts of the transluminating beam were used as test and reference beams. It was necessary to attenuate the reference beam using a neutral density filter so as to match its intensity with that of the test beam. Figure 4.6d is a photograph of the filtered shadow of the flame and Figure 4.6e shows a magnified photograph of the interference fringes formed by overlapping the test and reference beams. Comparison of Figures 4.6d and 4.6a clearly illustrate which facet of the flame is defined by the selective aperture in the schlieren blind shown in Figure 4.6c.

A two lens projection system was used to focus the interference pattern, which had a fringe spacing of 0.3cm, onto a 0.05cm wide aperture placed in front of the photomultiplier. The beat frequency signal, developed across a 100kΩ load resistor of the photomultiplier set at an anode voltage of 0.8kV, was displayed and photographed on a Tektronix 547 oscilloscope.

4.6.2. Results.

The separation of the two selective apertures was 0.549cm $\pm$ 0.2%, and the diameters of the apertures were 0.050cm and 0.110cm $\pm$ 5% for the reference beam and the deflected test beam respectively. As the focal length of the schlieren lens was 173cm $\pm$ 1% the angle of deflection θ was taken to be 3.17×10^{-3}Rd $\pm$ 1.2%.

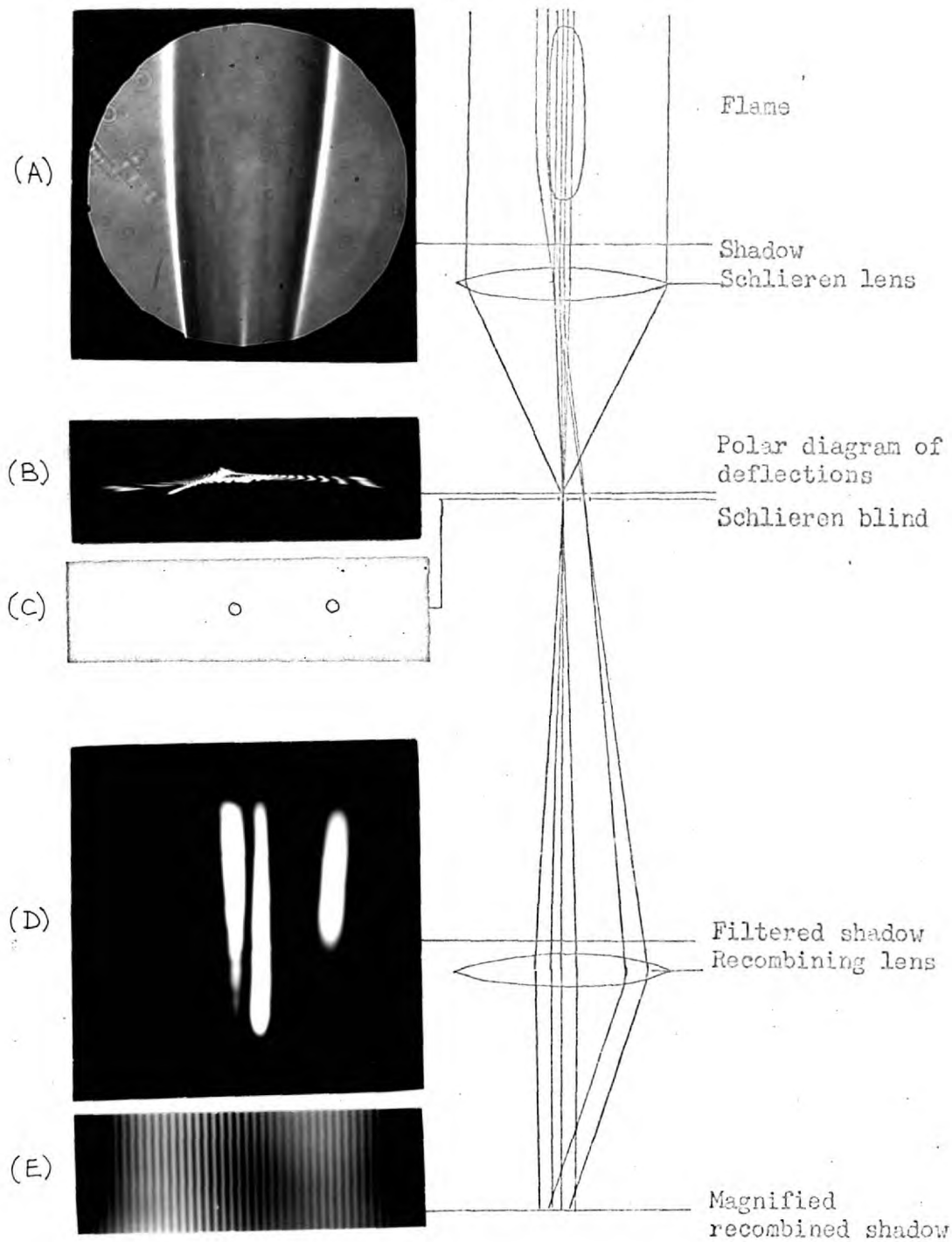

Behaviour of optical system used to measure the velocity of a moving flame front.

FIGURE 4.6

Figure 4.7 shows the resulting oscillogram trace as the fringe pattern, shown below, moves across the photodetector. The beat frequency determined from this oscillogram trace, which was recorded at a sweep speed of 10ms/cm and at a sensitivity of 0.2V/cm, was estimated to be 362Hz $\pm$ 1.3% by averaging over 15 cycles.

Substituting the above values for θ and ν_b into equation 3.38 gives a value of 7.20cm.s^{-1} $\pm$ 2.5% for the mean velocity of the flame front during the period of the measurement.

Taking N = 15 to be the number of recorded beats equation 3.27b shows that this velocity measurement represents an average velocity over a transluminating beam width of 0.3cm. Multiplying this value by the fractional error in the velocity measurement gives a figure equal to $0.4\lambda_1/\theta$, which is in good agreement with the uncertainty relationship previously proposed in Chapter 3.

4.7. CONCLUSIONS.

It has been confirmed that the theory proposed in Chaper 3 to explain the principle of the Doppler velocity method satisfactorily describes all the observations made on moving solid and phase objects. From a practical point of view it has been found that the alignment of the perturbed reference beam Doppler interferometer is particularly simple and that interference between the deflected and reference beams can often be obtained without complete overlap of the two beams. Velocities from a few centimeters per second up to the speed of sound have been

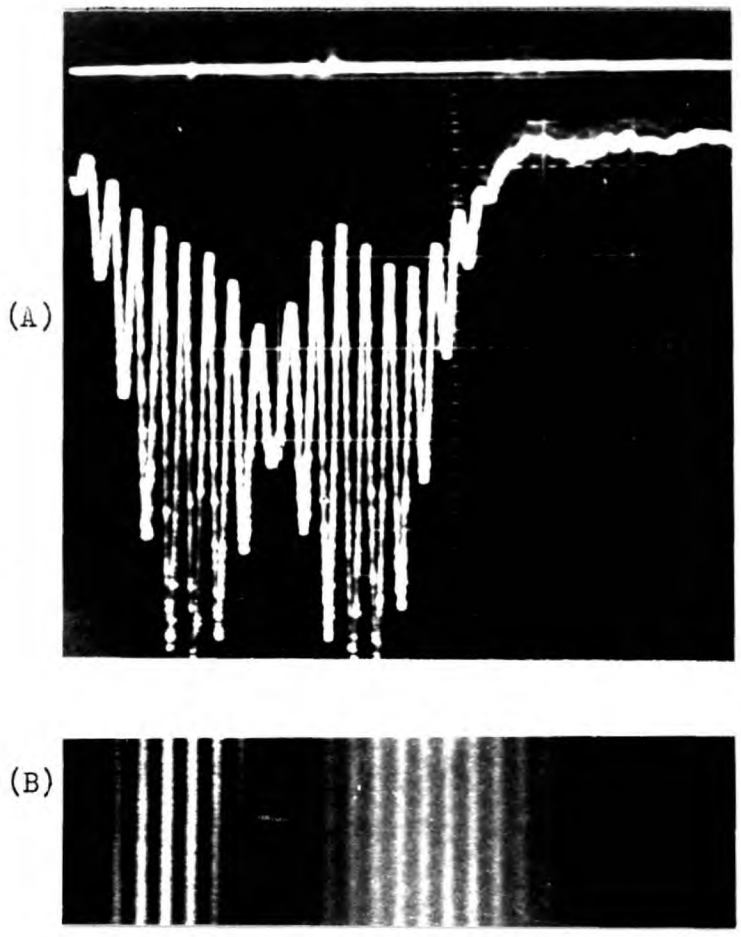

(A) Oscillogram trace of Doppler beat frequency signal produced by a moving flame as the fringe pattern (B) moves across the photodetector.

FIGURE 4.7

measured with an error of between 1.2 to 2.5%.

It would appear that the uncertainty relationship given by equation 3.42b may be used for assessing, at least approximately, the limitations of the Doppler velocity method. To assess the potentialities of the method to propagating combustion phenomena it is necessary to know the maximum angle Θ through which the transluminating beam is deflected. In general Θ increases with increasing velocity and is greatest for detonation and shock fronts and smallest for flames having the lowest burning velocities. For a premixed flame having a burning velocity of $50 cm.s^{-1}$ and a 1cm beam traverse Θ is of the order of 10^{-2}Rd. If the wavelength of the transluminating beam is 6.3×10^{-5}cm, $\lambda/\Theta = 6.3 \times 10^{-3}$cm and so if the velocity u is to be measured correct to 1% the beam width, or the distance over which the velocity measurement is averaged, must be at least 6.3mm. In the case of detonation and shock fronts the angle of deflection is given by $(2\delta)^{\frac{1}{2}}$ where δ depends on the temperature, pressure and composition changes that occur across the front. For a (large) deflection of 10^{-1}Rd and a beam traverse of 1cm the beam width need be only 0.63mm for the error in the velocity measurement to be of the order of 1%. These distance estimates have been calculated using an uncertainty relationship derived on the basis that the beat frequency could be measured to the nearest whole cycle. If it is possible to measure to a fraction of a cycle the distances calculated here may be reduced proportionately.

CHAPTER 5

THE ULTRA-SONIC METHOD OF GAS DIAGNOSTICS

5.1. INTRODUCTION.

The tendency in combustion to work at ever higher temperatures necessitates the development of special diagnostic techniques. Apart from being at a high temperature combustion systems may also be highly luminous, for example in augmented flames and plasma jets, and even transient as in travelling detonations and shock fronts. The extreme brightness, monochromaticity and the possibility of extremely short duration Q-switched pulses makes a laser an ideal light source for studying such systems. Many of the purely optical methods of gas diagnostics depend on the variation of the refractive index with temperature and composition. However, the temperature dependence of the refractive index of a gas decreases with increasing temperature and such methods are not always suited to high temperature diagnostics. Because of this the possibility of a combined ultra-sonic and optical diagnostic method has been investigated. Apart from the desirability of having a new diagnostic tool capable of furnishing additional information on both temperature and composition, an ultra-sonic method has certain advantages over purely optical methods. For example a $100^{\circ}K$ change in temperature in air at $1080^{\circ}K$ produces a 4.2% change in the velocity of sound and it may well be easier to measure this

velocity change than it would be to interpret the significance of a 1/10th of a fringe shift in a 1cm thick column of air undergoing a similar temperature change.

The measurement of the velocity of sound as a diagnostic tool was first proposed by Mayer[42] in 1873. Suits[43] developed a method using a weak shock wave originating from an electric spark, and obtained its velocity from a streak photograph. The method has been improved by Edels and Whittaker[44] who were able to use somewhat stronger shock waves. Rather than following a propagating shock front Marlow, Nisewanger and Cady[45] were able to determine the spatial distribution in the velocity of sound behind a shock wave from an instantaneous photograph of the wavefronts in an ultra-sonic beam. Non-visual sound velocity measurements have been made[46,47] using a pulsed ultra-sonic beam technique in which the transit time between a transducer and receiver is measured electronically.

This investigation is intended to examine whether or not it is possible to obtain the spatial distribution of the velocity of sound from an instantaneous photograph of an ultra-sonic beam propagating through hot gases from a burner port or jet. If it is possible one could then use sound waves to assist, for example, in finding the spatial distribution of temperature and composition in the boundary layer produced by rapidly quenching a simple reaction. A system relevant to combustion is the rapid quenching of dissociated oxygen issuing from an oxygen plasma jet by aspirating the hot gas through a cooled porous heat sink. If the flow

distribution within the gas can also be determined this would then provide a new method of measuring reaction rates at high temperatures.

After initially discussing the various factors that affect the propagation of ultra-sonic waves in gases the results of a preliminary investigation into the visualization of ultra-sonic waves in air at room temperature are given. These results are then used as a basis for solving the more difficult problems of the visualization of sound waves in gas flows which are discussed in the next chapter.

5.2. PROPAGATION OF SOUND WAVES IN GASES.

5.2.1. Introduction.

To apply the ultra-sonic method it is necessary to know how the velocity of sound depends on the temperature and composition of the gas, and what factors affect the amplitude and hence visualization of the pressure waves. This can be found by setting up and solving the equation of motion describing particle displacement in a compressible fluid. The wave equation for particle displacement ξ in an ideally perfectly compressible fluid in a one dimensional system[48a] is

$$\frac{d^2\xi}{dx^2} = \frac{d\rho}{dp}\frac{d^2\xi}{dt^2} \qquad \ldots 5.1$$

where p and ρ are respectively the fluid's pressure and density. It follows that a disturbance travels through the fluid with a velocity v equal to

$$v = \left(\frac{dp}{d\rho}\right)^{\frac{1}{2}} \qquad \ldots 5.2$$

Further simplification requires a krowledge of the equation of

state of the fluid. When the disturbance is sinusiodal and of frequency ν_s a solution of equation 5.1 is

$$\mathcal{E} = \mathcal{E}_0 \sin 2\pi\nu_s\left[t - \frac{x}{v}\right] \qquad \ldots 5.3$$

For ideal gases equation 5.2 may be simplified using Boyle's law. For real gases it is generally sufficient to use an equation of state that includes the second virial coefficient[49]. Thorpe[50] has calculated, using such an equation, that for ethylene at 25°C and at one atmosphere the velocity of sound is 0.36% below the ideal gas value. At higher temperatures the departure from the ideal value would be expected to be even less than this. However, as it is not anticipated to be able to measure the velocity of sound to better than ½% the ideal gas equation for the velocity of sound is considered to be sufficiently accurate for present purposes. If the above wave equation is modified[48b] to take into account the various loss mechanisms that exist in a real fluid the solution becomes

$$\mathcal{E} = \mathcal{E}_0 e^{-\alpha x} \sin 2\pi\nu_s\left[t - \frac{x}{v}\right] \qquad \ldots 5.4$$

The various factors that determine the velocity of sound v and govern the magnitude of the attenuation coefficient α are discussed below. This is followed by an examination of the various ways in which a sound wave can mark a transluminating light beam.

5.2.2. Velocity of sound.

As it is sufficient to consider most gases to obey Boyle's law equation 5.2 becomes

$$v = \left[\frac{RT}{M}\left(1 + \frac{R}{C_v}\right)\right]^{\frac{1}{2}} \qquad \ldots 5.5$$

where R is the universal gas constant, T is the absolute temperature, M is the molecular weight and C_v is the specific heat of the gas at constant volume. In the case of gas mixtures M and C_v appearing in this last equation must be replaced by an effective molecular weight $\bar{M}$, and an effective specific heat $\bar{C}_v$. These two quantities may be evaluated from a knowledge of the partial pressures of the various constituents[43,51]. Thus,

$$\bar{M} = \frac{\Sigma p_i M_i}{\Sigma p_i} \qquad \ldots 5.6$$

$$\bar{C}_v = \frac{\Sigma p_i C_{vi}}{\Sigma p_i} \qquad \ldots 5.7$$

Dispersion[48a] occurs in the velocity of sound whenever the time required for the exchange of heat between the various degrees of freedom and states of equilibrium of a gas is comparable with the heating and cooling period of the compression wave. In a pure nonreacting gas time lags exist in the transfer of energy from translational to rotational and vibrational energy states. It is the transfer of energy to vibrational states that is of most interest here. At sufficiently low frequencies it is possible for this exchange of energy to be complete while at high frequencies this may well not be so. If C_o and C_∞ represent the limiting low frequency and high frequency specific heats the velocity of sound is given by

$$v = \left\{ \frac{RT}{M} \left[1 + R \left(\frac{C_o + C_\infty \omega^2 \tau^2}{C_o^2 + C_\infty^2 \omega^2 \tau^2} \right) \right] \right\}^{\frac{1}{2}} \qquad \ldots 5.8$$

where $\omega = 2\pi\nu_s$ and τ is the relaxation time for the departure from equilibrium to be reduced to 1/e of its original value. When $\omega\tau \gg C_o/C_\infty$ the velocity of sound v_∞ is given by

$$v_\infty = \left[\frac{RT}{M}\left(1 + \frac{R}{C_\infty}\right)\right]^{\frac{1}{2}} \qquad \ldots 5.9$$

Similarly when $\omega\tau \ll C_o/C_\infty$ the velocity of sound v_o is given by

$$v_o = \left[\frac{RT}{M}\left(1 + \frac{R}{C_o}\right)\right]^{\frac{1}{2}} \qquad \ldots 5.10$$

The point of inflection of equation 5.8 occurs at a frequency ν_i given by

$$\nu_i = \frac{1}{2\pi\tau}\left(\frac{C_o}{C_\infty}\right) \qquad \ldots 5.11$$

At low temperatures vibrational energy states contribute only slightly to the specific heat of a gas and so C_o/C_∞ is only very slightly greater than unity. Consequently dispersion effects are small. At very high temperatures more and more vibrational states contribute to the specific heat and so C_o/C_∞ increases. For a diatomic gas this ratio has a maximum classical value of 1.4. ν_i can be calculated from equation 5.11 providing τ is known. The dependence of $1/2\pi\tau$ on temperature has been calculated from the list of experimentally determined relaxation times τ tabulated by Cottrell and McCoubrey[48] and graphs of this dependence are given in Appendix 1 for a number of gases of interest.

Velocity dispersion also occurs in a reacting system. In the case of a partially dissociated gas the velocity of sound is given by[43]

$$v = \left\{\frac{RT}{M}\left[1 + R\left(\frac{k^2AB + C_v\omega^2}{k^2B^2 + C_v^2\omega^2}\right)\right]\right\}^{\frac{1}{2}} \qquad \ldots 5.12a$$

where A and B are given by

$$A = \left[\frac{2D}{RT} - \frac{C_v}{R}\right]\left[\frac{1-f}{1+f}\right] + \left[\frac{2-f}{f}\right] \qquad \ldots 5.12b$$

$$B = \left[\frac{D^2}{RT^2}\right]\left[\frac{1-f}{1+f}\right] + C_v\left[\frac{2-f}{f}\right] \qquad \ldots 5.12c$$

k is the rate constant of the reaction, D is the dissociation energy and f is the fraction dissociated. At high frequencies this equation greatly simplifies to

$$v_\infty = \left[\frac{RT}{M}\left(1 + \frac{R}{C_v}\right)\right]^{\frac{1}{2}} \qquad \ldots 5.13$$

M and C_v appearing in these last two equations apply to the gas mixture and may be evaluated using equations 5.6 and 5.7. The simplicity of equation 5.13 arises because the period of oscillation is very short compared with the time required for the reaction to proceed to its new equilibrium state. Providing one works well away from the centre of a vibrational dispersion band equation 5.13 is only a function of temperature and composition.

5.2.3. The attenuation of sound.

The amplitude displacement ξ of a propagating sound wave may be attenuated as a result of viscous and heat conduction losses, and also as a result of dispersion losses. Thus the attenuation coefficient α appearing in equation 5.4 may be written as the sum $(\alpha_v + \alpha_h + \alpha_d)$ where α_v, α_h and α_d are the viscous, heat conduction and dispersion attenuation coefficients respectively.

α_v and α_h are given by[52a]

$$\alpha_v = \frac{2\pi^2 \nu_s^2}{v^3} \frac{4\eta}{3\rho} \qquad \ldots 5.14$$

$$\alpha_h = \frac{2\pi^2 \nu_s^2 (\gamma - 1) K}{v^3 C_p} \qquad \ldots 5.15$$

where ν_s and v are frequency and velocity of sound, η is the viscosity, ρ the density, γ the ratio of specific heats (C_p/C_v), K the thermal conductivity, and C_p the specific heat at constant pressure of the transmitting gas. When K is replaced by the kinetic theory expression[53]

$$K = \frac{(9\gamma - 5)\eta C_v}{4} \qquad \ldots 5.16$$

one obtains for the combined viscous and corduction attenuation coefficients

$$\alpha_v + \alpha_h = \frac{2\pi^2 \nu_s^2 \eta}{v^3 \rho} \left[\frac{4}{3} + \frac{(\gamma - 1)(9\gamma - 5)}{4} \right] \qquad \ldots 5.17$$

This equation has been used to calculate $(\alpha_v + \alpha_h)/\nu_s^2$ for a number of gases and temperatures and these are tabulated in Table 4.

α_d is given by[48e]

$$\alpha_d = \frac{2\nu_s \nu_m \alpha_m}{(\nu_s^2 + \nu_m^2)} \qquad \ldots 5.18$$

where

$$\nu_m = \frac{v_o}{v_\infty} \nu_i \ , \qquad \ldots 5.19$$

is the frequency at which the dispersion attenuation is a maximum and equal to α_m where

$$\alpha_m = \frac{\pi \nu_s}{2v} \left[\frac{v_\infty^2 - v_o^2}{v_o v_\infty} \right] \qquad \ldots 5.20$$

To evaluate equation 5.18 it is necessary to make use of the

expressions for v_o and v_{co} given in section 5.2.2. This in turn requires a knowledge of the contribution that vibrational energy states make to the total specific heat of the gas. This difficulty does not exist when experimental data on v_o and v_{oo} are available. In principle it is possible to make the effects of α_d small by working at a frequency well away from the centre of the dispersion band.

TABLE 4

Sound attenuation coefficients

$\alpha = \alpha_v + \alpha_h$

GAS	$\frac{\alpha_v}{\alpha}$	$\frac{\alpha_h}{\alpha}$	$\frac{\alpha}{v_s^2} \times 10^{13}$		
			273°K	1000°K	3000°K
Air	0.71	0.29	1.34	1.72	1.87
N_2	0.71	0.29	1.29	1.61	1.68
O_2	0.71	0.29	1.60	2.08	2.27
CH_4	0.77	0.23	0.62	0.86	1.02
CO_2	0.78	0.22	1.50	2.07	2.64
Ar	0.57	0.43	1.89	1.99	2.22

5.3. REFRACTIVE INDEX VARIATIONS IN AN ACOUSTIC BEAM.

5.3.1. Introduction.

An expression is derived below relating the refractive index variations in an acoustic beam to the beam's mean acoustic power density assuming sinusoidal pressure waves. This is then used to compare the various methods of marking a transluminating light beam and to assess their temperature dependence.

5.3.2. Pressure variations in an acoustic beam.

The instantaneous pressure disturbance in an acoustic beam is given by[54a]

$$\hat{p} = v^2 \rho \frac{d\xi}{dx}, \qquad \ldots 5.21$$

where in the absence of attenuation ξ is given by equation 5.3. Differentiating equation 5.3 and then substituting into equation 5.21 therefore gives the following expression for the pressure variations in an acoustic beam

$$\hat{p} = \hat{p}_o \cos 2\pi\nu_s \left[t - \frac{x}{v}\right] \qquad \ldots 5.22a$$

where

$$\hat{p}_o = \xi_o 2\pi\nu_s \rho v \qquad \ldots 5.22b$$

5.3.3. Mean power density of an acoustic beam.

The mean power density P is given by the sum of the mean kinetic and potential energy densities multiplied by the velocity of sound[54b]. I.e.

$$P = \frac{\xi_o^2 4\pi^2 \nu_s^2 \rho v}{2} \qquad \ldots 5.23$$

5,3.4. Optical marking by an acoustic beam.

For adiabatic pressure changes the refractive index n of a gas is related to its instantaneous pressure p by[6a]

$$\delta = \delta_o \left[\frac{p}{p_o}\right]^{1/\gamma} \qquad \ldots 5.24$$

where $\delta = n - 1$ and δ_o is the value of δ at some reference pressure p_o. If the ambient pressure is p_a the local pressure p in the acoustic beam is equal to

$$p = p_a + \hat{p}_o \cos 2\pi\nu_s\left[t - \frac{x}{v}\right] \qquad \ldots 5.25$$

The instantaneous value of δ in the acoustic beam is therefore

$$\delta = \delta_o\left(\frac{p_a}{p_o}\right)^{1/\gamma}\left[1 + \frac{\hat{p}_o}{\gamma p_a}\cos 2\pi\nu_s\left(t - \frac{x}{v}\right)\right] \qquad \ldots 5.26$$

where it is assumed that the amplitude of the pressure wave is very small compared with the ambient pressure. By combining equations 5.22 and 5.23 it is possible to express $\hat{p}_o$ in terms of the mean acoustic power density of the acoustic beam, i.e.

$$\hat{p}_o = (2P\rho v)^{\frac{1}{2}} \qquad \ldots 5.27$$

Equation 5.26 can be used as a basis for assessing the magnitude of the marking of the transluminating light beam when using interferometry, deflection mapping and shadowgraphy.

In interferometry the degree of marking, i.e. the number of interference fringes, depends on the optical path difference between regions of compression and rarefaction. If Z is the thickness of the acoustic beam the number of interference fringes N is given by

$$N = \frac{Z}{\lambda_o}(\delta_{max} - \delta_{min}) \qquad \ldots 5.28$$

where δ_{max} and δ_{min} are the maximum and minimum values of δ given by equation 5.26 and λ_o is the wavelength of the transluminating light beam. Substituting equations 5.26 and 5.27 into equation 5.28 gives

$$N = \frac{2Z\delta_o}{\gamma\lambda_o p_o^{1/\gamma} p_a^{(1-1/\gamma)}}(2P\rho v)^{\frac{1}{2}} \qquad \ldots 5.29$$

In deflection mapping the angular deflection θ of a transluminating light beam is given by[6b]

$$\theta = \frac{d\delta}{dx} Z \qquad \ldots 5.30$$

where $d\delta/dx$ can be found by differentiating equation 5.26. Hence

$$\frac{d\delta}{dx} = \delta_o \left[\frac{p_a}{p_o}\right]^{1/\gamma} \frac{2\pi\nu_s}{\gamma p_a} \left[\frac{2P\rho_o}{v}\right]^{\frac{1}{2}} \sin 2\pi\nu_s \left[t - \frac{x}{v}\right] \qquad \ldots 5.31$$

where p_o has been replaced by equation 5.27. The maximum angular deflection is therefore given by

$$\theta_{max} = \delta_o \left[\frac{p_a}{p_o}\right]^{1/\gamma} \frac{2\pi\nu_s}{\gamma p_a} \left[\frac{2P\rho_o}{v}\right]^{\frac{1}{2}} Z \qquad \ldots 5.32$$

In shadowgraphy the fractional change in illumination brought about by stretching or compressing, but not folding, an initially planar wavefront is given by[6c]

$$\frac{\Delta I}{I} = \frac{d^2\delta}{dx^2} Z\, l \qquad \ldots 5.33$$

where l is the distance from the centre of the sound beam to the viewing screen. Differentiating equation 5.31 and substituting into equation 5.33 gives

$$\frac{\Delta I}{I} = \delta_o \left[\frac{p_a}{p_o}\right]^{1/\gamma} \frac{4\pi^2\nu_s^2}{\gamma p_a} \left[\frac{2P\rho_o}{v^3}\right]^{\frac{1}{2}} Z\, l \cos 2\pi\nu_s \left[t - \frac{x}{v}\right] \qquad \ldots 5.34$$

The maximum fractional change in illumination in the shadow record of a sound wave is therefore

$$\frac{\Delta I}{I} = \delta_o \left[\frac{p_a}{p_o}\right]^{1/\gamma} \frac{4\pi^2\nu_s^2}{\gamma p_a} \left[\frac{2P\rho_o}{v^3}\right] Z\, l \qquad \ldots 5.34$$

Equations 5.29, 5.32 and 5.35 can be used to estimate the degree of marking in the various types of optical records of

sinusoidal sound waves. They show how this marking depends on the acoustic power density and frequency and may also be used to show how it varies with gas temperature. For air at NTP and a light beam of 0.589μm these three equations may be expressed in a more convenient form as follows

$$N = 6.5\times10^{-3} P^{\frac{1}{2}} Z \qquad \ldots5.36a$$

$$\theta_{max} = 3.6\times10^{-6} P^{\frac{1}{2}} Z \nu_s \text{ Radians} \qquad \ldots5.36b$$

$$\frac{\Delta I}{I} = 6.9\times10^{-3} P^{\frac{1}{2}} Z \nu_s^2 l \qquad \ldots5.36c$$

where P is in $mW.cm^{-2}$, Z and l are in cm, and ν_s is in MHz. Because ρ and v are functions of temperature it follows that the marking will also be temperature dependent. If the pressure is kept constant

$$N \propto T^{-0.25} \qquad \ldots5.37a$$

$$\theta_{max} \propto T^{-1.50} \qquad \ldots5.37b$$

$$\frac{\Delta I}{I} \propto T^{-1.25} \qquad \ldots5.37c$$

Normalized plots of these temperature dependences are shown in Figure 5.1.

5.4. THE TRANSDUCER.

5.4.1. Introduction.

The basic requirement of the transducer is that it must be capable of producing effectively plane sound waves of known frequency. For good visualization the effective width of the acoustic beam should be as large as possible. Limitations in its width may arise either from the finite cross sectional area of the

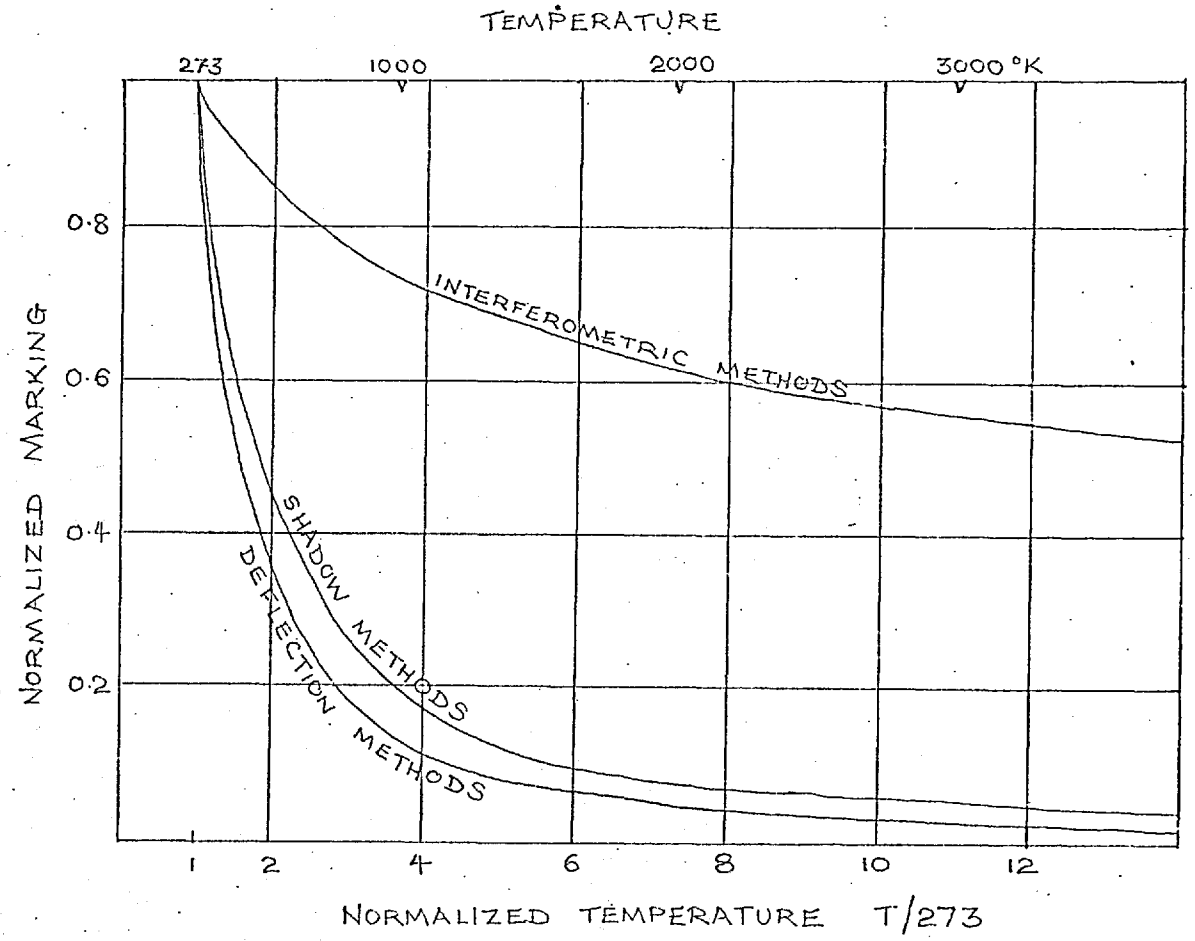

Normalized temperature ddpendence of the three optical methods of visualizing sinusoidal acoustic pressure waves.

FIGURE 5.1

transducer or from the nature of the system being studied.

The minimum frequency of the transducer is set by the required spatial resolution of the velocity measurement. This is clearly set by the wavelength of the sound waves. Ideally for the best spatial resolution the highest possible frequency should be used. Unfortunately, however, the attenuation of sound waves, as a result of viscous and conduction losses, increases as ν_s^2. Table 5 shows how the attenuation distance (defined as α^{-1}) in air depends on the frequency of the sound waves. The attenuation distance in other gases may be calculated using the data in Table 4.

TABLE 5

Sound attenuation distances in air

Temperature ^oK	Attenuation distance $1/\alpha$ (cm)			
	0.5MHz	0.7MHz	1.0MHz	2.0MHz
273	30.0	15.4	7.6	1.9
1000	23.4	11.8	5.8	1.5
3000	21.4	11.0	5.4	1.4

It is clear that frequencies much greater than 2MHz would be too strongly attenuated to be of any practical use and this, therefore, represents an upper frequency limit.

As dispersion attenuation can be even greater than that produced by viscous and conduction losses it is necessary to work at a frequency well away from the centre of a dispersion band. The approximate centre frequency of these bands for a number of gases at various temperatures may be estimated from the curves in Appendix 1. When the coupling medium between the

transducer and the test gas is air and its temperature ranges from about 300°K up to about 1000°K it is seen that the sound frequency must be kept much greater than 0.025MHz to avoid strong dispersion attenuation. This represents a lower frequency limit. When the ultra-sonic method is applied to the study of an oxygen plasma jet having a temperature of up to say 3000°K the curves in Appendix 1 show that the lower frequency limit is increased and should now be much greater than 0.1MHz.

Of all the ultra-sonic transducers reviewed by Carlin[58a] the only one capable of generating sound waves in the frequency range 0.5MHz to 2.0MHz is an electrically driven piezoelectric x-cut quartz crystal oscillator. The thickness of a piezoelectric crystal decreases with increasing frequency. As it is easier to cut and to mount a thick crystal it was finally decided to have two 5cm diameter x-cut quartz crystal discs made (by Gooch and Housego Ltd. in conjunction with Brooks Crystals Ltd., Cornhill Factory, Illminster, Somerset) having thickness vibrational frequencies corresponding to 0.5MHz and 0.7MHz. The methods used for mounting, driving and monitoring these crystals are now described.

5.4.2. Transducer construction and performance.

The crystal mountings used were based on a design described by Arnold, McCoubrey and Ubbelohde[56] and are illustrated in Figure 5.2. The crystals had an approximately 70 degree bevel and were held by three equispaced mounting clamps that located onto the apex of the bevel. The crystal faces were either gold or

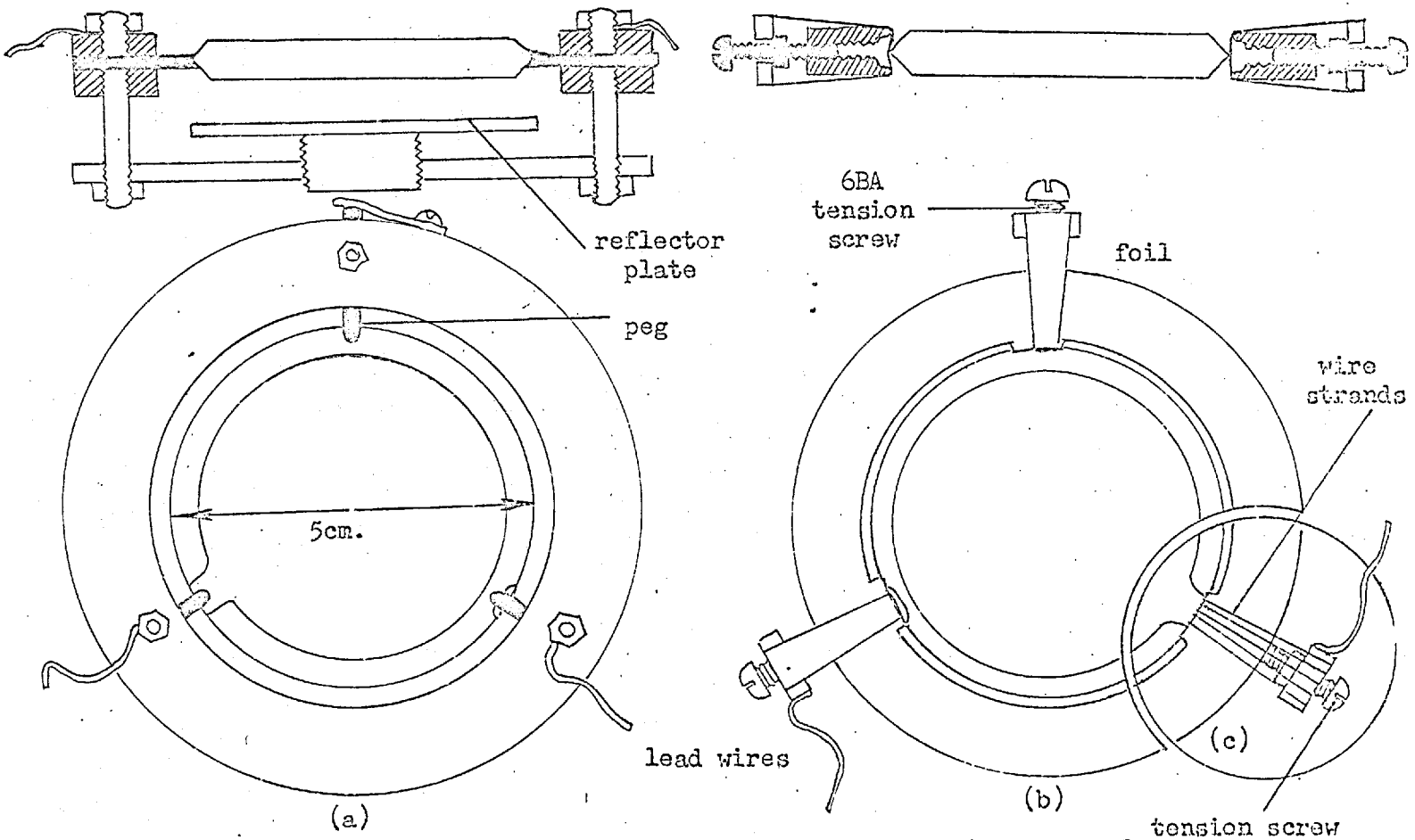

FIGURE 5.2

Crystal holder designs. (a) peg clamps and reflector plate, (b) foil clamps, (c) wire clamps.

silver coated. Electrical connection was made between each of the coated crystal faces and two of the three clamps, which also acted as terminals, via narrow metallic tongues deposited across the bevelled area. The tongues were made of a soft solder and were a few thousandth of an inch thick. It was not possible to solder lead wires directly onto the crystal faces or even onto the tongues as the resulting damping proved to be too great.

Three different clamp designs were tried. The first consisted of three brass pins, one of which was spring loaded, having V-shaped cut-outs at their tips for locating onto the apex of the crystal's bevel - see Figure 5.2a. The second type consisted of three copper foils held under tension as illustrated in Figure 5.2b. The tension in each foil could be adjusted independently by turning the appropriate tension screw. With this design the area of contact between the clamp and crystal could be made very small. In the third type of clamp three or four strands of wire were used in place of each copper foil. This has the advantage of reducing the area of contact even more. However, there is a practical limit as the clamp must be able to withstand the mechanical vibrations and local heating that occurs when the crystal is oscillating. It was noticed that wear occured both in the wire and foil clamps as well as in the soft solder tongues over the area of contact with the clamps. Strengthening the tongues at the apex of the bevel by using a small piece of gold foil proved unsatisfactory because of the additional damping. As wear was less using the copper foil clamp this was the design finally adopted whenever high acoustic power densities

were needed.

A single valve self oscillating circuit was used to drive the crystal[55b]. This had the advantage of being able to operate at both low and high powers by simply adjusting the supply voltage between 100V and 420V. Details of the circuit are shown in Figure 5.3. It was found to work satisfactorily, without modification, at both 0.5MHz and 0.7MHz. The acoustic power output was strongly dependant on the damping in the crystal mounting and on the values of the capacitors C_1, C_2 and C_3. The values indicated were those giving maximum power output.

Regarding performance, the quantities of interest are: constancy of frequency, uniformity of amplitude over the crystal face, and the magnitude of the acoustic power density. The power density was monitored using a torsion-wire acoustic wattmeter and is described in section 5.4.3.

The frequency of the two crystals showed an insignificant negative drift of the order of 1 part in 10^5 as the power output was increased from 75mW.cm^{-2} to 200mW.cm^{-2}. The frequencies of the two crystals, when operated at 75mW.cm^{-2} were measured on a TC3 Advance Electronics Timer Counter and found to be 0.49862MHz and 0.69960MHz.

To check the uniformity of the amplitude of oscillation over the crystal face the optical system illustrated in Figure 5.4 was set up. In this arrangement the upper face of the crystal was given a mirror finish by coating it with silver. This enabled straight line wedge fringes to be formed as a result of interference

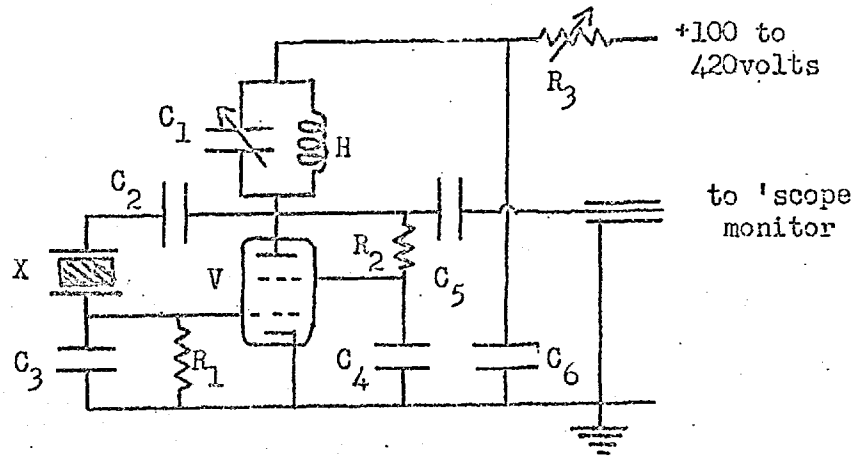

R_1 = 470kΩ	C_3 = 330pF
R_2 = 100kΩ	C_4 = 0.25μF
R_3 = 20kΩ	C_5 = 0.01μF
C_1 = 150pF	C_6 = 0.01μF
C_2 = 1800pF	H = 2mH
V = 5B/254M	X = 0.5MHz or 0.7MHz

Transducer Circuit.

FIGURE 5.3

between light reflected off the crystal face and off an inclined glass slab placed a few millimeters above the crystal. A 3mW helium-neon gas laser was used as a light source. As a dark fringe changes to a bright fringe whenever the optical path difference between the two interfering beams changes by $\frac{1}{2}\lambda$ (i.e. the crystal face is displaced by $\pm \lambda/8$) the observed time averaged fringe pattern becomes washed out whenever the change in path length exceeds $\frac{1}{2}\lambda$. Figure 5.5 shows the appearance of the interference pattern a) when the crystal is not oscillating, b) when it is oscillating at a power output of 60mW.cm^{-2} and c) when it is oscillating at 220mW.cm^{-2}. These photographs show that as the power output is increased so more and more of the crystal face has an amplitude of vibration exceeding $\lambda/8$. Although the crystal is clearly not vibrating uniformly, the regions having a large amplitude of vibration are randomly distributed over the crystal's surface and so the transducer should prove to be a satisfactory source of effectively plane ultra-sonic waves.

5.4.3. Acoustic power considerations and its monitoring.

The acoustic power densities needed for their visualization using interferometry, deflection methods and shadowgraphy may be assessed using equations 5.36 and 5.37. The normalized temperature dependence of the methods has been plotted in Figure 5.1. The marking produced by sound waves of a given frequency and power density at 1000°K and 3000°K is shown in Table 6 as a fraction of the marking produced at 273°K.

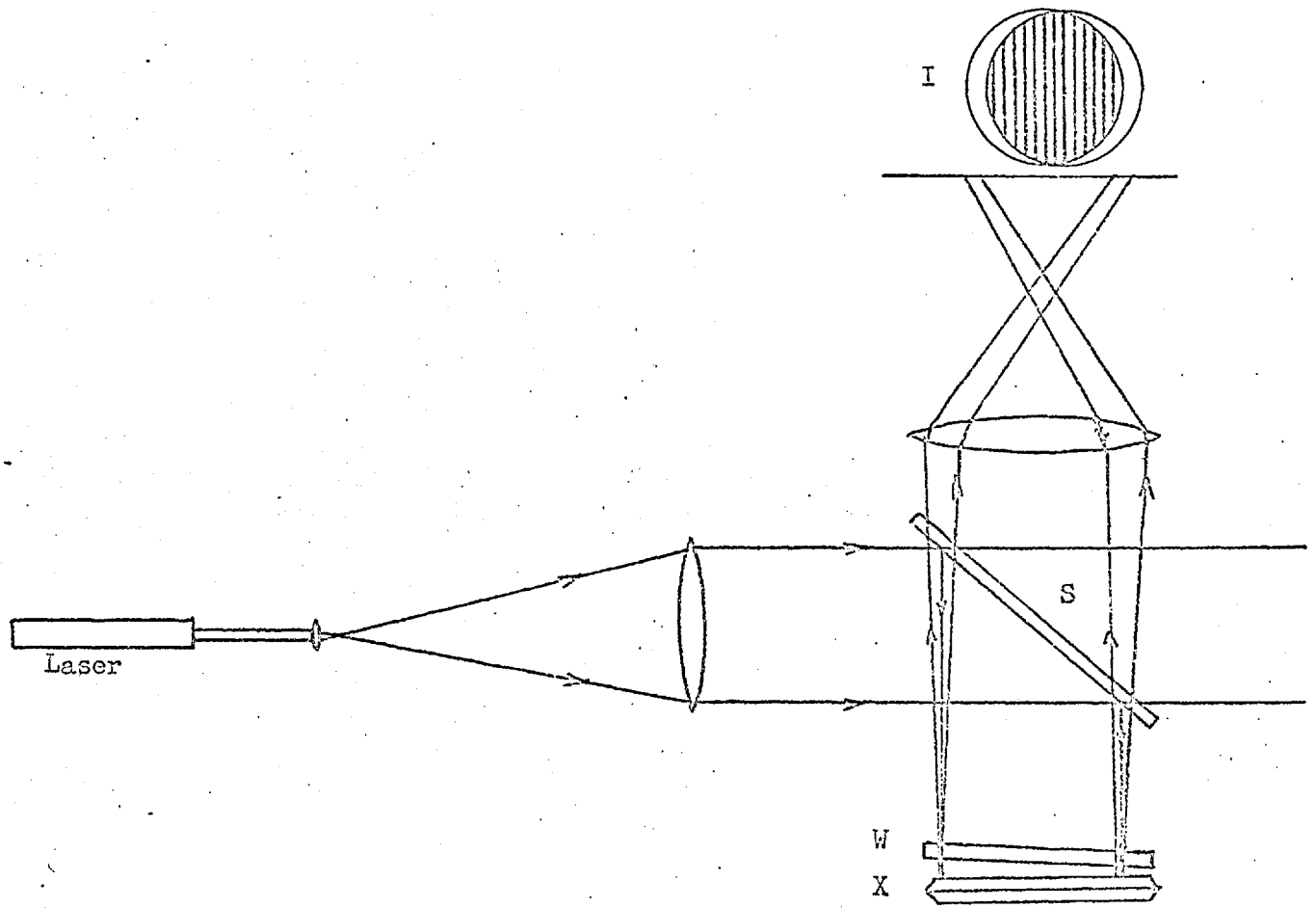

FIGURE 5.4

Optical system for recording the interference fringes shown in Figure 5.5 demonstating uneven amplitude of oscillation over the crystal face.
S, beam splitter; W, glass slab; X, silvered crystal face; I, interference pattern.

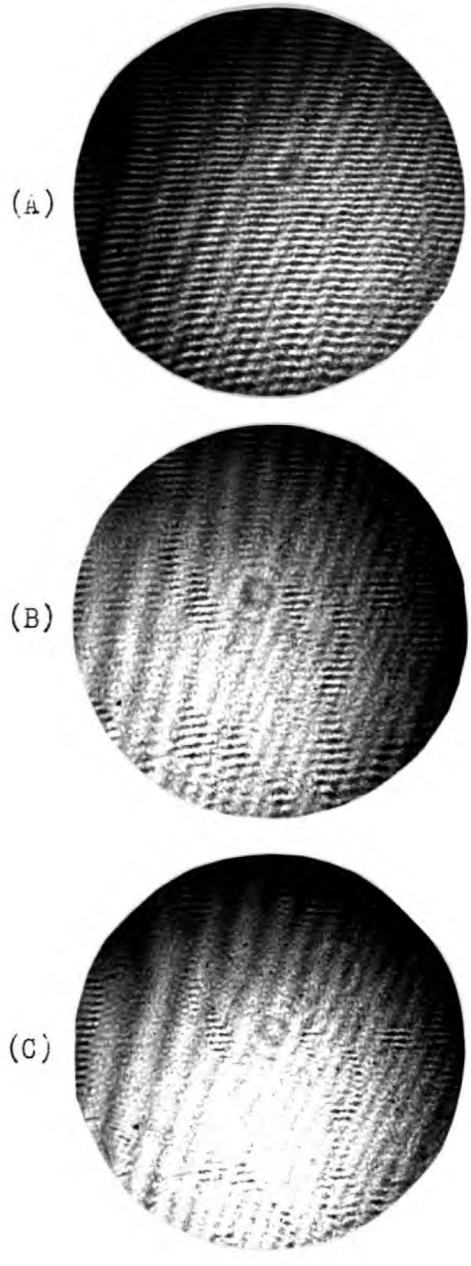

Interference fringes obtained using the optical system in Figure 5.4 (A) crystal off, (B) 60 $mW.cm^{-2}$, and (C) 220 $mW.cm^{-2}$.

FIGURE 5.5

TABLE 6

Relative marking of sound waves at different temperatures.

Method of marking	Degree of marking relative to that at 273°K		
	273°K	1000°K	3000°K
Interferometry	1.0	0.74	0.56
Deflection	1.0	0.14	0.03
Shadowgraphy	1.0	0.20	0.05

Table 7 shows the factor by which the acoustic power density must be multiplied in order to restore the marking obtained at 1000°K and 3000°K to the value at 273°K.

TABLE 7

Power compensation factors

Method of marking	Power compensation factor		
	273°K	1000°K	3000°K
Interferometry	1.0	1.8	3.2
Deflection	1.0	51	1100
Shadowgraphy	1.0	25	400

The clearest record of an acoustic beam in a system in which there is a large temperature range is obtained using the method of visualization that is least sensitive to temperature changes. Table 6 shows that on this basis interferometry should be the best method of marking the sound waves. Equation 5.36a and Table 6 may be used to see whether the degree of marking is in fact sufficiently large to be detected. Assuming that the maximum possible power density that can be obtained from the transducer is 250mW.cm^{-2} and that Z = 3cm N works out to be 0.31λ at 273°K and 0.17λ at 3000°K. Although these quantities are small they should be large enough for

for the detection of the acoustic wavefronts.

The next best method of marking is shadowgraphy. A quantitative assessment of the magnitude of the marking can be made using equation 5.36c only when $\Delta I/I$ is small, i.e. when the deflections are small. However, one can say qualitatively that if the calculated value of $\Delta I/I$ is say greater than 0.1 it should be possible to obtain a photographic record of the shadow of the sound waves. When $P = 250mW.cm^{-2}$, $Z = 3cm$, $l = 20cm$ and $\nu_s = 0.5MHz$, $\Delta I/I = 1.63$ at $273^{\circ}K$ and 0.08 at $3000^{\circ}K$. Shadowgraphy therefore seems a feasible method of visualization up to almost $3000^{\circ}K$. There will, however, be vast differences in the quality of the record in regions corresponding to low and high temperatures.

Deflection methods of marking sound waves are the most dependant on temperature. According to equation 5.36b and Table 6 the maximum angular deflection for $P = 250mW.cm^{-2}$, $Z = 3cm$ and $\nu_s = 0.5MHz$ is $85 \times 10^{-6}Rd$ at $273^{\circ}K$ and $2.5 \times 10^{-6}Rd$ at $3000^{\circ}K$. These deflections are too small to be of much use for marking the sound waves.

If the effects of attenuation are taken into account the degree of marking will be even smaller than that calculated above. However, this may be more than compensated for in the case of shadowgraphy and deflection methods by the fact that on account of their finite amplitude the sound waves are almost certainly not sinusoidal and have steeper refractive index gradients than are predicted by the above equations. (The wavefronts of a sound wave tend to steepen whenever $(d\xi/dt)/v = (2P/\rho v)^{\frac{1}{2}}/v$ is no longer negligible compared

to unity[54c,57]. For P = 250mW.cm^{-2} this ratio is of the order of 0.01).

The application of the ultra-sonic method does not require a knowledge of the absolute acoustic power output from the transducer. Nevertheless an idea of its magnitude would be useful if the exact refractive index distribution within the acoustic field were also known for then precise predictions of the limitations of the method could be made. In practice, however, it has been found that the main requirement is to be able to compare power outputs for then it is possible to use the results of an experimental observation made at a particular power setting and under certain conditions to predict what observations should be possible at different power settings and under different conditions.

An acoustic wattmeter suitable for comparing acoustic power settings and for giving an idea of the absolute acoustic power densities was made and is illustrated in Figure 5.6. The principle of the device is based on an acoustic radiation pressure measurement. If A is the cross-sectional area of the acoustic beam and F is the force the acoustic beam exerts on the vane attached to the torsion wire the acoustic power density is given by[54d,55a,58b]

$$P = \frac{Fv}{A} = \frac{\tau \theta v}{r A} \qquad \ldots 5.38$$

where τ is the torsion constant of the wire, θ the angular deflection and r the distance from the wire to the centre of the vane. The torsion constant was determined from a measurement of

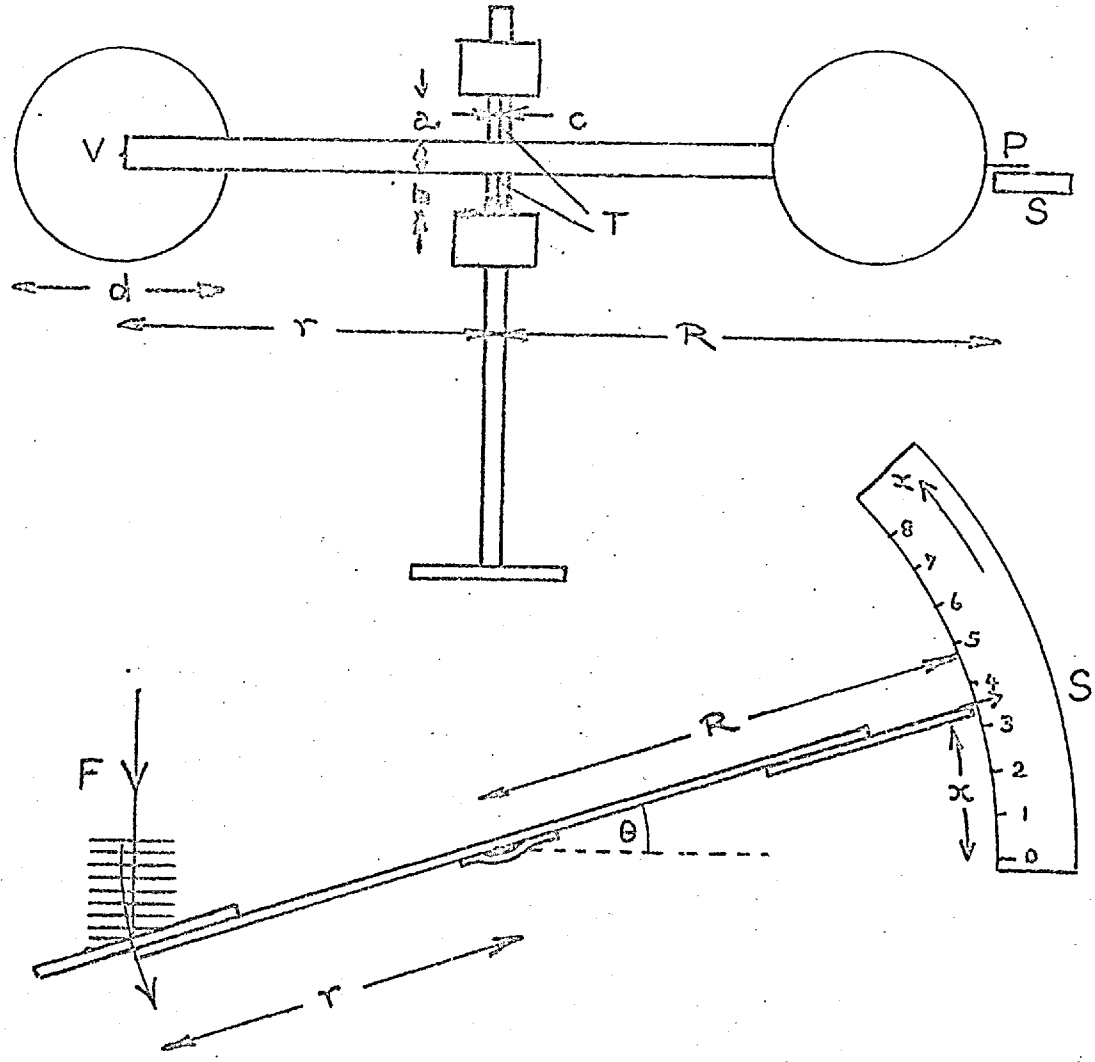

Acoustic torsion wattmeter. V, cardboard vane; T, torsion wire; P, pointer; S, centimeter scale; x, linear deflection; F, force exerted by beam on vane. a = 1.2cm, b = 1.0cm, c = 0.007inch, d = 6.0cm, r = 10.0cm, R = 13.0cm.

FIGURE 5.6

the period of oscillation of a mass of calculable moment of inertia attached to the wire and was found to be equal to $1.26 \times 10^4 \pm 1\%$ dyne.cm.Rd^{-1}. Instead of measuring θ, the linear displacement x of a pointer attached to the vane was measured. Replacing θ by x/R and then substituting $\tau = 1.26 \times 10^4$ dyne.cm.Rd^{-1}, r = 10.0cm, R = 13.0cm, $v = 3.43 \times 10^4$cm.s^{-1} and A = 14.4cm^2 for the 0.5MHz crystal and 15.9cm^2 for the 0.7MHz crystal into equation 5.38 therefore gives for the final expressions used for assessing the acoustic power densities:

$$P = 23.0x \text{ mW.cm}^{-2} \qquad \text{for the 0.5MHz crystal} \qquad \ldots 5.39a$$

$$P = 20.9x \text{ mW.cm}^{-2} \qquad \text{for the 0.7MHz crystal} \qquad \ldots 5.39b$$

where x is measured in cm.

Although this wattmeter may suffer from certain disadvantages as a result of the possible effects of attenuation, streaming and standing waves the last is unlikely to be important at high power levels and Medwin[59] suggests that the first two are probably self compensating. Not only is the wattmeter simple and direct reading but by using the crystal mounting illustrated in Figure 5.2b it can be used to monitor the power radiated from the back face of the crystal at the same time as the waves propagating from the front face are being photographed.

5.5. VISUALIZATION OF SOUND WAVES.

5.5.1. Introduction.

Because of the desirability of simplicity schlieren and shadow methods were considered to be preferable to interferometric methods.

Also, as measured power densities of the order of 200mW.cm^{-2} have been obtained from the transducer previously described the refractive index gradients are certainly much steeper, due to their finite amplitude, than was predicted for sinusoidal waves and so makes these methods of visualization much more favourable than were suggested by the previous calculations.

There are obvious advantages in using a Q-switched ruby laser light source as regards duration, brightness and coherency, and hence in the application of the ultra-sonic method to highly luminous systems. As, at this stage, the problem is essentially one of visualization the initial investigation may be carried out on any non-luminous system and so there is no great need for the extreme brightness of a laser source. The main requirement is a source having a time duration less than ν_s^{-1}. This can be obtained without much difficulty from a suitably designed spark gap. Such a source was eventually chosen as it also had the advantage of avoiding some of the incidental problems caused by the extreme coherency of laser sources.

It is shown how the preliminary visualization of standing sound waves was made using a continuous light source. The limitations of both the schlieren and shadow methods are examined and in particular it is shown how the shadow method of visualization of sound waves in air at room temperature depends on the acoustic power density.

5.5.2. Light source.

Two argon-jet spark light sources were constructed having a similar design to that used at the N.P.L.[23]. Their effective flash duration was found to be sufficiently short to enable both 0.5MHz and 0.7MHz sound waves to be photographed. The first spark gap had an output of 0.125Joule and was built using one TCC low inductance 0.01μF capacitor charged to 5kV. In later work the light output was increased to 1Joule by placing two 0.01μF capacitors in parallel as shown in Figure 5.7a, and overcharging them to 10kV.

The spark gaps could be fired in the conventional way by applying a voltage pulse to a trigger electrode via a trigger transformer. Figure 5.7b shows diagramatically two ways which were used to develop a voltage pulse across the primary of the trigger transformer. Method i) was used for firing the spark gap for all the investigations described in this chapter, while method ii) was used for the investigations described in the following chapter. In method ii) it was possible to fire the spark gap at any pre-arranged time after a particular event occured. The advantage of being able to do this will become apparent later.

Figure 5.8 illustrates how a continuous light source, in the form of a high pressure mercury vapour lamp, was used for aligning the spark gap. An image of the mercury arc was formed at the centre of the spark gap using the condensing lenses L_1 and L_2. Both the spark gap and mercury vapour arc could then be imaged onto the pin-hole, A, using the condensing lenses L_3 and L_4. With this

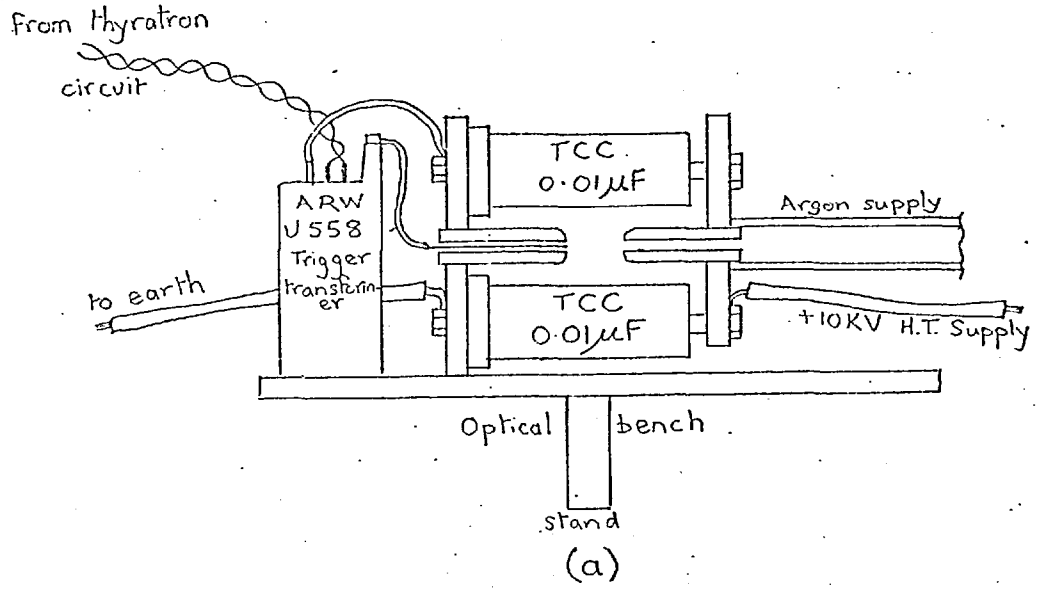

(a)

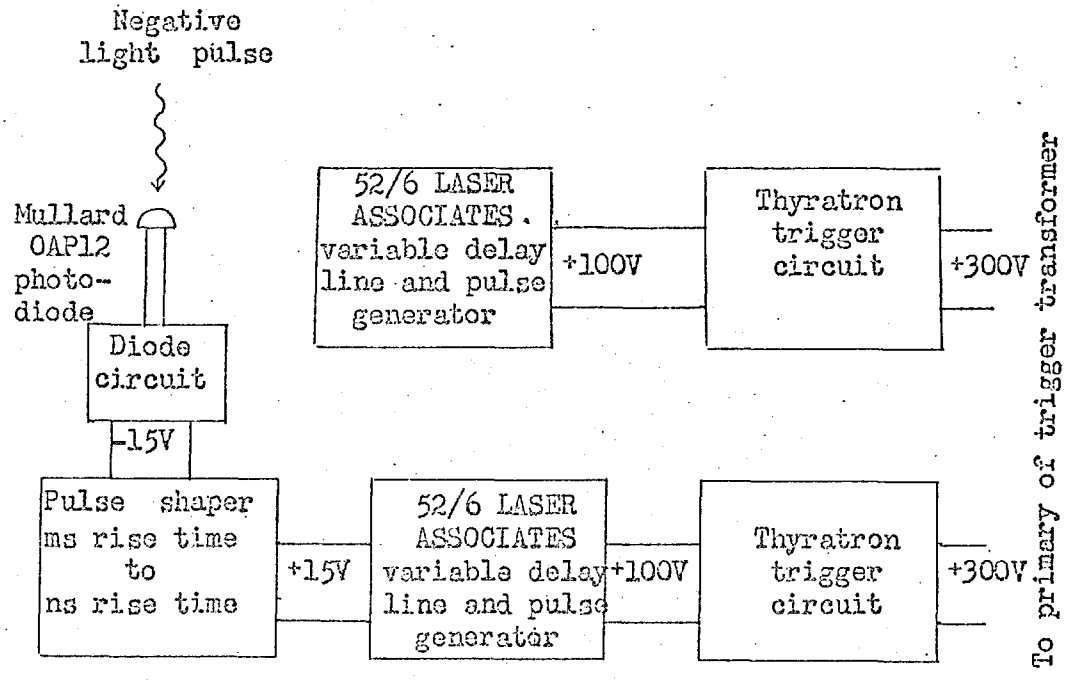

(b)

(a) Design of spark gap and (b) arrangements used for triggering spark gap.

FIGURE 5.7

arrangement it was easy to align the rest of the optical system using the continuous light source only. This light source was also used for the visualization of the standing sound waves.

5.5.3. Preliminary visualization of sound waves in air.

As there is no clear indication in the literature[45,60-64], which has been fully reviewed by Bergmann[52] up to the year 1938, on the minimum power density and depth of acoustic field necessary for the good visualization of progressive sound waves in air it was first necessary to carry out a preliminary investigation into this problem. For convenience this was carried out using in the first place standing sound waves and a continuous light source.

The dark field schlieren system used for the initial visualization is shown in Figure 5.8. The schlieren stop K was sufficiently large to just mask out all the direct light. Standing sound waves could be formed in the approximately 1cm wide gap between the 0.5MHz crystal (operating at a relatively low power) and the reflector plate using the crystal holder illustrated in Figure 5.2a. At this stage no direct method of acoustic power monitoring was used. However, an idea of its magnitude could be assessed from the observation that when a ground glass screen was placed behind the schlieren stop it was just possible to detect two or three reasonably well defined patches of high illumination on either side of K. These were identified as the diffraction orders produced by a grating structure and illustrated the fact that plane standing sound waves constitute a phase grating. Exactly

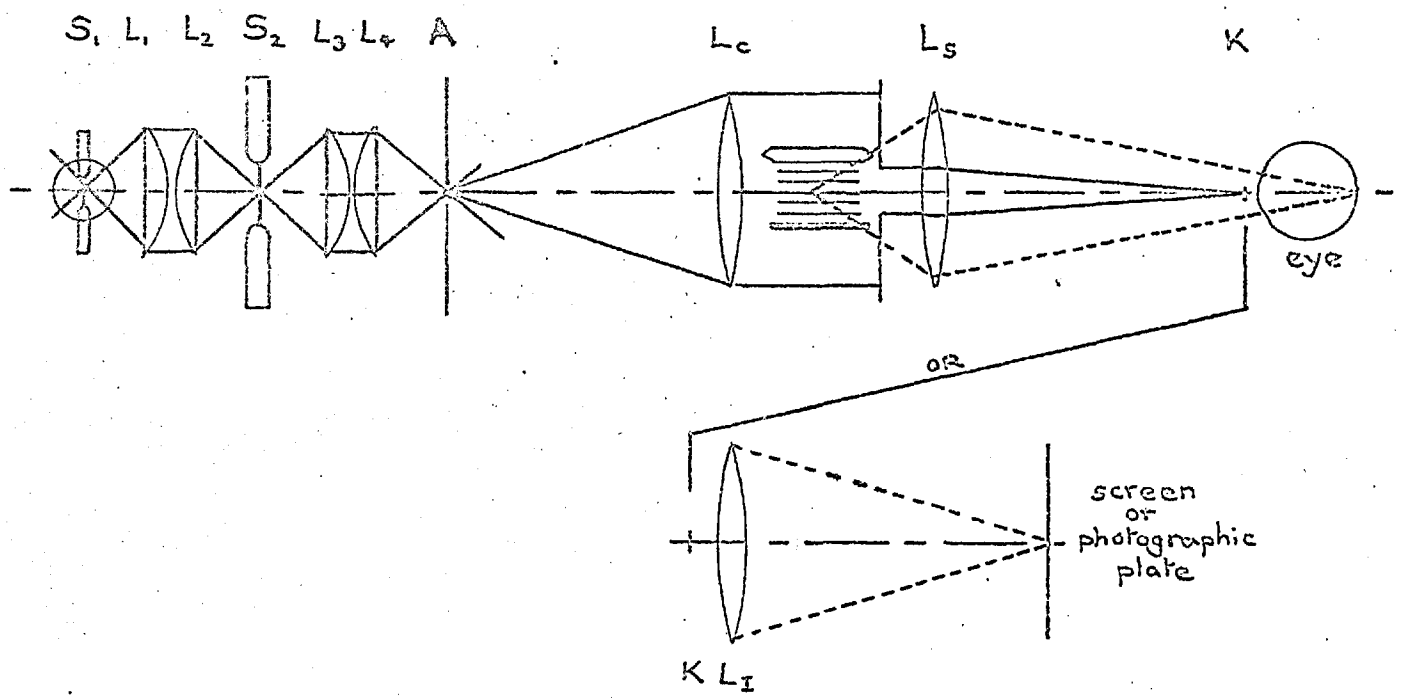

FIGURE 5.8

Schlieren system for visualizing sound waves. S_1, continuous light source; S_2, argon jet spark light source; L_1,L_2,L_3,L_4, condensing system; A, pinhole aperture; L_c, collimator lens; L_s, schlieren lens; K, schlieren stop; L_I, imaging lens.

the same diffraction pattern was observed after repositioning the crystal holder so that the transluminating beam passed only through the progressive sound field.

The presence of the standing and progressive sound waves could most simply be detected by placing ones eye immediately behind the schlieren stop such that at least the $\pm$ 1 diffraction orders passed through the pupil. The sound waves appeared as regions of bright illumination against a dark background. As the eye can detect extremely low levels of illumination this is perhaps the most sensitive unaided method of visualization that exists and it was possible using this method to detect the presence of progressive sound waves up to a distance of 30cm from the crystal face. However, the distribution in the illumination was not completely uniform and had the appearance of two or three diffuse columns of high intensity. This indicated that not all of the crystal's surface was oscillating with equal amplitude and is in agreement with the previous interferometric observations described in 5.4.2.

The diffraction pattern formed by the standing waves is illustrated in Figure 5.9a and was photographed on an Ilford HP3 plate at an exposure time of 10sec. The optical system used was the same as in Figure 5.7 except that K was replaced by a photographic plate. The optical specification of the system is give given in OS1. The 'star' like appearance of each maxima was caused deliberately by placing a triangular aperture in front of the gap containing the standing waves, so as to make the diffraction maxima visible by separating them from the diffraction pattern

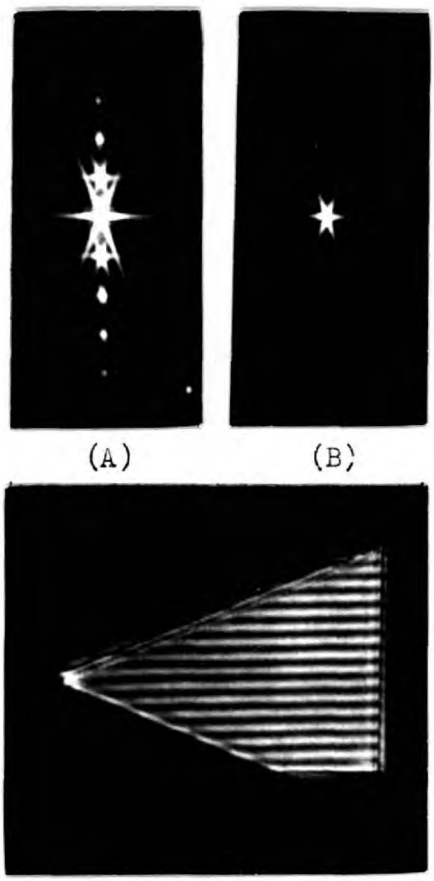

Diffraction patterns produced at the focus of the schlieren lens (A) by standing sound waves (B) by by a triangular aperture. (C) schlieren photograph of standing sound waves.

FIGURE 5.9

produced by the parallel gap. Figure 5.9b shows the diffraction pattern produced by the triangular aperture only (i.e. with the

OS1

S: 25owatt Hg-vapour lamp + green filter
A: 0.1mm diameter.
L_c: 100cm f.l.
L_s: 185cm f.l.
M : 0.87 (magnification using L_i)

tranducer turned off). By using the negative of Figure 5.9b as the schlieren stop K in Figure 5.8 the schlieren record of the standing sound waves illustrated in Figure 5.9c was obtained. This was recorded on an Ilford HP3 plate at an exposure of 60sec.

It was not possible to record progressive sound waves with the above optical system by simply replacing the Hg-vapour lamp by a 0.125Joule spark gap. With the present transducer this could only just be done using Ilford XK (blue sensitive) plates and by modifying the optical specification to that given in OS2 so as to increase the light flux falling on the photographic plate.

OS2

S: 0.125J argon jet spark.
A: 0.37mm diameter.
L_c: 50cm f.l.
L_s: 185cm f.l.
M : 0.36

These observations suggested that the acoustic field was not sufficiently intense for it to diffract an appreciable amount of light around the schlieren stop and so affect the photographic plate. Because of this the transducer's circuit was redesigned so as to

increase its power output by roughly an order of magnitude. It is this modified circuit that is shown in Figure 5.3.

5.5.4. Limitations of the schlieren method.

Increasing the acoustic power density to between 100 and 200mW.cm^{-2} (when several diffraction orders become visible) did not appreciably improve the schlieren record of the progressive sound waves even after replacing the 0.125Joule spark by the 1Joule spark. This was because the exposure levels were probably so low that one was operating on the tail of the photographic plate's (Ilford XK) characteristic curve.

To overcome this problem it was necessary to either increase i) the acoustic power density and depth of acoustic field, ii) the brightness of the spark, iii) the size of the pin hole, or iv) to somehow raise the background level of illumination falling on the plate. As the crystal was probably working at its maximum power output for continuous operation, and as ii) and iii) had also been increased to their maximum values (see OS3) the only way left was to increase the background level of illumination falling on the plate. This was most conveniently done by making the diameter of the schlieren stop slightly smaller than the diameter of the focal spot of the schlieren lens. Figure 5.10 shows three photographs of 0.5MHz progressive sound waves taken on Ilford XK plates using the optical system illustrated in Figure 5.8 and the specification given in OS3 in which the diameter of the schlieren stop $K_{a,b,c}$ was a) slightly greater, b) equal to and c) slightly less than the diameter of the focal spot of the schlieren lens. Although it was not possible to

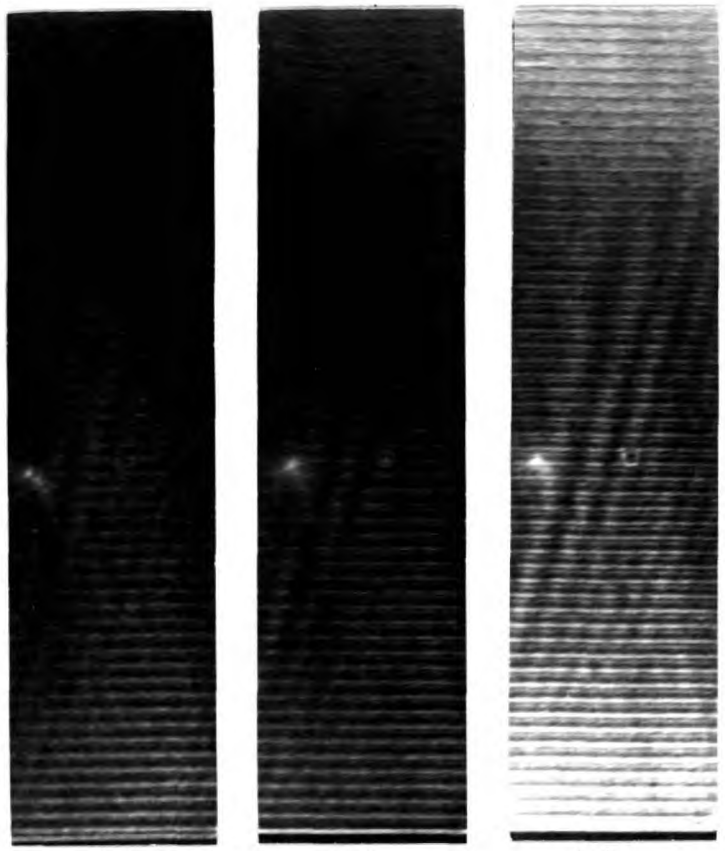

Schlieren photographs of 0.5MHz progressive sound waves for three different schlieren stop diameters - see 0S3. (A) stop diameter 2.3mm (90 $mW.cm^{-2}$), (B) stop diameter 2.0mm (92 $mW.cm^{-2}$), (C) stop diameter 1.6mm (75 $mW.cm^{-2}$).

FIGURE 5.10

OS3

S: 1J argon jet spark.
A: 0.57mm diameter.
L_c: 50cm f.l.
L_s: 180cm f.l.
M: 0.36
K_a: 2.3mm diameter.
K_b: 2.0mm diameter.
K_c: 1.6mm diameter.

maintain the acoustic power densities exactly equal for each of the three photographs it is, nevertheless, quite clear that allowing some undeflected light to fall on the plate greatly extended the amount of marking. K could not be reduced much more than shown as the effects of the background light soon swamp those caused by the diffracted light.

For optimum marking the size of the schlieren stop relative to the size of the focal spot therefore depends, amongst other things, critically on the acoustic power and acoustic beam width (i.e. the amount of light diffracted around K) and so it was concluded that this method of visualization and recording would only be suited for studying systems in which there does not exist appreciable distributions in the properties of the acoustic beam.

5.5.5. The shadow method.

To see how the degree of marking in a shadowgram of sound waves depends on the viewing distance, l, and the acoustic power density the optical system shown in Figure 5.11 was set up. Figure 5.12 illustrates how the shadowgram of both progressive and standing 0.5MHz soundwaves, at an acoustic power density of

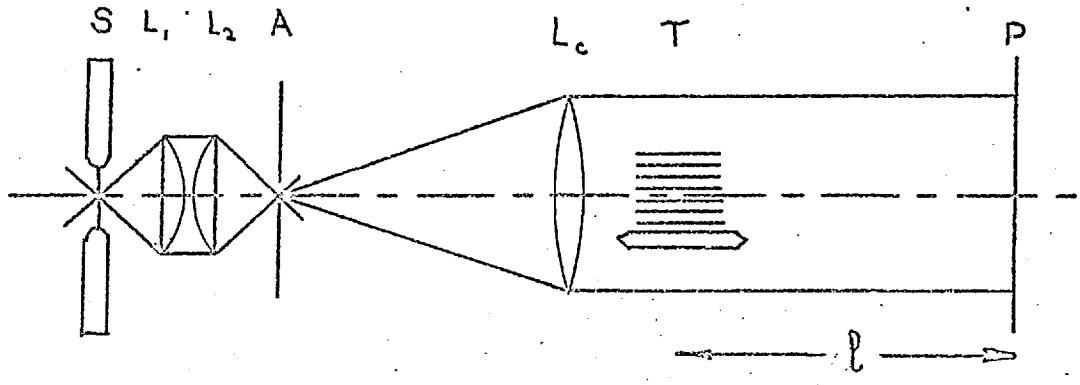

Shadow system for visualizing sound waves. S, argon jet spark light source; L_1,L_2, condensing system; L_c, collimator lens; T, sound waves; l, distance between centre of sound beam and viewing plane; P, photographic plate.

FIGURE 5.11

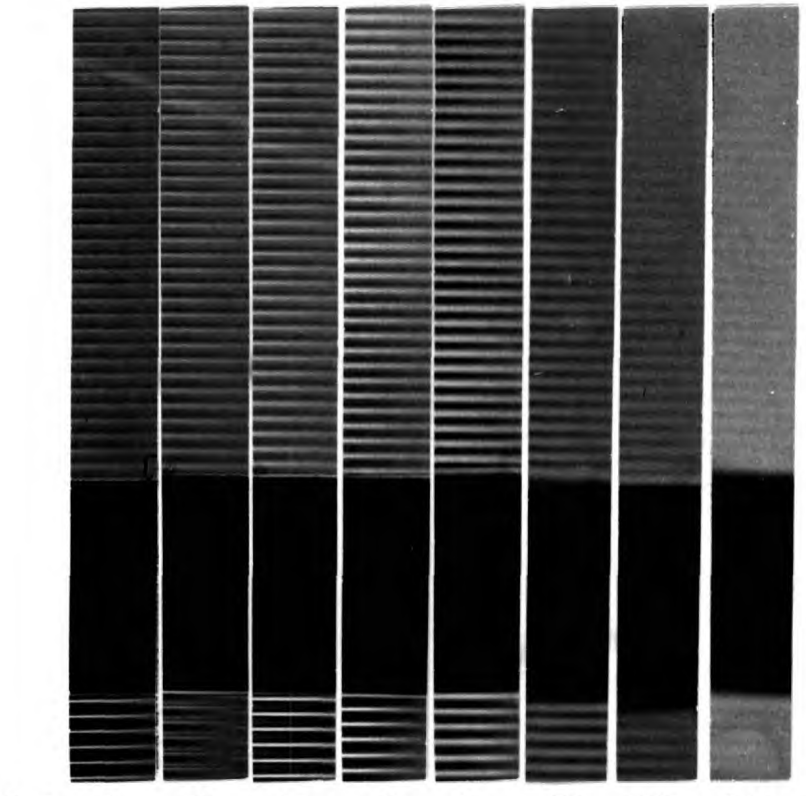

Shadowgrams of progressive (top) and standing (bottom) sound waves at various viewing distances, l. Sound frequency 0.5MHz, power density 100mW.cm^{-2}, and acoustic beam width 4.5cm.

FIGURE 5.12

nomimally 100mW.cm^{-2} and an acoustic beam width of 4.5cm, depends on the viewing distance (measured from the centre of the crystal) from 5cm up to 145cm. Details of the optical system are given in OS4.

OS4

S: 0.125J argon jet spark.
A: 0.3mm diameter.
L_c: 50cm f.l.
l: variable from 5cm to 145cm.
M: 1.0

Examination of the photographs in Figure 5.12 revealsthat for small l very sharp asymmetrical marking of the progressive wavefronts occurs. This indicates that the compression fronts are steeper than the rarefaction fronts and that the waves, therefore, do not have a sinusoidal profile. It is also seen that the visibility of the wavefronts is not particularly critical on the viewing distance and that relatively good marking can be obtained over a range of l covering several centimeters. The best marking occurs in the neighbourhood of l = 20cm. Below this the marking is sharper as the light deflected out of a compression front only partly fills the rarefaction region. At distances greater than 20cm the deflections overfill the rarefaction region and spill into the compression front and as a result introduces a loss in marking contast .

The effect of reducing the acoustic power density was next investigated. Figure 5.13 shows five shadowgrams (photographed on Ilford AK plates) of 0.5MHz sound waves at various acoustic power densities between approximately 3mW.cm^{-2} and 70mW.cm^{-2}. (It was not

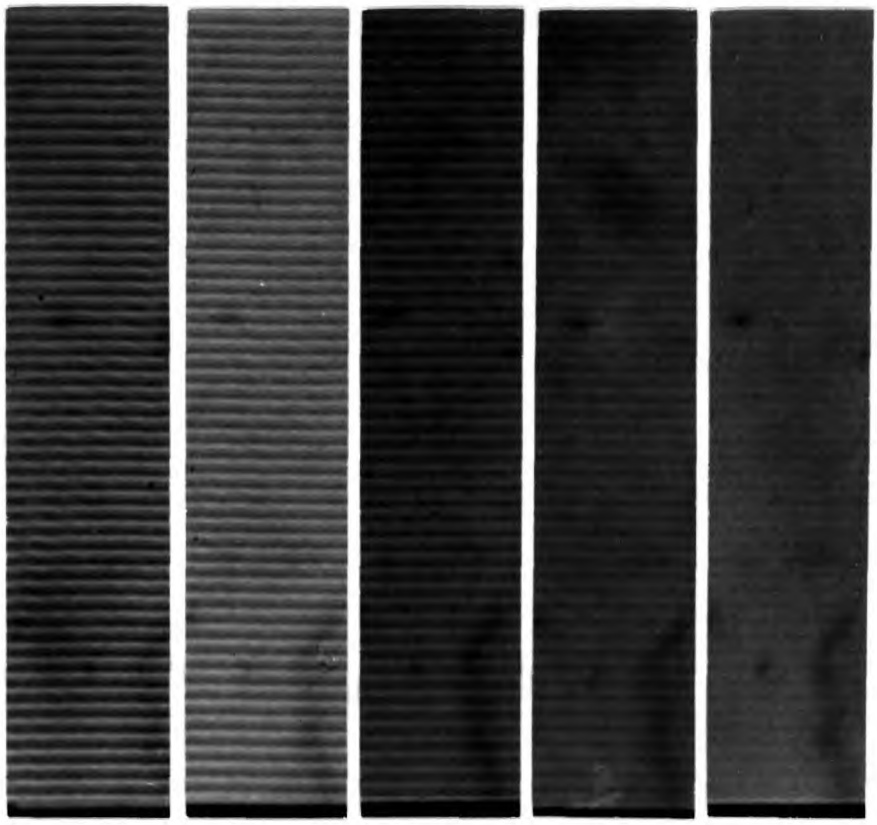

Shadowgrams of progressive sound waves at various acoustic power densities, P. Sound frequency 0.5MHz, viewing distance 20cm, acoustic beam width 3.0cm.

FIGURE 5.13

possible to measure the very low acoustic power densities using the acoustic wattmeter described in section 5.4.3. In these cases the acoustic power levels were estimated by monitoring the amplitude of the oscillator voltage on an oscilloscope. This was then converted into a power density using a calibration curve obtained at higher power levels by extrapolation.) In all cases the acoustic beam width was 3cm and the crystal holder used was the one illustrated in Figure 5.2b. Details of the optical system are given in OS5.

OS5

S: 1J argon jet spark.
A: 0.57mm diameter.
L_c: 50cm f.l.
l: 20cm.
M: 1.0

It is clear from these photographs that the shadow method has an extremely large range of acoustic power detection and is the most suitable method of recording the acoustic wavefronts. It has the added advantage of extreme simplicity.

5.6. SUMMARY.

The essential features governing the propagation of ultrasonic waves in gases have been discussed and expressions relating the velocity of sound to both temperature and gas composition are given.

Acoustic power density measurements suggested that the sound waves radiating from a specially constructed quartz crystal transducer were not purely sinusoidal, and this belief was confirmed

experimentally by an examination of the structure of a shadowgram of the sound waves recorded at small viewing distances. Although this conclusion invalidates the quantitative application of the various equations describing the optical properties of the acoustic field (which were derived assuming a sinusoidal profile) they can probably still be used for predicting the temperature, power and frequency dependences of the various optical methods of visualization.

It was shown theoretically that the least temperature dependant (and hence most desirable) method of recording sound waves is by interferometry. However, because of the desire to develope as simple a diagnostic tool as possible the less complicated methods of schlieren and shadowgraphy were looked into further. An experimental study of these two methods showed that schlieren methods were unsuitable, and that shadowgraphy was the most promising both from the point of view of extreme simplicity and in its ability to record acoustic waves having a very large range of power densities.

Having establised the basis of an ultra-sonic method of gas diagnostics both theoretically and experimentally it may now be applied to practical systems. An analysis of Figure 5.9c gives a value for the velocity of sound of $3.40 \times 10^{4} cm.s^{-1} \pm 3\%$ (averaged over 13 half-wavelengths). This compares well with the accepted value of $3.43 \times 10^{4} cm.s^{-1}$. In the next chapter it is shown how the ultra-sonic method may be extended to the diagnosis of gases in which temperature and composition gradients exist.

CHAPTER 6

ULTRA-SONIC MEASUREMENTS

6.1. INTRODUCTION.

Having established the basis for a combined ultra-sonic and optical method of gas diagnostics it is now shown how it may be applied to flame systems. In extending the method to practical systems it soon became apparent that even at relatively low acoustic power densities the ultra-sonic beam interacted with the gas flows being studied. In particular the disturbing effects resulting from the interaction of an ultra-sonic beam with a premixed methane-air flame has been examined and a method of overcoming it is described.

The velocity of sound is a function of both temperature and composition and so the ultra-sonic method of gas diagnostics has always to be used in conjunction with some other information concerning the nature of the system being studied. This may take the form of either additional experimental data, e.g. the distribution of refractive index, or theoretical predictions, e.g. equilibrium composition. The number of additional bits of information required will depend on how many unknowns there are. To simplify this problem the ultra-sonic method has been tested here only on simple systems in which equilibrium exists and compositions are easily calculable.

Apart from attempting to measure flame temperatures ultra-sonic temperature measurements have been compared with thermocouple

measurements in air and in argon. The temperature of the air used in these measurements was below 1500°K and so changes in atomicity due to dissociation were insignificant[65]. Should dissociation have been important it would have been necessary to make use of the various sources[65,66] of thermodynamic data available. However the temperature dependence of C_p/C_v was significant and had to be taken into account when interpreting a velocity of sound measurement. Neither of these problems existed in the case of argon.

It appears that although the measurement error for the ultrasonic method is greater than that for a thermocouple measurement, the interpretation of the results in terms of a gas temperature are easier and less liable to error as a result of the uncertainties and inaccuracies in making thermocouple corrections to compensate for the disequilibrium that always exists between the gas phase and solid thermocouple junction. This disequilibrium does not exist for sound waves - at least as far as translational and rotational temperatures are concerned.

6.2. THE INTERACTION PROBLEM.

6.2.1. Introduction.

The disturbing effects that sound waves produce on flames and jets under certain circumstances have been observed for many years, and Wood[54e] has reviewed numerous cases dating back to Leconte's discovery of this phenomenon in 1858. Figure 6.1 illustrates the interaction produced when a 0.5MHz ultra-sonic beam, of a few tens

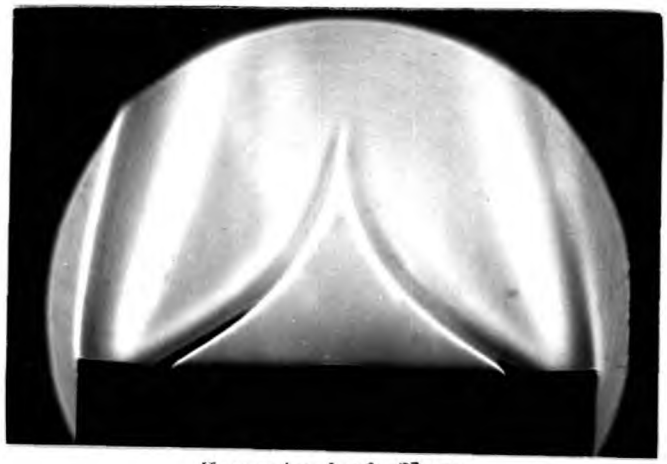

Unperturbed flame

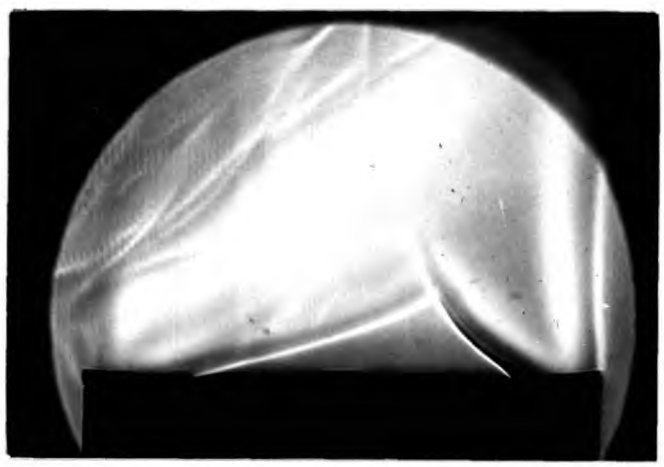

Perturbed flame

Interaction between an ultra-sonic beam and a flame.
Sound frequency 0.5MHz, power density $\sim$10mW.cm^{-2}.

FIGURE 6.1

of mW.cm^{-2}, was directed towards the flat face of a roof shaped reaction zone of a premixed coal gas-air flame stabilized on a rectangular burner. It is clear that the boundary between the burnt gases and the surrounding air is greatly perturbed and that the reaction zone closest to the incoming beam is displaced. However, it is not certain whether or not these disturbances are also accompanied by a complete inability of the sound waves to actually penetrate the hot gases.

To study this problem further a very large square matrix burner, 8cm x 8cm, was made up as illustrated in Figure 6.2a. To provide a flat boundary between the combustion products and the surroundings the burner was designed so that it was possible to sheath the hot gases with an independently controllable air flow, roughly 1cm thick. A premixed methane-air flame, in which the methane flow was 2.5 litre.min^{-1} and the air flow was 33 litre.min^{-1} was used throughout the investigation. A reasonably flat interface between the hot gases and the surrounding sheath was obtained for a sheath flow of 40 litre.min^{-1}.

To prevent the crystal and its mounting from over heating they were placed behind a screen, as shown in Figure 6.2b. Each time a photograph of an interaction was taken a slide, covering a window immediately in front of the crystal, was momentarily removed.

6.2.2. Interaction's dependence on acoustic power density.

The series of schlieren photographs shown in Figure 6.3 was taken, using the optical system illustrated in Figure 5.8 and

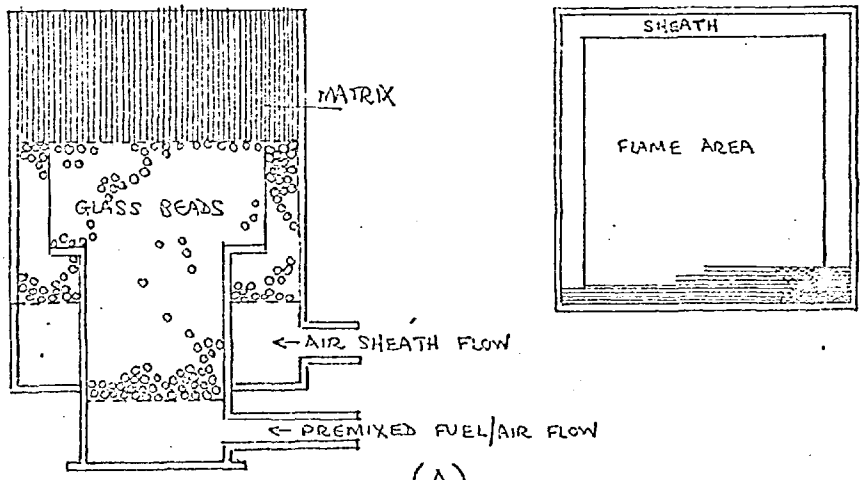

(A)

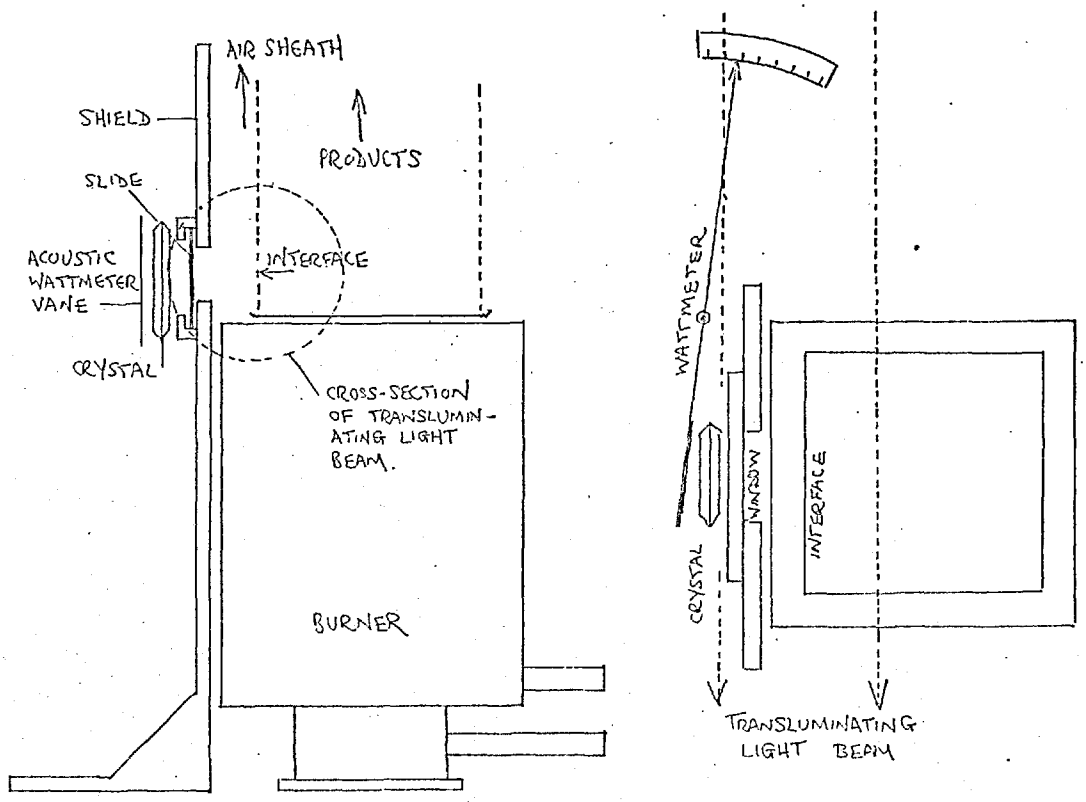

(B)

Design of burner (A) and screen (B) used for studying the interaction between an ultra-sonic beam and air sheath/flame interface.

FIGURE 6.2

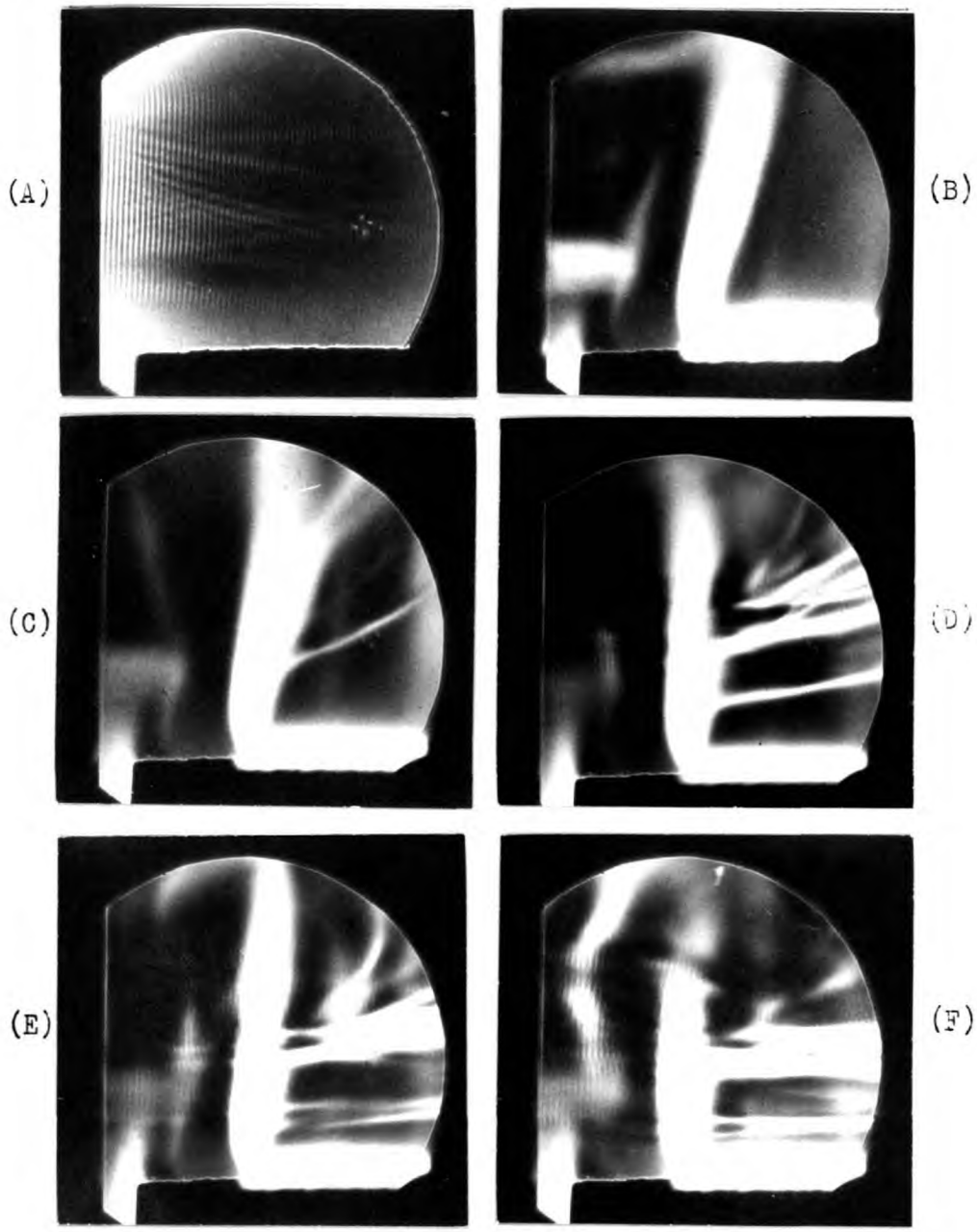

Interaction of an ultra-sonic beam, at various acoustic power densities, with a flame. Sound frequency 0.5MHz, acoustic beam width 3.0cm. (A) no flame, (B) no sound waves, (C) 23 $mW.cm^{-2}$, (D) 54 $mW.cm^{-2}$, (E) 90 $mW.cm^{-2}$ and (F) 114 $mW.cm^{-2}$.

FIGURE 6.3

specified in OS6, to see how the interaction of 0.5MHz sound waves with the flame varied with acoustic power density. For the

OS6

S: 1J argon jet spark.
A: 0.57 mm diameter.
L_c: 50cm f.l.
L_s: 180cm f.l.
K: 2mm diameter.
M: 0.25.

purposes of comparison photographs of the sound waves in air at room temperature and of the unperturbed flame are shown in Figures 6.3a and 6.3b respectively. The dimensions of the acoustic beam used for this and all subsequent studies was 3cm wide x 2.5cm high and was defined by the size of the window in the screen placed immediately in front of the crystal. When taking the photographs in Figure 3 the lower edge of the sound beam was 0.5cm above the top of the burner and the crystal (not shown) was about 2cm to the left of the interface being studied.

Examination of these photographs shows that when acoustic power densities are greater than 50mW.cm^{-2} sound waves are visible in the perturbed region above the flame. However, the wavelength of these sound waves is not appreciably different from those in Figure 6.3a and suggests that the gas in this perturbed region is quite probably air at essentially room temperature. Also, it is seen that as the acoustic power density increases so the interface becomes deflected through progressively larger angles. It was concluded that the interaction between the acoustic beam and the flame arises as a result of entrainment of cold air from the

surroundings at a velocity dependent on the acoustic power density.

Subsequent observations showed that entrainment can occur even at room temperature and that at high powers an appreciable wind may develop in front of the transducer. This can most easily be visualized in the rapid stream like motion of air borne dust or smoke particles in the vicinity of the crystal face. This so called 'quartz wind effect' has in fact been observed[67] before, and occurs as a result of a non-linear process due to the finite amplitude of the sound waves.

6.3. SOLUTION OF INTERACTION PROBLEM.

6.3.1. Introduction.

It was quite apparent from simple dust entrainment experiments that the entrainment velocity was very much less than the velocity of sound. Therefore it must take a relatively long time, in comparison with the transit time of the wavefronts, for the entrained gas to travel a given distance. By photographing the sound waves almost immediately after the crystal starts oscillating it should be possible to obtain a record of the sound waves in the hot gas before it has been appreciably disturbed. A method was devised for rapidly photographing the sound waves in the flame at a preset time interval after the slide shielding the crystal from the flame was removed. The basis of the method was to arrange for the slide on being removed to interrupt a light beam, and then with the aid of a photodiode and suitable circuitry cause the argon jet spark to be triggered.

6.3.2. Design of 'slide-trigger' device.

To get some idea of the time intervals involved a preliminary experiment was performed to find out how the entrainment velocity varied with distance from the crystal face and on the acoustic power density.

The entrainment velocity for air at room temperature, along the normal to the centre of a 0.5MHz quartz crystal, was measured using a particle tracking technique[68] by stroboscopically illuminating entrained bentonite particles at a frequency of 10^3Hz. A chopped 0.5cm wide unexpanded 8mW helium-neon laser beam was used as a source of illumination. The tracks were photographed at right angles to this beam at a magnification of 0.5 on Ilford HP3 plates using a Kodak Specialist Camera. The analysis of a number of tracks recorded for different acoustic power densities showed that the axial entrainment velocity v_e, the distance x from the crystal face, and the acoustic power density P may be related by the empirical expression

$$v_e = 0.44\, P\, x, \qquad (0 < x \lesssim 5\text{cm}) \qquad \ldots 6.1$$

where v_e is expressed in cm.s^{-1} when P is in mW.cm^{-2} and x is in cm.

It follows that if the gas is displaced a distance d with a velocity v_e given by the above expression the time interval t in which this displacement occurs is given by

$$t = 2.3 \frac{d}{P\, x} \qquad \ldots 6.2$$

For $P = 100\text{mW.cm}^{-2}$ and taking 0.5cm as an acceptable value for the perturbation distance d (i.e. the permitted displacement of the

interface between the sheath and the flame) this last equation indicates that the sound waves must be photographed within a time interval of less than 6ms from the instant the slide covering the window in front of the oscillating transducer is removed. From a practical point of view this means that the slide must be removed in a time interval less than this.

Figure 6.4 illustrates the design of the device used for rapidly removing the slide from in front of the crystal, and for triggering the argon jet spark. When the sprung steel lever was released it made contact with a light brass pin which in turn pushed a thin aluminium slide (6cm x 3cm and weighing 2.3gm) along the two guide rails. At the instant the slide began opening the window it also shut a small aperture through which a beam of light passed onto a Mullard OAP 12 photodiode. The signal developed in the photodiode circuit was used to trigger the argon jet spark using the arrangement shown in Figure 5.7b. The opening time of the window was equal to 5ms and was reproducible to $\pm$ 10%. The time between the instant the light beam was interrupted (i.e. the window started to open) and the moment the spark gap fired could be varied from 0.1ms up to 100ms using a Laser Associates 52/6 Delay line.

6.3.3. Testing 'slide-trigger' device.

Figure 6.5 shows a sequence of photographs, for a range of delay times from 5ms to infinity, of 0.7MHz 150mW.cm^{-2} sound waves incident on the interface between the gaseous products of a methane-air flame and the surrounding air sheath. The photographs were

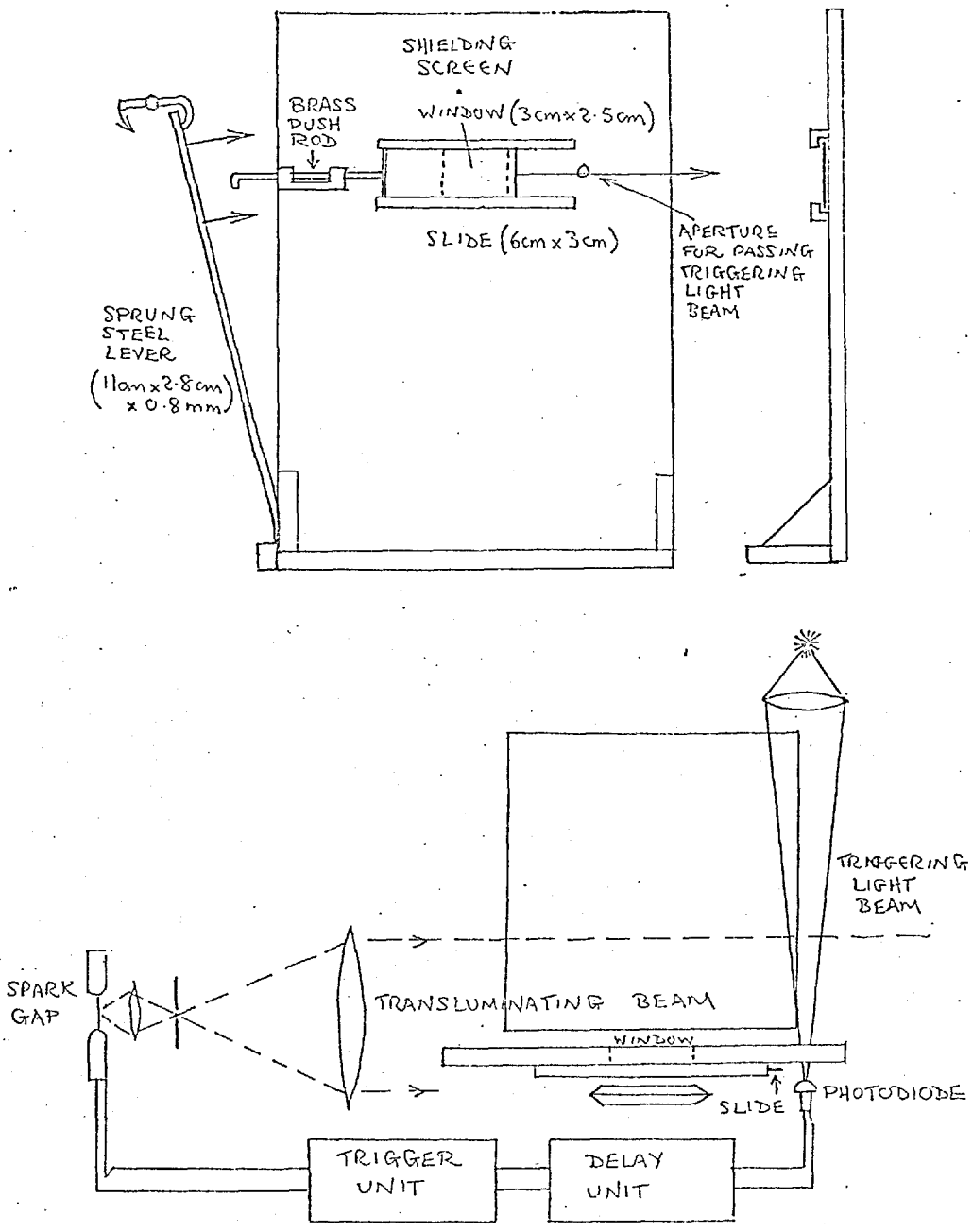

Method used for removing slide covering window in front of crystal and for triggering argon jet spark light source.

FIGURE 6.4

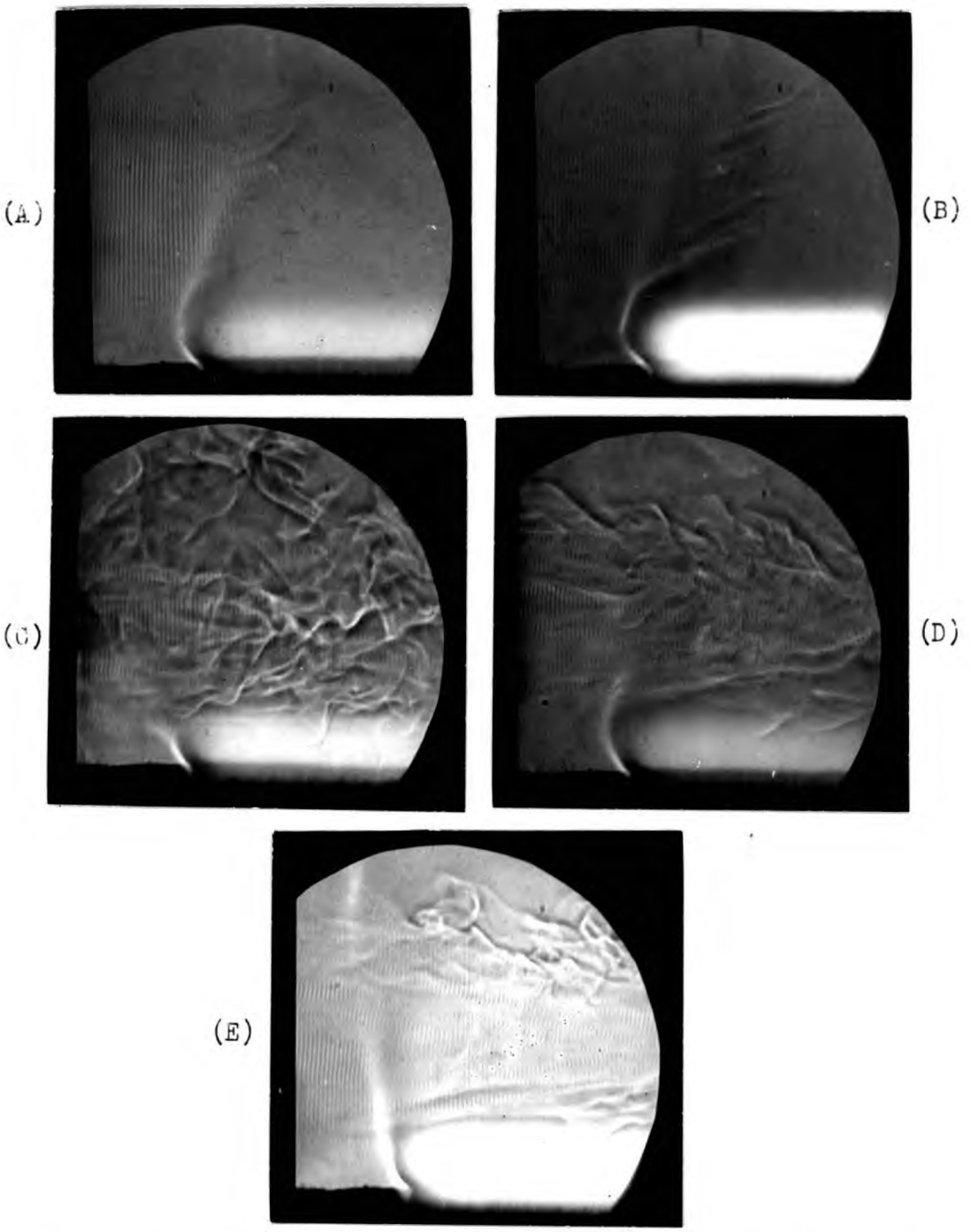

Time sequence of build up of interaction between an ultra-sonic beam and a flame. Sound frequency 0.5MHz, acoustic beam width 3.0cm. (A) 5ms, (B) 10ms, (c) 50ms, (D) 100ms, (E) infinity.

FIGURE 6.5

taken on Ilford XK plates using the optical system illustrated in Figure 6.6 and the specification given in OS7. This system was used

OS7

S: 1J argon jet spark.

A: 0.28mm x 1.10mm (set perpendicular to axis of spark)

L_c: 50cm f.l.

l: effective viewing distance 20cm.

M: 1.0

in preference to the one shown in Figure 5.11 as the lens imaging the 'l-plane' onto the photographic plate reduces the flux of light radiated by the flame from falling on the plate and so reduces the amount of fogging.

Examination of this sequence of photographs confirms that the entrainment of could air causes the perturbation of the flame, and that it takes a finite time to fully develop after the initial switching on of the ultra-sonic beam. Figure 6.5a shows that the perturbation after a time delay of 5ms is as anticipated only very small, while Figure 6.5e shows that after 100ms it is practically fully developed.

6.3.4. Discussion of results.

A measurement of the wavelength of sound within the boundary layer shown in Figure 6.5a reveals that it has a maximum value equal to 1.7 ± 0.1 times the wavelength in the surrounding sheath of cold air. If it is assumed that the acoustic properties of these gases (of which 75% is N_2 and 4% O_2) are essentially the same as for air this may be interpreted as indicating a temperature of $850 \pm 100^{\circ}K$.

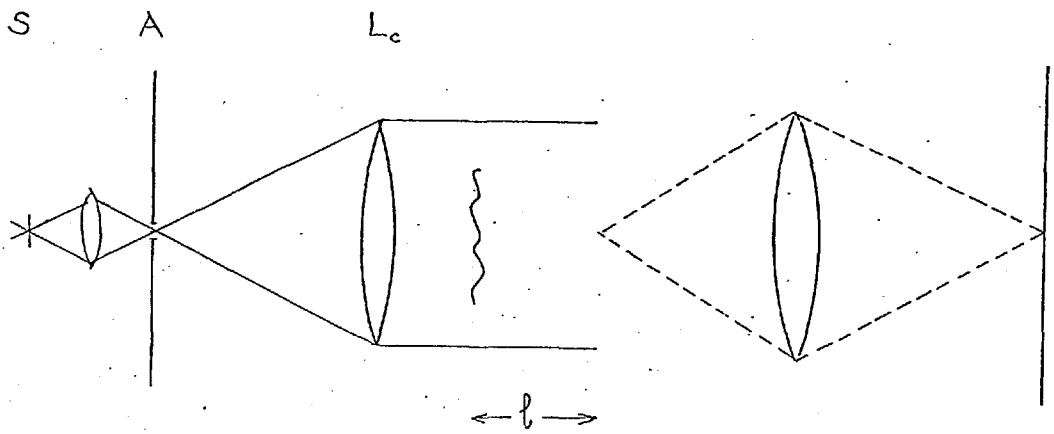

Optical system for imaging viewing plane onto photographic plate. S, light source; A, pin-hole aperture; l, distance between centre of acoustic beam and viewing plane.

FIGURE 6.6

Beyond this point the marking of the sound waves is so weak that measurements are impossible.

The reason for this fall off in marking within the column of flame gases could arise from a reduction in gas density, a perturbation of the acoustic wavefront, an increase in the value of the attenuation coefficient and from the presence of dispersion effects.

The effect of a reduction in gas density due to a rise in temperature has been given in chapter 5 and a curve showing the temperature dependence of sound wave marking using shadowgraphy is shown in Figure 5.1. According to the photographs in Figure 5.13 it should be possible to detect a 3cm wide beam of 0.5MHz sound waves down to an acoustic power density of $3mW.cm^{-2}$. When 0.7MHz waves are used equation 5.36c predicts that this limit is reduced by a factor $(0.7/0.5)^2$; i.e. the lowest limit of detection of 0.7MHz waves should be $1.5mW.cm^{-2}$. The power density used in Figure 6.5a was $150mW.cm^{-2}$. Therefore, as marking is proportional to $P^{\frac{1}{2}}$ it should be possible to detect sound waves up to temperatures where the marking is equal to $(1.5/150)^{\frac{1}{2}} = 0.1$ of its initial value. The curve in Figure 5.1 shows that for air this occurs at a temperature of $6x273^{\circ}K$, i.e. $1428^{\circ}K$. It is not possible, therefore, to explain the lack of marking above $850^{\circ}K$ on the grounds of the reduced gas density.

Shadowgrams of the flame/air sheath interface taken at zero, 1ms, 3ms and 5ms delay show that even at 3ms some perturbation of the interface occurs. Because of the method employed for switching

on the ultra-sonic beam this initial perturbation takes the form of a slightly skewed indentation of the interface. As a result of this the angle that the incident acoustic beam makes with the normal to the interface is no longer zero but is spread over a range of angles. For an acoustic power density of 150mW.cm^{-2} and a window opening time of 5ms the maximum value of the skew angle is of the order of $\tan^{-1}0.2$, i.e. about 12°. For a final flame temperature[69] of 1875°K this will produce an angle of deviation in the incident acoustic beam of roughly 20°. This is more than sufficient to account for the lack of marking at the higher temperatures. However, not all parts of the acoustic beam are deflected through this angle. Instead the perturbed interface probably has a focusing effect and the penetrating acoustic wavefront becomes curved rather than deflected in a single direction. The curve in Figure 5.1 shows that the theoretical marking at 850°K is 0.25 of that observed at 273°K. This may be reduced to 0.1 simply by reducing the acoustic beam width from 3cm to 1.2cm. Therefore, a perturbation to the acoustic wavefront could account for the lack of marking above 850°K.

The increase in attenuation of the acoustic beam as a result of the increase in the viscous and conduction attenuation coefficients with temperature is too small to be of any significance - see Table 4 (page 107) and Table 5 (page 113). However, attenuation of the acoustic beam in the flame gases as a result of dispersion effects is possible. The presence of carbon dioxide, which has a relaxation frequency at atmospheric pressure of 0.7MHz at 900°K, may well result in strong absorption even at the concentrations (i.e.

7% by volume) that exists in the flame gases[70]. Appendix 1 shows how the relaxation frequency of CO_2 varies with temperature. An exact prediction of the dispersion attenuation coefficient is not possible without a knowledge of the vibrational relaxation times of the constituents of the gas mixture as a function of temperature.

6.4. TEMPERATURE MEASUREMENTS IN NON-ABSORBING GASES.

6.4.1. Introduction.

To eliminate the undesirable consequences of dispersion attenuation (possibly due to the presence of CO_2 and even H_2O in flame gases) the ultra-sonic method was applied to non-absorbing gases. This should then show whether perturbations to the acoustic wavefront do contribute appreciably to the loss of marking by the sound waves. The gases used for this test were air and argon, and it was demonstrated that the ultra-sonic method can in fact be used to measure the temperature of these gases.

6.4.2. Electrical gas heater and thermocouple design.

The electrical heater used for heating the gas flow is illustrated in Figure 6.7. The outlet port measured 5cm x 5cm. For a given gas flow and heater settings thermocouple measurements showed that the outlet gas temperature was constant to $\pm$ 10°C over a region extending up to 1cm from its centre in a plane perpendicular to the flow, and up to 5cm above the outlet.

Gas flow temperatures were monitored using a 36 swg calibrated copper-constantan thermocouple stretched horizontally across the flow. The ends of the thermocouple wires, which were 2.5cm long, were

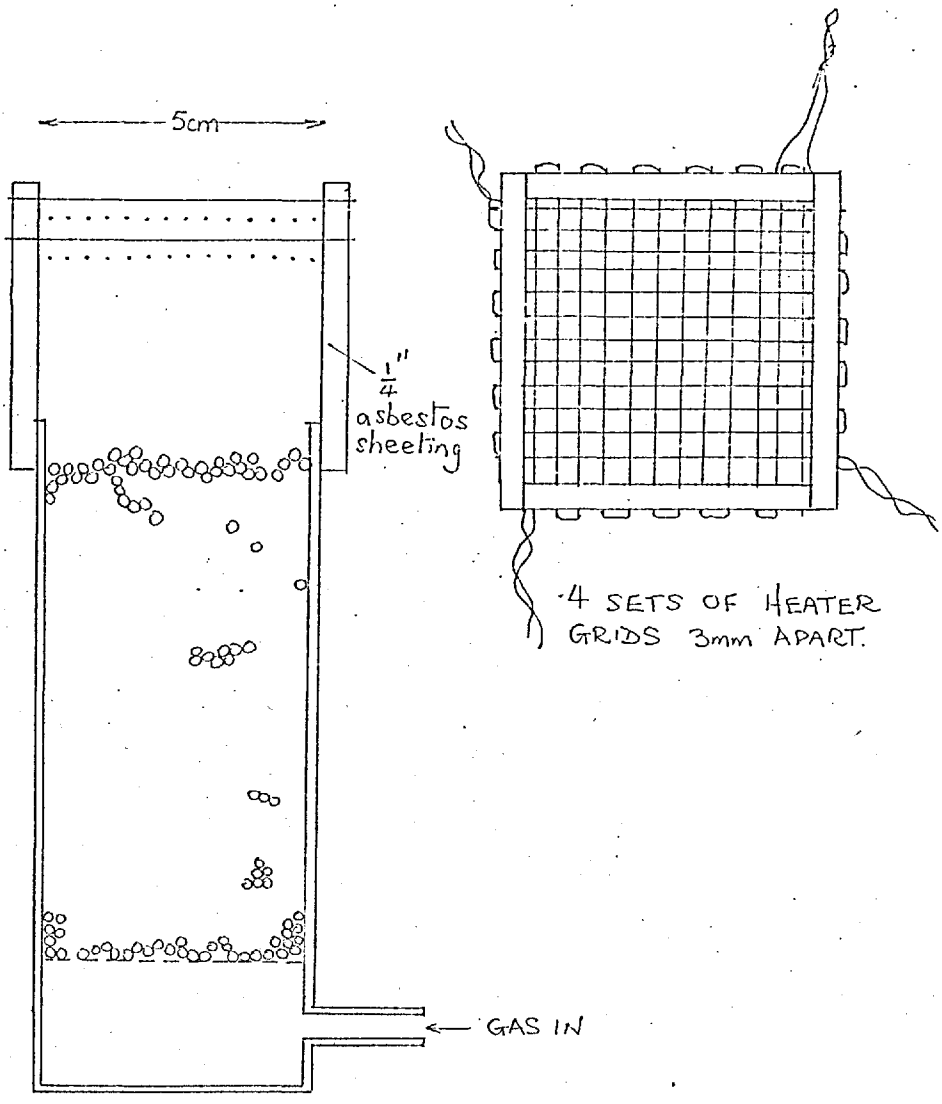

Electric gas heater.

FIGURE 6.7

rigidly held in two relatively massive copper clamps which helped to keep the ends of the wires at effectively room temperature.

6.4.3. Ultra-sonic and thermocouple temperature measurements.

Three ultra-sonic temperature measurements were made for each gas corresponding to thermocouple readings of ~20°C (room temperature), ~400°C and ~500°C. The flow velocity was adjusted for each gas so that the above temperature readings were obtained for heater currents of zero, 0.9Amp and 11.0Amp respectively. For air the voloumatric flow was kept practically constant at 20litre.min^{-1} while for argon it was 30litre.min^{-1} for all three heater current settings.

Shadowgrams of 0.7MHz 125mW.cm^{-2} sound waves at room temperature and at thermocouple readings of ~400°C and ~500°C are shown in Figure 5.8 for air and in Figure 5.9 for argon. These photographs were taken after a delay of 5ms using the optical system illustrated in Figure 6.6 and OS7.

Measurements made on these shadowgrams are summarized in Table 8. The errors in the wavelength measurements were based on the assumption that the wavefronts could not be located to better than $0.1\lambda_c$. Column (4) was calculated by multiplying the measured wavelength in cm obtained from column (3) by the transducer frequency 0.7×10^6Hz. Column (5) was then evaluated using tables[65] of the velocity of sound as a function of temperature. Thermocouple readings taken at about the same time as the shadowgrams were recorded are listed in column (6).

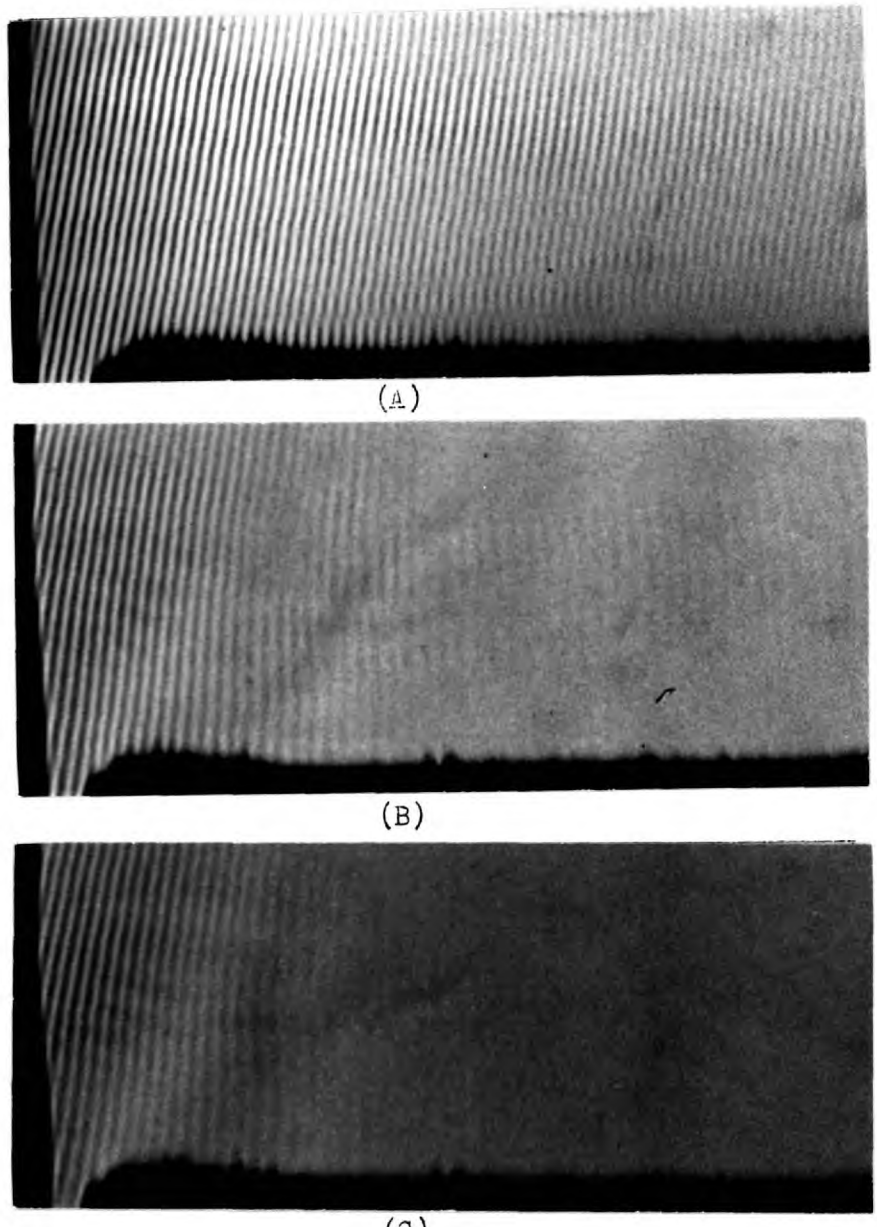

0.7MHz ultra-sonic waves in air. (A) at room temperature (B) thermocouple temperature of 400°C (C) thermocouple temperature of 500°C. Power density 125 mW.cm^{-2}, and acoustic beam width 3.0cm.

FIGURE 6.8

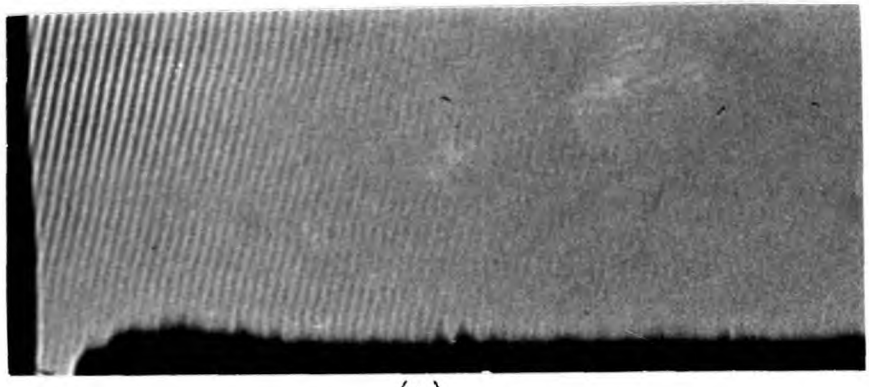

(A)

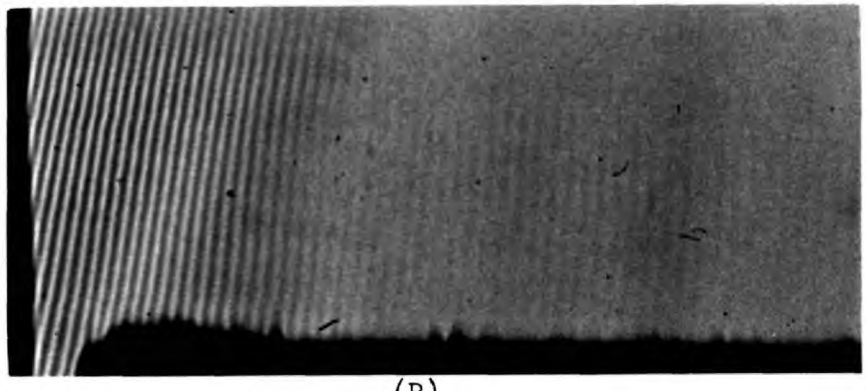

(B)

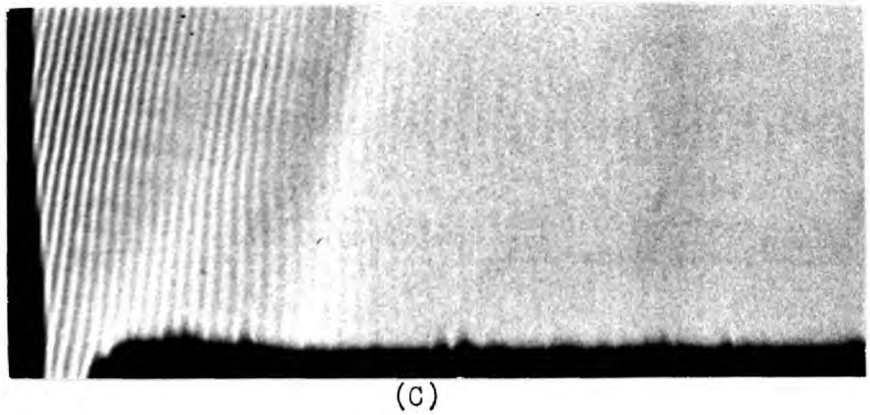

(C)

0.7MHz ultra-sonic waves in argon. (A) at room temperature (B) thermocouple temperature of 400°C (C) thermocouple temperature of 500°C. Power density 125 $mW.cm^{-2}$, and acoustic beam width 3.0cm.

FIGURE 6.9

TABLE 8

Results of simultaneous ultra-sonic and thermocouple temperature measurements

Gas (1)	No. of λ_s measured (2)	Wavelength mm (3)	Velocity of sound $cm.s^{-1}$. (4)	Ultrasonic temperature ^oK. (5)	Thermocouple temperature ^oK. (6)
air	50	$0.495 \pm 0.4\%$	3.46×10^4	296 ± 3	295 ± 1
air	21	$0.784 \pm 1.0\%$	5.48×10^4	770 ± 15	683 ± 10
air	3	$0.827 \pm 7.0\%$	5.79×10^4	863 ± 121	773 ± 10
argon	20	$0.468 \pm 1.0\%$	3.27×10^4	304 ± 6	296 ± 1
argon	19	$0.735 \pm 1.0\%$	5.15×10^4	765 ± 16	670 ± 10
argon	13	$0.800 \pm 1.5\%$	5.60×10^4	904 ± 27	778 ± 10

Inspection of Table 8 reveals that in all cases the ultra-sonic temperature measurement is higher than the thermocouple temperature reading. Also for any given thermocouple temperature setting the ultra-sonic temperature measurements are always higher in argon than in air.

The ultra-sonic temperature values give a more reliable indication of the true gas temperature than the thermocouple temperature readings. This is because the final temperature of a thermocouple junction depends on the heat transfer to and from the wire rather than solely on the temperature of the gas in which it is immersed. Nevertheless it is possible, in principle, to correct a thermocouple temperature reading to the true gas temperature by setting up the heat transfer equation for the wire immersed in the system being studied, and then solving for T_{gas} in terms of the various heat transfer coefficients and other physical constants of the system. Because of the complexities of such a correction

procedure it is usually necessary to assume that many of the parameters describing the system are spatially independent of temperature. It follows then that an only approximate correction can be made. The great beauty of the ultra-sonic method is that the propagation velocity depends intimately on the translational and rotational temperatures and so temperatures deduced using this method represent the true gas temperature - without the need of having to make even an approximate correction.

6.4.4. Estimate of difference between temperature of thermocouple and gas.

To assess whether the differences between the ultra-sonic gas temperature measurements and the thermocouple temperatures could in fact be attributed to heat transfer processes between the thermocouple wire and its surroundings an estimate of the temperature difference between the gas and the wire was made.

Under steady conditions the heat flow from the gas stream to the wire by convection exactly balances the heat losses from the wire due to radiation and along the wire due to conduction. The heat transfer equation for an element of wire of length dx is therefore

$$\alpha\pi D(T_{gx} - T_x).dx - \frac{D\sigma}{4}\int^{4\pi}\left[\epsilon_x T_x^4 - \epsilon_w T_w^4\right]d\omega.dx + \frac{\pi K D^2}{4}\frac{d^2T_x}{dx^2}.dx = 0 \qquad \ldots 6.3$$

where α is the heat transfer coefficient between the gas stream and the wire, D is the diameter of the wire, T_{gx} is the temperature

of the gas at a distance x along the wire, T_x is the temperature of the wire at x, σ is Stephan's constant, ϵ_x is the emissivity of the wire at x, ϵ_w is the emissivity of the surroundings and is a function of position, T_w is the temperature of the surroundings and is a function of position, and K is the thermal conductivity of the wire.

In general α varies with x on account of its dependence on temperature and velocity. Here, however, it is replaced by an effective heat transfer coefficient for the whole length of the wire. In evaluating the radiation term it was necessary to consider the heat gained due to radiation from the electric heater as well as the heat lost to the surroundings. This compensating effect tended to reduce the magnitude of the radiation correction. Also the relatively low junction temperatures and large wire diameter all contributed towards making the conduction term the predominant loss mechanism. An approximate estimate of the magnitude of the radiation correction can be made by considering that all the heat lost by the wire is by radiation only. This gives a maximum possible value for $T_{gas} - T_o$ where T_o is the junction temperature.

The radiation correction was calculated using Kaskan's equation[72]

$$T_{gas} - T_o = \frac{1.25 \epsilon_o D^{3/4}}{K_g} \left[\frac{\pi}{\rho v}\right]^{\frac{1}{4}} (T_o^4 - T_w^4) \quad \ldots 6.4$$

where ρ is the density of the gas, K_g the thermal conductivity of the gas and v is the gas velocity. The corrections calculated using this expression are listed in Table 10.

It is clear from Table 10 that the radiation correction on its own cannot account for the differences between the ultra-sonic gas temperature measurements and the thermocouple temperatures. If conduction is assumed to be the dominant loss mechanism equation 6.3 becomes

$$\frac{d^2T_x}{dx^2} + \frac{4\alpha}{KD}(T_{gx} - T_x) = 0 \qquad \ldots 6.5$$

Before this equation can be solved for T_x some knowledge of the spatial variation of the gas temperature T_{gx} is required. Ideally it is best to try to arrange for the wire to be stretched along an isotherm so that T_g can be taken as a constant independent of x. Unfortunately such an assumption in this case would not be realistic as the distance in which the gas fell from its maximum value to room temperature extended over an appreciable length of the wire. A more reasonable approach is to assume that the maximum gas temperature is proportional to the temperature of the thermocouple junction ($x = 0$) such that $T_{go} = aT_o$. If this proportionality is assumed to exist along the length of the wire (i.e. $T_{gx} = aT_x$) the above equation simplifies to

$$\frac{d^2T_x}{dx^2} + m^2T_x = 0, \qquad \ldots 6.6a$$

where

$$m^2 = \frac{4\alpha}{K\,D}(a - 1) \qquad \ldots 6.6b$$

The solution of equation 6.6 is

$$T_x = E\cos mx + F\sin mx \qquad \ldots 6.7$$

At $x = 0$, $T_x = T_o$ and $dT_x/dx = 0$ and so this becomes

$$T_x = T_o \cos mx \qquad \ldots 6.8$$

At x = L, i.e. at the end of the thermocouple wire held in the clamp the temperature of the wire is equal to the clamp temperature, T_L. Solving this last equation for m at x = L gives

$$m = \frac{1}{L} \cos^{-1}\left(\frac{T_L}{T_o}\right) \qquad \ldots 6.9$$

Combining this with equation 6.6b and solving for a gives

$$a = 1 + \frac{K D}{4 \propto L^2}\left[\cos^{-1}\left(\frac{T_L}{T_o}\right)\right]^2 \qquad \ldots 6.10$$

As $T_{go} = aT_o$ one finally obtains for the gas temperature immediately adjacent to the thermocouple junction

$$T_{go} = T_o\left\{1 + \frac{K D}{4 \propto L^2}\left[\cos^{-1}\left(\frac{T_L}{T_o}\right)\right]^2\right\} \qquad \ldots 6.11$$

Equation 6.11 was used to correct the thermcouple readings given in Table 8. The constants used for this evaluation were $K = 0.88 cal.cm^{-1}.s^{-1}.{}^{o}C^{-1}$, $D = 1.78 \times 10^{-2} cm$, L = 2.5cm and $T_L = 300^{o}K$. The values used for the heat transfer coefficient are listed in Table 9 and were taken from the curves given in Appendix 2 assuming that the effective gas velocities were $26 cm.s^{-1}$ and $30 cm.s^{-1}$ for air, and $39 cm.s^{-1}$ and $45 cm.s^{-1}$ for argon, for the low and high temperatures respectively.

TABLE 9

Heat transfer coefficients, $\propto$, for a 36 swg (0.0178cm) wire in air and in argon

GAS	$\propto (cal.cm^{-2}.s^{-1}.{}^{o}C^{-1})$	
	400°C	500°C
air	9.8×10^{-3}	10.5×10^{-3}
argon	5.7×10^{-3}	6.1×10^{-3}

Table 10 compares the corrected thermocouple temperatures with the ultra-sonic gas temperature measurements. The ± 10° error in the thermocouple temperature represents only the reading error; it does not take into account any errors that may have been introduced in making the corrections.

TABLE 10

Comparision between ultra-sonic gas temperature measurements and corrected thermocouple temperatures

Gas	Uncorrected thermocouple temperature °K	Radiation temperature correction °K	Conduction temperature correction °K	Corrected thermocouple temperature °K	Ultrasonic gas temperature °K
air	683±10	17	53	753±10	770±15
air	773±10	18	64	855±10	863±116
argon	673±10	14	90	777±10	765±16
argon	778±10	19	112	909±10	904±28

The degree of agreement between the two methods of gas temperature measurement is quite remarkable, particularly when one considers the approximations made in correcting the thermocouple readings.

6.4.5. Discussion of results.

According to equation 5.35 the marking of sound waves in argon should be 1.07 times greater than in air. The fact that the marking in argon is poorer than in air is almost certainly due to a perturbation in the wavefront of the waves entering the interface. This wavefront perturbation probably also accounts for the overall poor marking in Figures 6.8 and 6.9.

In the absence of dispersion effects the marking in carbon dioxide should be 3.00 times that in air. However Figure 6.10

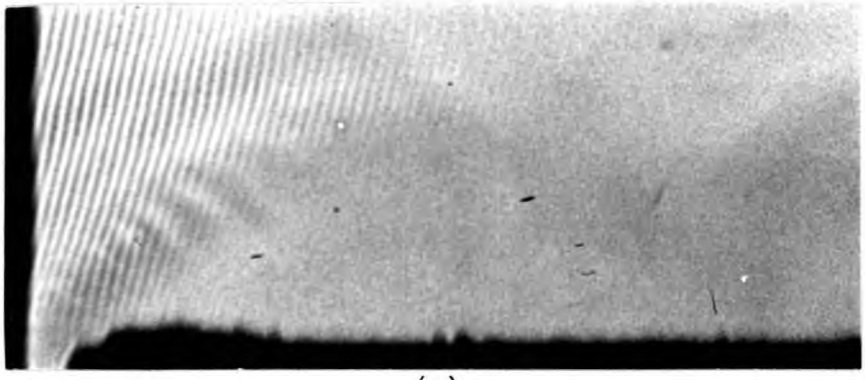

(A)

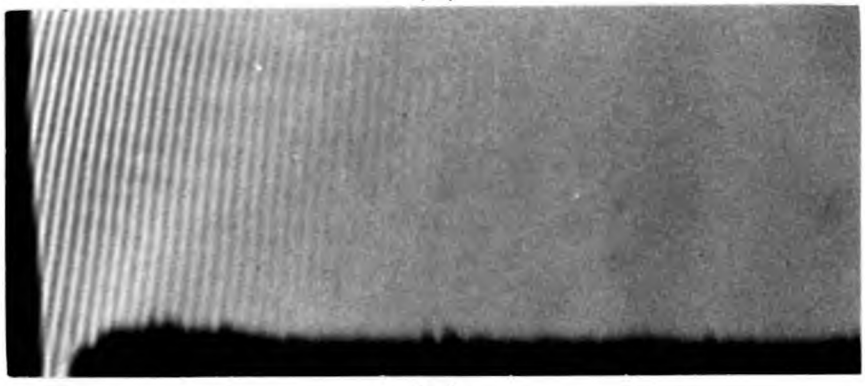

(B)

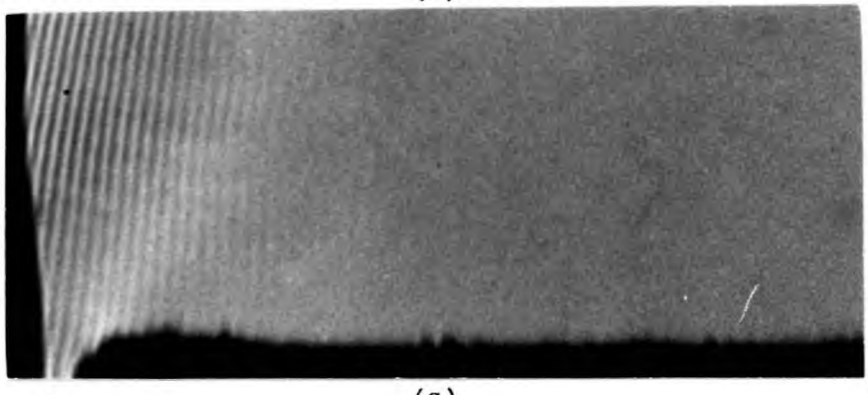

(C)

0.7MHz ultra-sonic waves in carbon dioxide. (A) at room temperature (B) thermocouple temperature of 400°C and (C) thermocouple temperature of 500°C. Power density 125mW.cm^{-2} and acoustic beam width 3.0cm.

FIGURE 6.10

shows that in spite of this the marking is very much less than in both air and argon. This suggests that in carbon dioxide some other form of attenuation must be present, i.e. dispersion attenuation.

6.5. CONCLUSIONS.

It has been shown that the ultra-sonic method of gas diagnostics can be used for the measurement of gas temperatures up to almost 1000°K. However, there is a problem of achieving good marking of the wavefronts and this appears to be due to perturbations of the acoustic wavefronts on entering the gas flow being studied and, in some systems, also due to attenuation of the acoustic beam by dispersion effects. This may well be the case in gas flows containing carbon dioxide. Marking could be improved by working at higher acoustic power densities. If this is done there is no obvious reason why the method cannot then be extended to higher temperatures.

CHAPTER 7

SUBTRACTIVE INTERFEROMETRY

7.1. INTRODUCTION.

Laser radiation has produced such a favourable mutation in interferometer design that it has resulted in the evolution of a completely new species of interferometer. As a consequence of this interferometry, in particular subtractive interferometry, has become a very simple diagnostic tool.

The design and use of a particularly simple subtractive interferometer, suitable for combustion studies, is described and it is shown how its performance may be interpreted both in terms of Moiré fringes and holographic concepts. It is also shown how the problem of residual fringes, ever present in practical interferometers, can be solved and how the disturbing effects of poor quality windows within the test space can be eliminated. The use of a high temperature region as a reference state is particularly advantageous in interferometry: it is demonstrated how this may be done when studying, for example, the changes in phase that occur when a heat sink is immersed in a flame.

Interferometry is used in combustion research for obtaining the spatial distribution of temperature and composition in, for example, flame gases and in the gaseous boundary layer separating a gas at one temperature and a solid at another. If in a particular system the refractive index is primarily a function of temperature

(composition effects being sometimes negligible) the temperature distribution may be deduced from a measurement of the refractive index distribution within the system. It is not possible to measure the refractive index distribution directly and this has to be inferred from a measurement of the change in phase distribution that occurs when a beam of light transluminates the phase object. The three dimensional nature of most phase objects makes it possible to relate changes in phase to a three dimensional distribution in refractive index only for certain phase object geometries such as, for example, axially symmetric systems. In combustion this does not usually present much of a problem as one can often choose whatever geometry is most suitable. However, here the problem is not one of interpretation but rather one of recording the phase distribution in an unambiguous manner using subtractive interferometry.

Subtractive interferometry may be thought of as the comparison of the wavefront profile of the test beam emerging from a phase object with the wavefront profile of the same test beam at a different time. In other words it is the study of the phase changes that occur in the test beam in the time interval separating the recording of the two wavefronts. Ordinary interferometry, on the other hand, is the instantaneous comparison of the wavefront profile of the test beam emerging from a phase object with the profile of a reference wavefront of accurately known structure.

The need for some form of subtractive interferometric technique has been appreciated ever since attempts were made to make interferometers of large cross-sectional working area. Cost

limitations make it impractical to manufacture large diameter optical components to such close tolerances that the differences in wavefront profile of the test and reference beams are much less than half a wavelength of light. At best practically all interferometers will form at least a few fringes (known as residual fringes) in the interferogram in the absence of a phase object in the test beam. The subtraction of the effects of these residual fringes from the interferogram formed when a phase object is present in the test beam to give a 'difference' interferogram is known as subtractive interferometry. Various attempts have been made in the past to automatically correct an interferogram for the presence of these residuals. Up until recently the methods employed (for example ref. 6d) have usually been somewhat tedious as a result of having to use thermal light sources. The availability of laser light sources, and in particular the advancement of double exposure holographic techniques have recently (e.g refs 73 and 74) enabled very much simpler methods to be used.

7.2. PRINCIPLES OF SUBTRACTIVE INTERFEROMETRY.

7.2.1. Introduction.

The principles of subtractive interferometry may best be understood by considering the theory of an ordinary two beam interferometer. By doing this it can be shown that all interferometry has to be a form of subtractive interferometry in order that the effects of optical imperfections within the interferometer may be eliminated. A number of ways of obtaining difference

interferomgrams are described.

7.2.2. Generalized two beam interferometer theory.

It is sufficient here to discuss interferometer theory in very general terms: the detailed theory and performance of numerous interferometers may be found in reference 6 for thermal light sources, and in reference 7 for laser light sources.

Consider the parallel beam interferometer arrangement shown in Figure 7.1. Let the reference beam be inclined at an angle θ to the test beam. Let the test space be situated between $0 < x < X$ and let this be imaged with a magnification of +1 onto the image plane at $x = x_i$. Let the three dimensional absolute refractive index distribution of the phase object be represented by the function $n(x,y,z)$ and let the absolute refractive index of the surrounding space, including the reference space, be n_r.

In general a phase difference $\phi(x_i,y,z)$ will exist between the test and reference beams at the image plane as a result of the presence of the phase object in the test beam, defects or mismatch in optical components and differences in beam geometry.

Thus (providing deflections are small)

$$\phi(x_i,y,z) = \frac{2\pi}{\lambda_o}\int_0^X [n(x,y,z) - n_r]\,dx \qquad \text{(due to phase object)}$$

$$+ \phi_d(x_i,y,z) \qquad \text{(due to optical defects)}$$

$$+ \frac{2\pi}{\lambda_o} n_r L \qquad \text{(due to differences in beam length, L, at } x_i,y,z\text{)}$$

$$+ \frac{2\pi}{\lambda_o} n_r y \sin\theta \qquad \text{(due to differences in angle at the image plane)}$$

where λ_o is the free space wavelength of the light used.

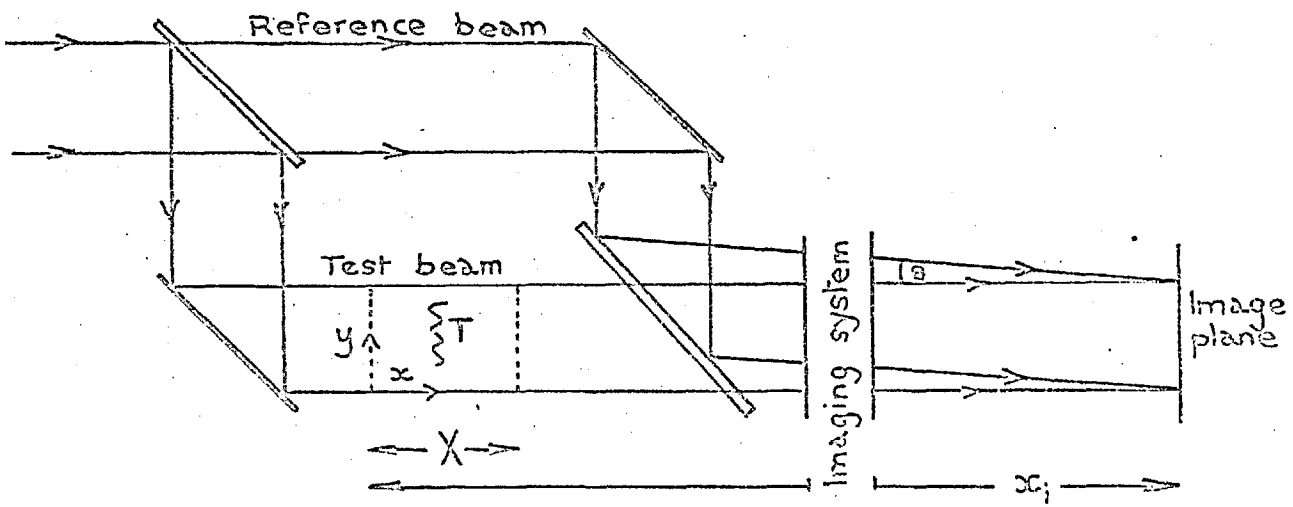

FIGURE 7.1

Co-ordinate system used in generalized two beam interferometer theory. T, phase object of refractive index n(x,y,z); x, distance co-ordinate along beam; X, thickness of phase object; x_i, image co-ordinate; Θ, angle between test and reference beams at the image plane.

Wherever the phase difference $\phi(x_i,y,z)$ between the two interfering beams is equal to a multiple of 2π a bright interference fringe occurs in the resulting interference pattern. It is more convenient for interpreting the interferogram to express the phase distribution in terms of a fringe order number distribution N where

$$N = \frac{\phi}{2\pi} \qquad \ldots 7.2$$

Converting equation 7.1 into a fringe order number distribution gives

$$N(x_i,y,z) = \frac{1}{\lambda_o}\int_0^X [n(x,y,z) - n_r]\,dx + N_d(x_i,y,z) + \frac{n_r L}{\lambda_o} + \frac{n_r y \sin\theta}{\lambda_o}, \qquad \ldots 7.3$$

where $N_d(x_i,y,z)$ is the fringe order number distribution of the residual fringes arising from the optical defects in the interferometer.

The fringe order number at $(x_i,0,0)$ is

$$N(x_i,0,0) = \frac{1}{\lambda_o}\int_0^X [n(x,y,z) - n_r]\,dx + N_d(x_i,0,0) + \frac{n_r L}{\lambda_o} \qquad \ldots 7.4$$

If the geometry of the phase object is such that $n(x,0,0) = n_r$ it follows from equation 7.4 that

$$\frac{n_r L}{\lambda_o} = N(x_i,0,0) - N_d(x_i,0,0) \qquad \ldots 7.5$$

Substituting equation 7.5. into equation 7.3 gives

$$N(x_i,y,z) - N(x_i,0,0) = \frac{1}{\lambda_o}\int_0^X \left[n(x,y,z) - n_r\right] dx + N_d(x_i,y,z) - N_d(x_i,0,0) + \frac{n_r y \sin\theta}{\lambda_o} \qquad \ldots 7.6$$

If the interferogram fringes are counted using the fringe at $(x_i,0,0)$ as the origin one may write

$$N(x_i,y,z) - N(x_i,0,0) = N_I(x_i,y,z) \qquad \ldots 7.7a$$

and

$$N_d(x_i,y,z) - N_d(x_i,0,0) = N_{dI}(x_i,y,z) \qquad \ldots 7.7b$$

The integrated absolute refractive index distribution can then be expressed in terms of measurable quantities. Hence

$$\frac{1}{\lambda_o}\int_0^X \left[n(x,y,z) - n_r\right] dx = N_I(x_i,y,z) - N_{dI}(x_i,y,z) - \alpha y \qquad \ldots 7.8$$

where α is defined by

$$\alpha = \frac{n_r \sin\theta}{\lambda_o}, \qquad \ldots 7.9$$

and is the spatial shear fringe frequency along the y-axis in the absence of residual fringes, and a phase object in the test beam.

7.2.3. 'Infinite' fringe arrangement.

By making θ, and hence α, equal to zero an aberration free interferometer will form, in the absence of a phase object in the test beam, an infinitely wide interference fringe. However, equation 7.8. predicts that for a practical interferometer a fringe order number distribution given by

$$N_I(x_i,y,z) = N_{dI}(x_i,y,z) \qquad \ldots 7.10$$

will be observed.

When a phase test object is present in a real interferometer adjusted for the infinite fringe condition the integrated absolute refractive index distribution is given by

$$\frac{1}{\lambda_{o_0}}\int_0^X [n(x,y,z) - n_r]dx = N_I(x_i,y,z) - N_{dI}(x_i,y,z) \qquad \ldots 7.11$$

and cannot be evaluated unless $N_{dI}(x_i,y,z)$ is known. This cannot be deduced from a simple 'infinite' interferogram of the residual fringes as it is impossible to tell just by looking at the interferogram whether their order number increases or decreases with increasing y and z. To find this information some auxiliary experiment is usually necessary.

7.2.4. 'Finite' fringe arrangement.

When Θ is not zero an aberration free interferogram will form in the absence of a phase object in the test beam a set of equispaced interference fringes parallel to the z-axis. However, for a practical interferometer equation 7.8 predicts that a fringe order number distribution given by

$$N_I(x_i,y,z) = N_{dI}(x_i,y,z) + \alpha y \qquad \ldots 7.12$$

will be observed. If the effects of the shear term, αy, dominate the effects of the residual fringes N_{dI} the residual fringe order number distribution (including its sign) can easily be found.

If a phase test object is present in a real interferometer, adjusted for the finite fringe condition, the integrated absolute refractive index distribution is given by

$$\frac{1}{\lambda_{o_0}}\int_0^X [n(x,y,z) - n_r]dx = N_I(x_i,y,z) - N_{dI}(x_i,y,z) - \alpha y \qquad \ldots 7.13$$

As the last two terms in equation 7.13 are the same as in equation 7.12 the combined effect of the residual fringes and the shear fringes can be deduced from a measurement of $N_I(x_i,y,z)$ in the absence of the phase object, and then eliminated. This is considerably easier to do than in the case of an 'infinite' fringe interferogram.

7.2.5. Subtractive methods.

With the 'infinite' and 'finite' fringe arrangements described above it was necessary to first evaluate and then subtract the effects of the residual fringe distribution before the integrated refractive index distribution could be found. However, there is a very much simpler subtractive method whereby the refractive index distribution can be found without having to actually evaluate $N_{dI}(x_i,y,z)$. The principle of the method is based on the superposition of two finite fringe interferograms, one made with one and the other without or with another phase object in the test beam.

If N_{I1} and N_{I2} are the observed fringe order number distributions when phase objects of refractive index distribution $n_1(x,y,z)$ and $n_2(x,y,z)$ are respectively placed in the test beam it follows from equation 7.8 that

$$\frac{1}{\lambda_o}\int_0^X \left[n_1(x,y,z) - n_2(x,y,z)\right]dx = N_{I1} - N_{I2} \quad \ldots 7.14$$

If N_{I1} and N_{I2} are primarily determined by the shear term αy they effectively represent two grating like fringe patterns of nominal fringe frequency equal to α, but each having slightly different

local fringe frequencies due to the differences in structure of the two phase objects. When the two interferograms are superimposed the slight differences in local fringe spacing give rise to Moiré fringes. These dark Moiré fringes occur at points where M_I defined by

$$M_I = N_{I1} - N_{I2} \qquad \ldots 7.15$$

is equal to $(m + \frac{1}{2})$ where m is an integer (including zero). Thus the first dark fringe corresponds to a contour along which there has occured a relative phase shift of π.

If equation 7.15 is substituted into equation 7.14 it has the same form as the equation for an 'infinite' fringe, aberration free, interferogram. There is a fundamental difference however. Previously the reference state corresponded to n_r, the refractive index of the surroundings, while here it is completely arbitrary. Also as the left hand side of equation 7.14 represents the difference between two refractive index distributions in the test space a constant term (for example the refractive index distribution corresponding to a poor quality window or other complicated refractive index distribution) could be added to these distributions at each exposure and the same difference still be obtained.

There are a number of ways in which the two interference patterns may be combined and the resulting 'difference' interferogram or Moiré fringes extracted. These will now be discussed.

A) Double exposure/double plate method.

The interferometer is adjusted so that the shear term is dominant in controlling the form of the resulting interference

fringes. Two interferograms are then recorded on two separate photographic plates, one with and the other without the phase object being present in the test space. The two plates are then processed (as negatives) to a high density and then carefully superimposed to obtain point to point correspondence within the test space.

Outside the phase object the interference fringes of the two interferograms coincide exactly and the overall transmission of the two plate combination is grey (i.e. 50% clear and 50% opaque). In moving in towards the phase object the fringe spacing in one of the interferograms changes slightly with respect to the other. Eventually a region is reached where the maximum in one interferogram coincides with a minimum in the other and the overall transmission of the two plate combination reduces to zero (i.e. 100% opaque). The first black Moiré fringe occurs wherever there has been a relative phase shift of π, and each subsequent fringe is separated from the last by 2π. Grey fringes occur wherever there has been a relative phase shift of 2π and these too are separated from each adjacent grey fringe by 2π. From the point of view of interpreting the resulting Moiré interferogram using equations 7.14 and 7.15 it is the grey fringes that have to be counted as it is a grey fringe that occurs at the origin $(x_i, 0, 0)$. The disadvantage of this method of obtaining an aberration free order number distribution is that it requires two separate photographic recordings which then have to be superimposed exactly.

B) Double exposure/single plate method.

The interferometer is again adjusted so that the shear term is dominant in controlling the form of the resulting interference fringes. Without moving the photographic plate between exposures two interferograms are recorded on the same photographic plate, one with and the other without the phase object in the test beam. The plate of the two superimposed interferograms is then processed (as a negative).

The position of the dark interference fringes outside the phase object remain unaltered between exposures. These fringes and the parts of the other dark fringes within the phase object that suffer a displacement of 2π and multiples of 2π are twice as great (assuming two equal exposures) as the fringes which suffer a displacement of π and odd multiples of π. The exact effect this has on the processed plate's transmission depends on the plate's density-exposure characteristic curve. However, the overall effect is that in regions outside the phase object the difference interferogram is dark. On entering into the phase object there occur alternate regions of first light and then dark difference interferogram fringes. The first light fringe corresponds to a relative phase shift of π while the first dark fringe corresponds to a relative phase shift of 2π.

This arrangement is simpler than in method A) in so far as only one plate is needed and there is now no problem in obtaining exact superposition of the two interferograms. An interpretation problem may exist if the spacing of the shear fringes is comparable

to the width of the resulting difference interferogram fringes. For this reason it is best to make the shear angle θ as large as possible. Although the ambiguity in interpreting the correct aberration free order number distribution decreases with increasing α the processing of the plate so as to make the resulting difference interferogram easily visible, becomes progressively more critical. However, if α is so large that the difference fringes are invisible to the naked eye they can generally be located by using a microscope that is capable of resolving the shear fringes.

C) Holographic reconstruction method.

The interferometer is adjusted so that the shear angle θ is greater than the maximum angular deflection produced by the phase object. Without moving the photographic plate between exposures two interferograms are recorded on the same plate, one with and the other without the phase object in the test beam. The plate of the two superimposed interferograms is, when processed (as a negative) a double exposed hologram of the test space. Ideally, therefore, exposures should be so arranged that the resulting amplitude transmittance of the processed plate (i.e. the hologram) falls on the linear portion of the plate's amplitude transmittance-exposure characteristic curve[24]. However, as the hologram is essentially the same as a side-band Lieth and Upatnieks type hologram[75] the exact exposure and processing procedure used is not critical[15]. Therefore, the recording of the double exposure interferogram is exactly the same as in the previous method. The difference between the two methods is in the way the two super-

imposed interferograms are subtracted to give the required difference interferogram.

If only one exposure was taken the interference pattern on the processed plate would simply have a grating structure and consist of approximately equispaced continuous interference fringes. When this fringe pattern is illuminated with the same reference beam that fell on the plate during the recording process the transmitted light becomes diffracted by the grating. One of the diffraction orders of this light is in fact a reconstruction of the original test beam and, by using an imaging system can reform an image of the original test space. Whether the test space contained a phase object or not the image of the test space would be of uniform illumination.

When two exposures are taken on the same plate, one with and one without a phase object in the test beam, the interference pattern on the processed plate (i.e. the double exposed hologram) will still have basically the same grating structure as before but some of its interference fringes will be washed out as a result of maxima in one of the interferograms coinciding with minima in the other. These regions of wash out occur along contours corresponding to relative phase shifts of π and odd multiples of π. If this double exposed hologram is now illuminated by the original reference beam the areas of the hologram in which the fringes have been washed out will be unable to diffract and hence contribute to the reconstruction of the original test beam. When this partially reconstructed beam is used to form an image of the test space the

illumination in the image is no longer uniform but is interrupted with dark fringes. These fringes correspond to regions in the test space in which there has been a relative phase shift of π and odd multiples of π between exposures.

The advantage of this method over methods A) and B) is that higher shear angles can be used and hence less ambiguity occurs in locating the exact position of the difference interference fringes. A holographic reconstruction gives a clear high contrast record of these fringes and it is infinitely easier to obtain these than to use a microscope to locate the difference fringes in the double exposed interferogram.

7.3. DESIGN AND PERFORMANCE OF INTERFEROMETER.

7.3.1. Introduction.

The design and performance of an extremely simple interferometer is described, and it is shown how it can be used to obtain difference interferograms.

7.3.2. Light source.

A Scientifica and Cook Electronics B18/3 8mW d.c. uniphase helium-neon gas laser was used as a light source. This was sufficiently powerful to enable very short exposure times ($\sim 10^{-2}$s) to be used during the recording process, and not too long exposure times ($\sim$10s) to be used when making holographic reconstructions. Without the excellent spatial and temporal coherency of such a laser the method of beam splitting used here would be impossible, and the interferometer's great virture of extreme simplicity would be lost.

7.3.3. Optical system.

Figure 7.2 shows the interferometer in its final form. Not only is it simple to construct and to align but it has the advantage of requiring no more optical components than are used in an ordinary parallel beam schlieren system. If large aperture lenses are not available they could easily be replaced by schlieren mirrors.

It is seen in Figure 7.2 that one half of the parallel beam between the collimating and schlieren lenses acts as the test beam and the other half as the reference beam. The purpose of the beam splitter is to divide the beam into two (division of amplitude) and then to superimpose the reference half of one beam with the test half of the other. Therefore, the heart of the interferometer lies in the beam splitting arrangement and this is shown in greater detail in Figure 7.3. The test beam was reflected off the front surface of the first glass wedge W_1 (which was half a Fresnel biprism) and the reference beam was reflected off a second glass wedge W_2 (which was the plane face of a plano-convex lens). As only ~1/25th of the incident light is reflected off each interface the intensity of the test and reference beams were essentially the same. Wedges were used as beam splitters so that the unwanted back reflections could easily be deflected out of the optical system. So as to be able to adjust the angle of shear between the test and reference beams, at the recording plane, the wedges were mounted as shown in Figure 7.3a.

If d is the separation of the beam splitters, and β is the

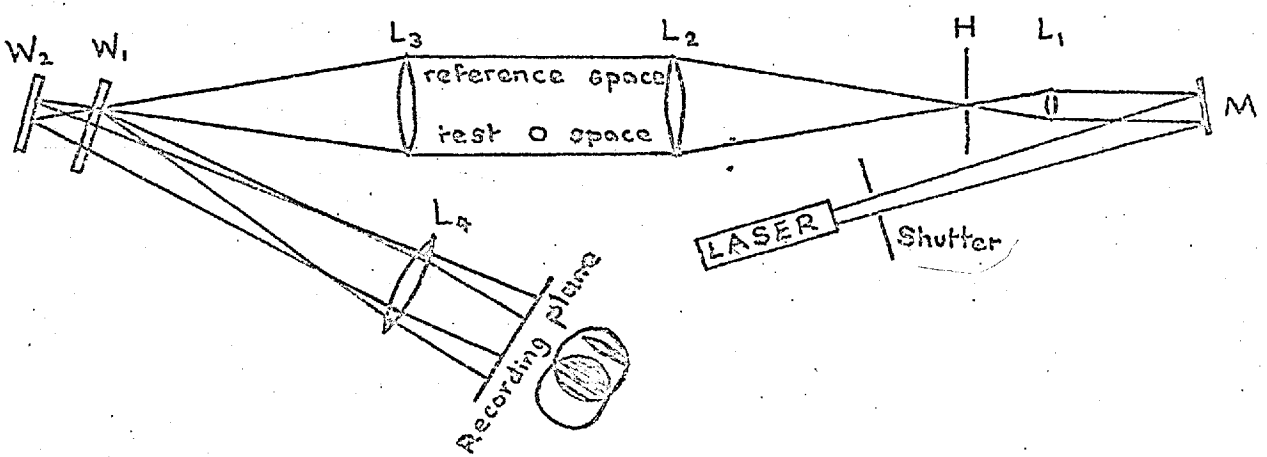

FIGURE 7.2

Interferometer. L_1, lens for expanding laser beam; H, pin-hole; L_2, collimator lens; L_3, schlieren lens; W_1, W_2 beam splitters; L_4, imaging lens.

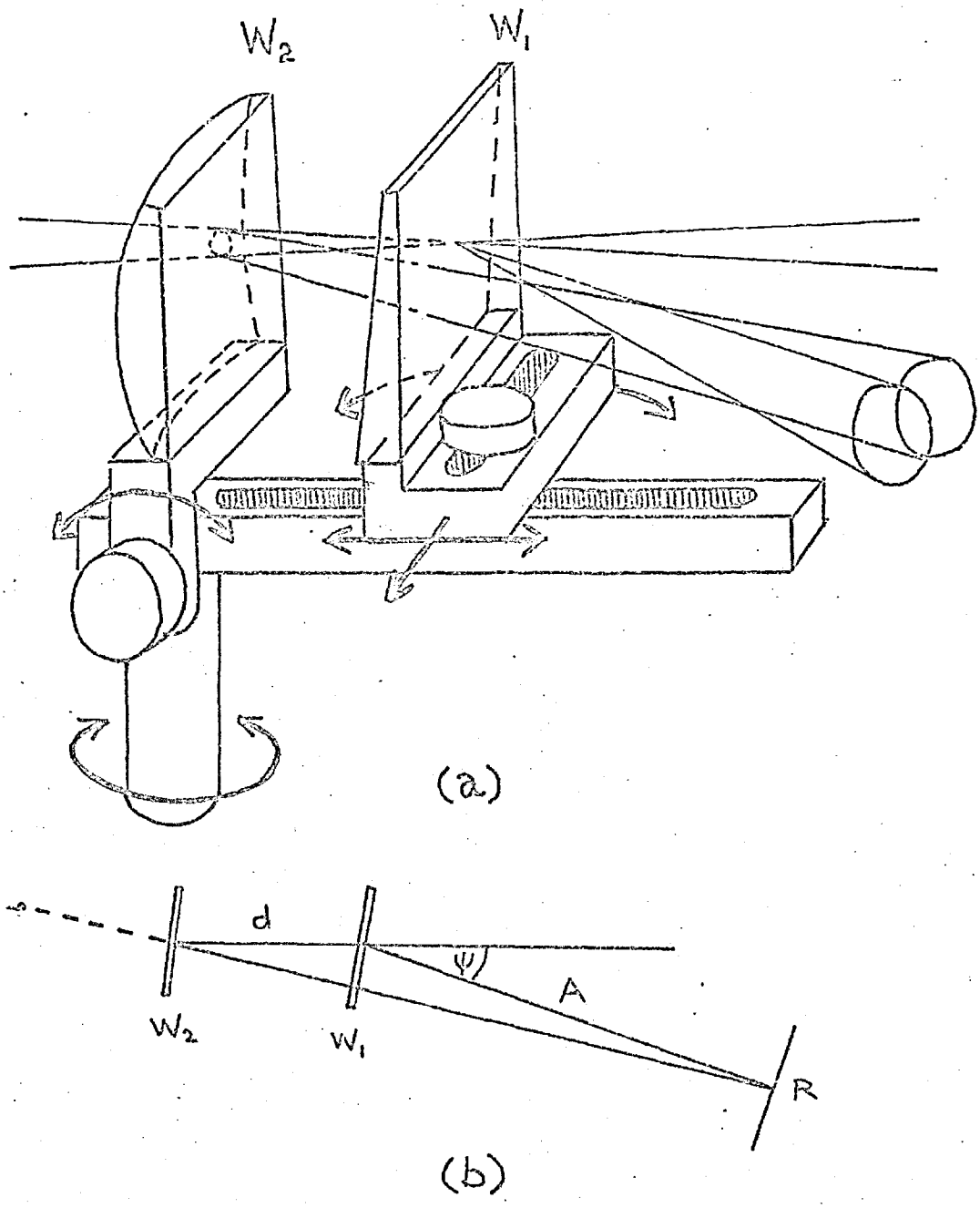

Design of beam splitter arrangement used in interferometer shown in Figure 7.2 showing degrees of freedom.

FIGURE 7.3

angle between the test beam and the optic axis of the schlieren lens after reflection at W_1, as shown in Figure 7.3b, the angle between the test and reference beams, θ, is given by

$$\sin\theta = \frac{d\sin\psi'}{(A^2+2Ad\cos\psi'+d^2)^{\frac{1}{2}}} \qquad \ldots 7.16$$

where A is the distance between the recording plane R and the first beam splitter. In the absence of a phase object in the test beam the spatial fringe frequency is (from equation 7.9) given by

$$\propto = \frac{n_r\, d\, \sin\psi'}{\lambda_o (A^2+2Ad\cos\psi'+d^2)^{\frac{1}{2}}} \qquad \ldots 7.17$$

To achieve a reasonably uniform illumination across the width of the beam in the test and reference spaces it was necessary to considerably overfill the collimating lens with laser light. This was done using a sufficiently short focal length lens L_1 in conjunction with an 80μm diameter pin-hole H. The pin-hole acted as a spatial filter and removed unwanted diffraction rings formed by dust particles on the lens L_1 and the mirror M.

The image space was focused onto the recording plane using lens L_4. To keep image distortion to a mimimum the test beam must be the one reflected off the front face of the first beam splitter, which should be flat. The distorsion of the reference beam as a result of its double passage through the first beam splitting wedge and its reflection off the front face of the second beam splitter is unimportant. Apart from a good surface polish, which is essential whenever using laser light, the beam splitting components

do not have to be of a particularly good optical quality.

7.3.4. Choice of photographic plates.

Apart from the power output from the laser and the resolving power and sensitivity of available emulsions, the choice of photographic plate also depends on the nature of the phase object being studied. The nature of the object is important from the point of view of its stability, and its structure and size. The stability determines the maximum permissible exposure time. The structure and size of the object together with the design of the camera determines the dimensions of the image. Together these give a measure of the plate's minimum exposure ($erg.cm^{-2}$). Once the image size has been set the angle of shear required to give the necessary number of shear fringes per centimeter of image, to avoid ambiguity in the structure of the fringes in the difference interferogram, can be calculated.

To assess the recording properties of a number of photographic plates that may be suitable for recording holograms of phase objects encountered in combustion research the interferometer was set up to form an image of the test space, at a magnification of ~1/3 and with a spatial frequency of the shear fringes of 25/mm. This corresponds to about 8/mm of object space.

Tests were made to find the exposure times that would give the best fringe profiles (for a spatial fringe frequency ~25/mm) for a number of different emulsions. Figure 74 shows microscope enlargements of photographs of the fringes recorded on Ilford HP3, FP4 and R52 plates, on an Agfa-Gevaert 10E70 plate and a Kodak 649F

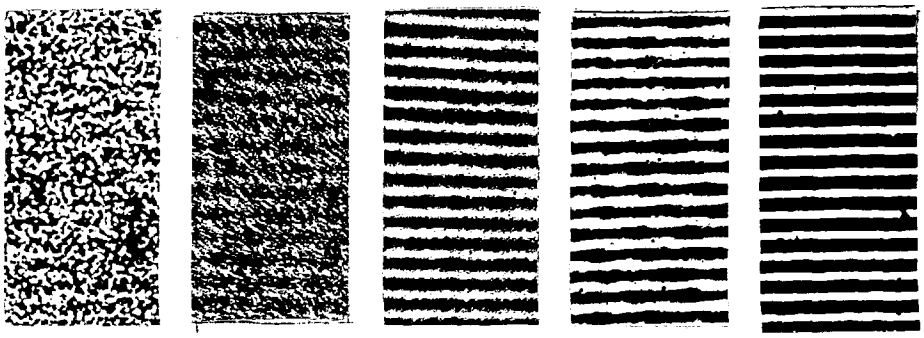

Shear fringe structure recorded on (A) Ilford HP3, (B) Ilford FP4, (C) Ilford R52, (D) Agfa 10E&O, and (E) Kodak 649F.

FIGURE 7.4

plate. Table 11 lists the exposure times and approximate exposures (based on an estimate that the laser delivers roughly 20 erg.s^{-1}.cm^{-2} to the recording plane). There was little to

TABLE 11

Plate	Exposure time(sec)	Exposure (erg.s^{-1}.cm^{-2})
ILFORD HP3	1/400	1/20
" FP4	1/400	1/20
" R52	1/100	1/5
AGFA 10E70	5	100
KODAK 649F	60	1200

choose between the Ilford R52 and the Agfa-Gevaert and Kodak plates regarding smoothness of fringe profile. However, the Ilford R52 plate was very much faster than the other two plates and was therefore chosen as the most suitable plate to use.

7.3.5. Choice of spatial shear fringe frequency.

Tests were made to see how the spatial shear fringe frequency affects the visualization of the fringes in the difference interfefogram. Figure 7.5 shows a set of double exposed holograms in which a 2inch diameter premixed flat methane-air flame was used as a phase object. The flame gases were sheathed by a fast air flow to reduce the effects of flow fluctuations caused by draughts and entrainment. The advantage of this phase object was that it exhibited a large number of interference fringes and possessed a large range of spatial fringe frequencies (in object space) from 2.2/mm at the outer boundary to 0.2/mm near the centre. These frequencies corresponded to 6.6/mm and 0.6/mm in image space.

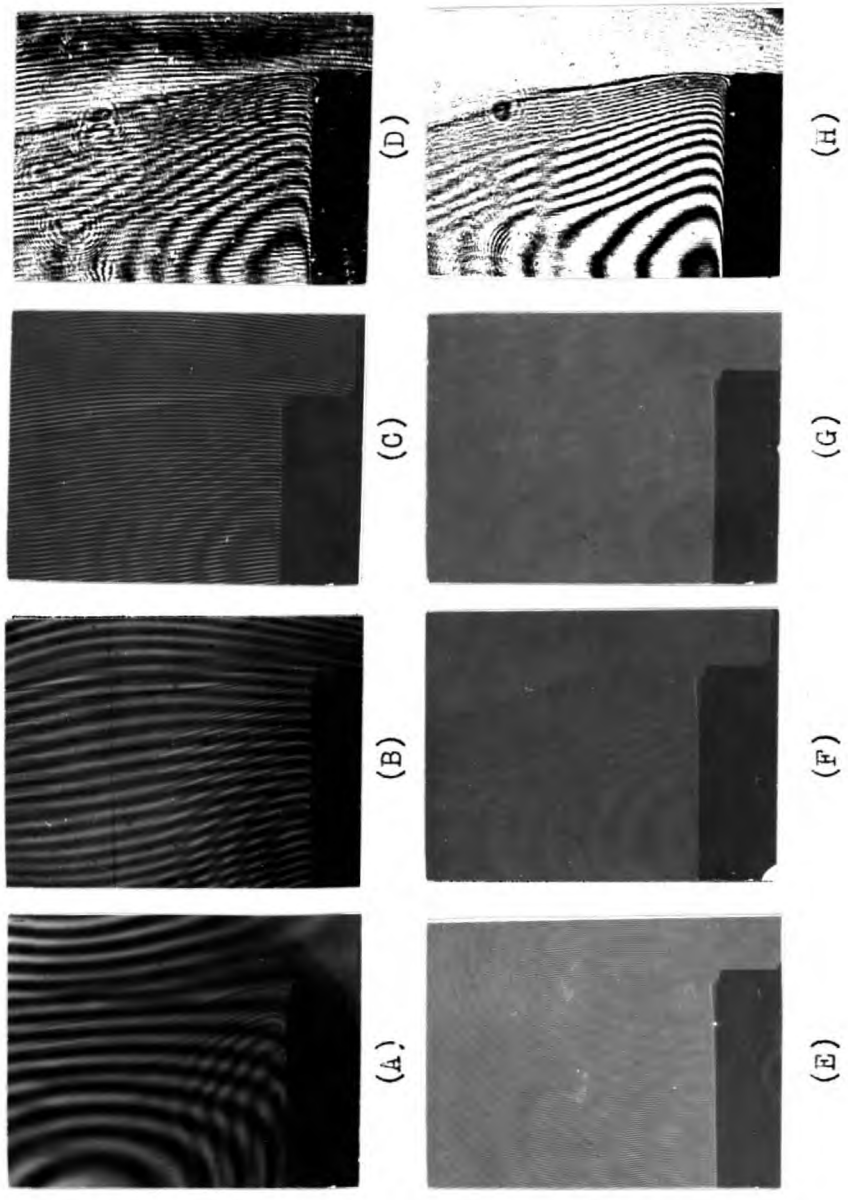

Effect of shear fringe frequency on visualization of difference interference fringes. Spatial fringe frequencies: (A) very small, (B) 1.5/mm, (C) 4.0/mm, (E) 8.5/mm, (F)18.5/mm (G) 24.0/mm. --- ((D) and (H) are holographic reconstructions obtained from (C) and (G) respectively).

FIGURE 7.5

The maximum spatial shear fringe frequencies used corresponded to about 8/mm of object space or 24/mm of image space. At the higher shear fringe frequencies it was not possible to visualize the difference interference fringes easily with the naked eye - see Figures 7.5e, 7.5f and 7.5g - and so the holographic method was used. Figure 7.5h was obtained from Figure 7.5g using this method. It can be seen that even the closest interference fringes can be resolved when using a spatial shear fringe frequency equivalent to 8/mm of object space. Figure 7.5d was obtained from Figure 7.5c also using the holographic method. In this case the spatial shear fringe frequency was equivalent to 1.3/mm and the difference interference fringes could be resolved only down to a frequency of~0.7/mm. Therefore it would appear that the holographic method can resolve difference interference fringes that have a spatial fringe frequency that is at the very most equal to half the spatial shear fringe frequency.

When the shear fringe frequency was equivalent to 1.3/mm of object space, or less, it was possible to detect the difference interference fringes directly with the naked eye - see Figures 7.6a, 7.6b and 7.6c. However, ambiguity clearly occurs whenever the difference fringe frequency is of the same order as the shear fringe frequency. It is interesting to note that in parts of Figures7.6a and 7.6b very fine difference fringes ~2.2/mm of object space can be detected in spite of the fact that the shear fringes have a spatial frequency~0.5/mm.

It was concluded that the holographic method of visualization

gave the most easily interpretable record of difference interference fringes, and that ideally the shear fringe frequency should be as high as possible and at least equal to twice the difference interference fringe frequency.

7.4. APPLICATIONS OF SUBTRACTIVE INTERFEROMETRY.

7.4.1. Introduction.

The whole point of subtractive interferometry is that firstly there is no longer any need to worry about small optical imperfections in, and the careful setting up of the interferometer, and secondly it provides a means of comparing the structure of a phase object with itself at two different times. After describing the optical details of the holographic method of forming a 'difference' interferogram it is demonstrated how the perturbing effects of a poor quality window in front of a small pre-mixed coal gas flame, stabilized on a microburner, can be eliminated. It is then shown how subtractive interferometry may be used to record the refractive index changes that occur when a heat sink is immersed in a flame.

7.4.2. Optical system.

The double exposure holograms from which 'difference' interferograms were to be obtained were all first recorded using the optical system illustrated in Figure 7.3. The specification of the system is given in OS8. The plates used were Ilford R52 and the two exposure times were 1/200s each. After processing the plate was placed back into the optical system at exactly the same position at which it was recorded. This repositioning was not particularly

difficult and after a little experience could be done quite easily. In principle it does not matter what position is selected for the recording plane providing the processed plate is always replaced into the original recording position. However, in practice the best results were always obtained when the recording plane R coincided with the image plane I_1.

QS8

S: 8mW He-Ne laser.
L_1: 1.5cm f.l.
L_2: 173cm f.l.
L_3: 173cm f.l.
d: 4.0cm.
β: 0.2Rd.
L_4: 50cm f.l.
M: 1/3.

Next the plate was illuminated by the reference beam only as shown in Figure 7.6. Figure 7.6b illustrates the reconstruction of the test beam when a double exposed hologram is illuminated by the original reference beam. The original test beam was prevented from falling on the hologram by placing a small blind B_1, as shown, between the beam splitting arrangement and the first imaging lens L_4. It was also necessary to prevent the direct light from the reference beam from falling onto the recording plane of the difference interferogram, i.e. the second image plane, and this was done by placing a second blind B_2 in the focal plane of the second imaging lens L_5. The resulting difference interferograms were recorded on R52 plates at exposure times, for unit magnification between the first and second imaging planes, corresponding

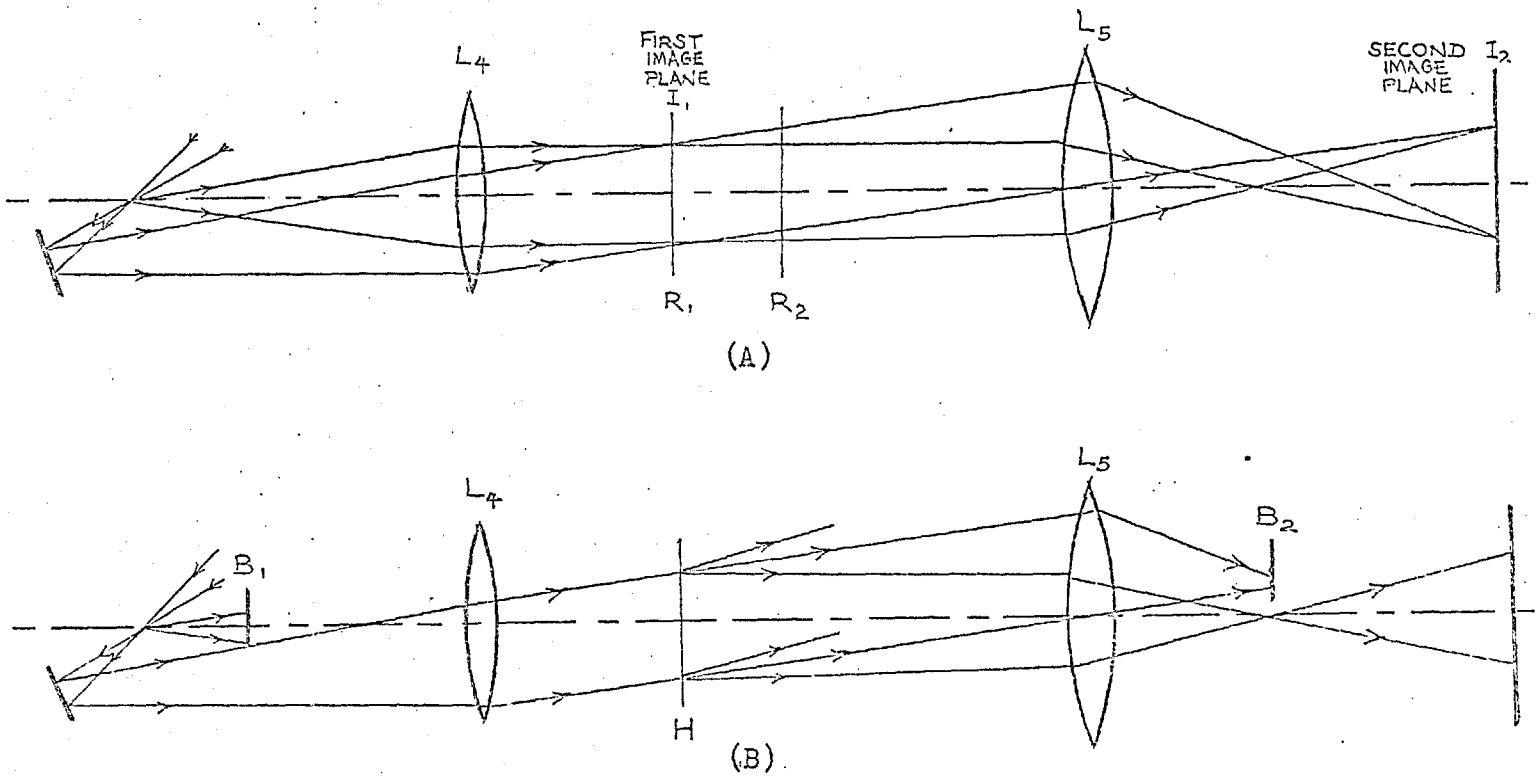

FIGURE 7.6

Ray diagrams of final section of interferometer shown in Figure 7.2. (A) shows the positions of the first and second imaging planes, I_1 and I_2. R_1 is the recording plane of a focused hologram while R_2 is the recording plane of an unfocused hologram. (B) shows how when a hologram is illuminated by the reference beam only an image of the original test object can be formed. B_1 and B_2 are blinds for removing the test beam and the zero order of the illuminating beam.

to about 10s.

It was possible to record somewhat poorer quality difference interferograms using considerably shorter exposure times equivalent to about 1/50s. These were obtained from a single exposure hologram of the phase object by placing the processed plate in the recording plane as before, and illuminating it with the test beam as well as with the reference beam. When a single exposure hologram of a phase object is illuminated with the reference beam only the complete original test beam is reconstructed. When this (weak) reconstructed test beam is combined with an unperturbed (strong) test beam low contrast 'difference' interference fringes are formed.

7.4.3. Subtractive interferometry for eliminating window aberrations.

To illustrate the effect that a poor quality optical window has on the interferogram of a flame the set of difference interferograms shown in Figure 7.7 was taken. The aberrations in the window were not so large that they introduced any serious distorsion in the imaging of the test space as subtractive interferometry cannot be used to remove such optical defects. Figure 7.7a is a difference interferogram of the piece of glass used as a window. Micrometer measurements showed that it was slightly wedge shaped and that the interferogram revealed a wedge corresponding to about four wavelengths in 5cm.

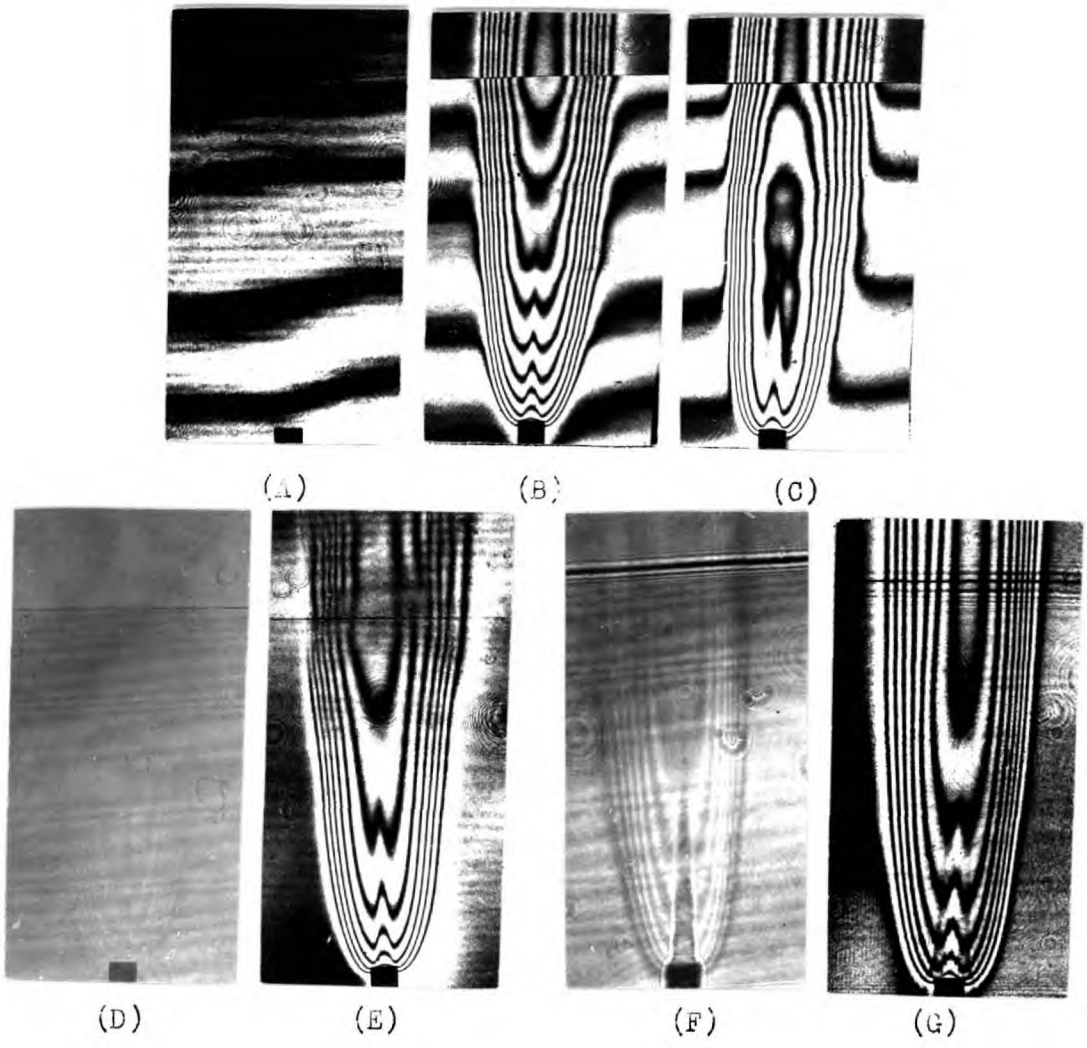

Subtractive interferometry for eliminating the effects of window aberrations. (A) interferogram of 'wedge' window, (B) and (C) interferograms of flame plus window aberrations, (D) and (F) focused and unfocused double exposure holograms, (E) and (G) interforogams of flame, with effects of window aberrations removed, obtained from (D) and (F) respectively.

FIGURE 7.7

The double exposure holograms from which Figures 7.7b and 7.7c were obtained were recorded with nothing in the test beam during the first exposure and with the window and the flame during the second exposure. Figure 7.7b is the difference interferogram that was obtained when the base of the wedge window was at the bottom while Figure 7.7c was obtained when it was at the top. These interferograms are the same as would be obtained using an ordinary (but aberration free) interferometer adjusted for the infinite fringe condition.

Figures 7.7d and 7.7f are the double exposure holograms from which Figures 7.7e and 7.7g were obtained. They illustrate how subtractive interferometry may be used to eliminate the unwanted fringes produced by the optical defects in a window. In these two cases the double exposure holograms were recorded with only the window in the test beam during the first exposure, and with both the flame and the window during the second exposure.

The difference interferograms in Figures 7.7e and 7.7g differ from one another, especially in the neighbourhood of steep refractive refractive index gradients, because their respective recording planes were not the same. Figure 7.7e was obtained from the focused double exposure hologram in Figure 7.7d which was recorded in the first image plane, while Figure 7.7g was obtained from the unfocused double exposure hologram in Figure 7.7f. Figure 7.7f was recorded in the image plane

corresponding to an object plane 120cm behind the actual test space. An unfocused image will always contain a proportion of high frequency fringes and if the recording medium is unable to resolve these fringes the derived difference interferogram will also lack high frequency detail.

Figure 7.8b illustrates the quality of the difference interferogram that can be obtained from a single exposure hologram (Figure 7.8a) using the technique described in section 7.4.2. Although it is clear from a comparison with Figures 7.7e and 7.7g that this latter method is inferior from the point of view of fringe contrast the single exposure method does have the advantage that in addition to the interferogram, schlieren and shadow records can also be obtained. These are shown in Figures 7.8c and 7.8d.

7.4.4. Subtractive interferometry for studying perturbations.

Apart from the obvious advantages of having an aberration free interferometer, subtractive interferometry enables one to compare a phase object with itself at two different times. This facility may be used for studying the refractive index changes (and hence changes in composition and temperature distribution) that occur when a heat sink is immersed in a hot gas.

Figure 7.9a is the difference interferogram resulting from the refractive index changes that occured when a water cooled heat sink, 2" deep x $\frac{3}{8}$" wide, was immersed into the combustion products above a flat 2" diameter premixed

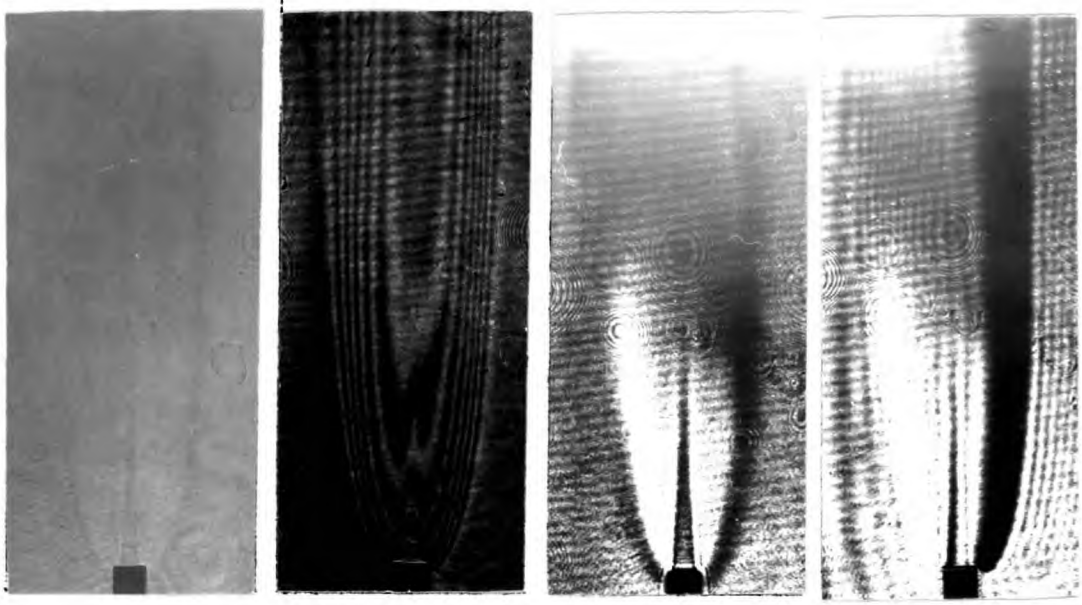

(A) (B) (C) (D)

Difference interferogram (B) obtained from single exposure hologram (A). (C) is a shadow and (D) is a schlieren also obtained from (A).

FIGURE 7.8

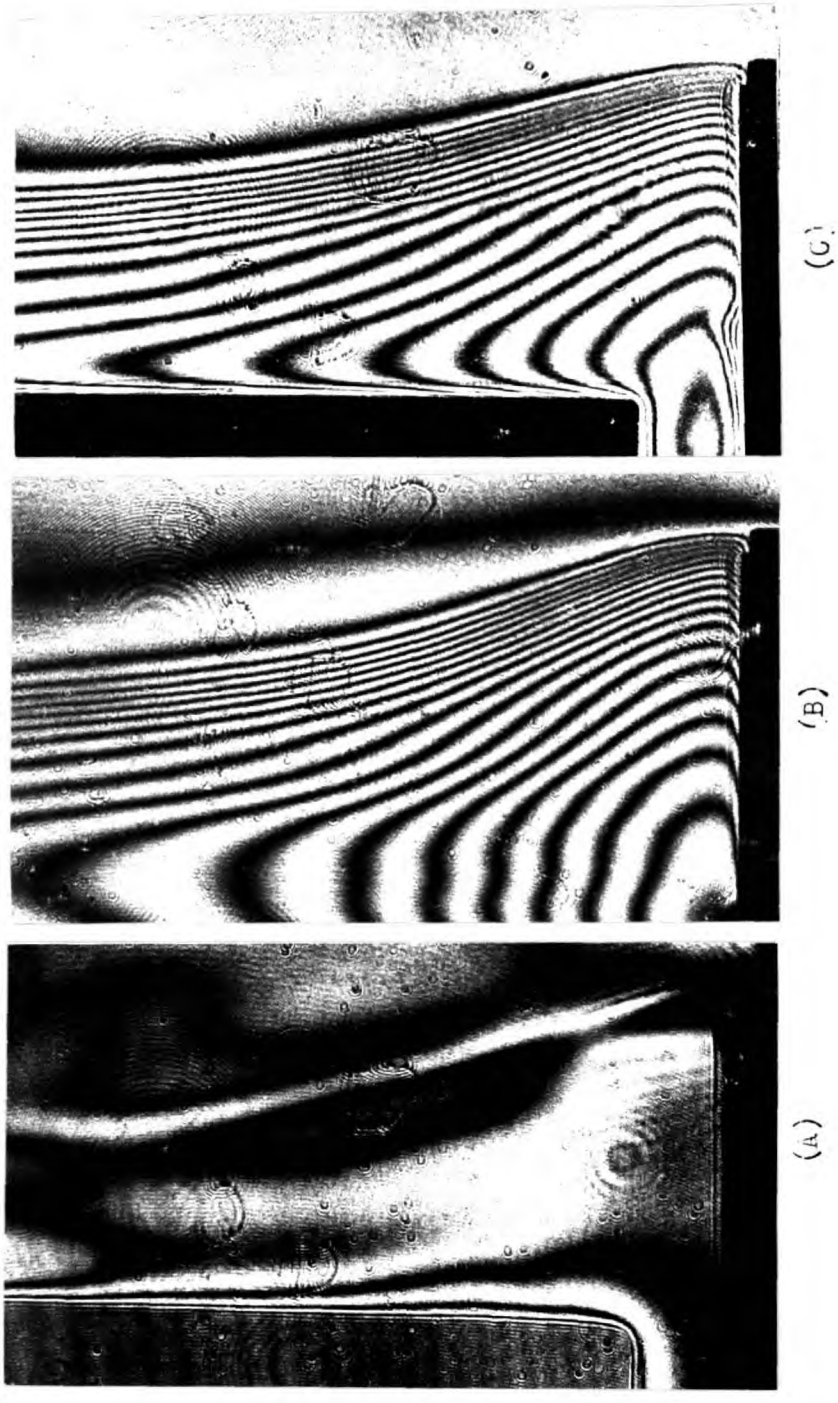

Subtraction of boundary effects using subtractive interferometry. (A) difference interferogram equivalent to subtracting (B) from (C).

FIGURE 7.9

methane-air flame. The fringes in the immediate vicinity of the heat sink represent the difference between the two interferograms shown in Figures 7.9b and 7.9c, of the flame in the absence and in the presence of the heat sink respectively.

By making the column of hot gas completely stable it should be possible using subtractive interferometry to obtain, for example, an interferogram of the relative changes that occur in the refractive index distribution in the centre of a cylindrical column of gas before and after a cylindrical heat sink is introduced. Providing the column of gas is sufficiently wide for at least part of the temperature profile to remain a known constant value between exposures this temperature region can be used as a reference state for analysing the difference interferogram. This method of examining the temperature distribution in the neighbourhood of the centre of a hot column of gas is subject to less error than in the direct analysis of, for example, the interferogram shown in Figure 7.9c.

7.5. CONCLUSIONS.

Having established a theoretical basis for the necessity and principle of subtractive interferometric methods the design of an extremely simple interferometer was proposed. The performance of this interferometer was examined and tests made on it showed that it was suitable for obtaining good difference interferograms

of flames, providing the spatial frequency of the shear fringes was large in comparison with the spatial frequency of the difference interference fringes. In the limit it appears that the shear fringe frequency must be at least equal to twice the difference fringe frequency. It was also satisfactorily demonstrated that subtractive interferometric methods may be used to eliminate the effects of optical imperfections in windows in the test space, and should simplify interferometric studies of refractive index distributions inside, for example, columns of hot gas.

This new facility of being able to subtract boundary effects is particularly useful in combustion research. In the past it has always been necessary to first penetrate a boundary envelope before being able to study what is happening, for example, in the neighbourhood of a cold quenching surface, inside the envelope. This requires first finding out what is going on in the usually uninteresting outer regions and any inaccuracies arising out of this inevitably reduces the amount of useful information that can be extracted from the later analysis of the inner region of interest. Subtractive interferometry eliminates the need for this unnecessary analysis of the outer region and so greatly improves the accuracy of the investigation.

CHAPTER 8

SUMMARY, POTENTIAL DEVELOPMENTS AND APPLICATIONS

Various methods of making lens holograms have been described, their imaging properties discussed theoretically, and their practical use successfully demonstrated.

Developments in the field of holographic optical elements will lie in improved methods of manufacture. Figure 8.1 illustrates a possible method of making particularly good quality point holograms. The method depends on the availability of an unbacked, high resolution and transparent emulsion of good optical quality. It would have the great advantage of requiring the minimum of optical components, and by using a very small pin-hole the quality of the diverging lens does not have to be very good. The quality of the resulting hologram is limited by the quality of the mirror behind the photographic plate.

From an applications point of view, it is conceivable that if the efficiency of holographic optical elements can be sufficiently increased by, for example, suitable processing to form phase holograms, they may become a general replacement for conventional optical elements. At present they are most likely to become useful replacements for the more expensive optical

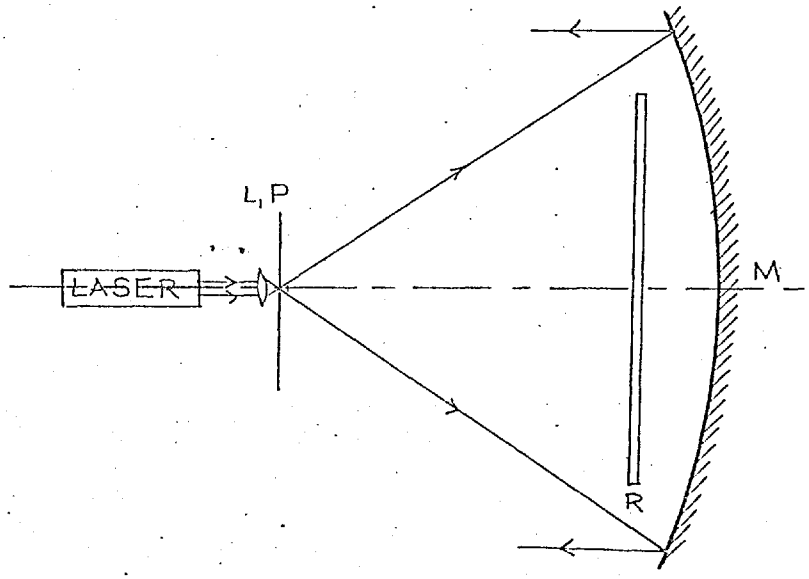

Optical arrangement for making a point hologram using a transparent unbacked photographic plate

FIGURE 8.1

components (e.g. large aperture schlieren lenses) that are used in conjunction with bright laser sources. The output from such a source is more than sufficient to compensate for the inefficiencies of the lens holograms. Their cheapness of construction also makes tham particularly suited for use in optical systems used for studying unconfined explosions. The possibility of making lens holograms of extremely large aperture could provide a means of studying the very large test sections encountered in some wind tunnel experiments: in this case the hologram could be made in situ on the windows of the wind tunnel.

The theoretical basis of a method of measuring the velocity of phase and solid objects, based on the application of schlieren-interferometry and the Doppler effect has been proposed, described in detail, and verified experimentally.

An obvious extension of the Doppler velocity method is the measurement of the velocity of solid objects moving through phase objects. Apart from having to take into account the effects that schlieren deflections have on the direction of the scattered light the effect of possible fluctuations in the phase of the transluminating beam will have to be eliminated.

The most useful application of the Doppler velocity method will be in the study of moving phase objects as it is simpler, has better spatial resolution, and is more convenient than most other available techniques (e.g. streak photography, ionization,

pressure or temperature probes). The method has the added advantage of automatically giving the velocity component normal to the propagating refractive index gradient and is, therefore, particularly suited to the measurement of burning velocities as well as for measuring local detonation velocities. The method may be extended and applied to the study of an array of objects moving at different velocities by performing a frequency analysis of the observed beat frequency signal. This gives a measure of the velocity distribution in, for example, a stream of particles or randomly moving turbules.

It has been demonstrated that the visualization of ultrasonic waves, using shadowgraphy and a short duration argon jet spark, can be used as a diagnostic technique for measuring the temperature of gases up to almost 1000^{o}K providing the gas composition is known.

The most promising developments of the ultrasonic method will result by working at higher acoustic power densities and/or frequencies as, at present, the method seems to be limited by poor visualization at high temperatures and in certain gases due to absorption. As the sound wavefronts become distorted on entering the hot gases there is nothing to be gained by increasing the cross-sectional area of the transducer. It should be possible to operate the crystal at

higher power densities by using pulsing techniques. Not only would this eliminate the mechanical slide arrangement used, but it would also improve the synchronization of the light source which, if fired just before the end of the acoustic pulse, would reduce perturbation displacement effects. Interferometric methods of visualization may also be possible at high acoustic power densities. While this does not have the simplicity of the shadow method its insensitivity to temperature makes it particularly attractive.

The ultrasonic method has applications where solid thermometry is difficult or impossible. It is less costly experimentally and easier to interpret theoretically than spectroscopic methods. The method, if used in conjunction with a Q-switched laser light source, could be used for measuring the temperature of, for example, a highly luminous plasma jet.

The design of a relatively cheap, simple and aberration free subtractive interferometer has been described and some of its advantages demonstrated.

The ability of being able to obtain aberration free interferograms represents the achievement of perfection in interferometric experimentation. This greatly simplifies interpretation as the problem of the correction for the presence of residual fringes no longer exists. The size and shape of

the phenomenon of interest may force changes in design detail and if test sections are much larger than 7cm in width (or from the axis of symmetry) the two large aperture lenses will certainly have to be replaced by schlieren mirrors. Larger test sections may even necessitate using lens holograms. Exposure times could be shortened by partial silvering of the beam splitting elements.

As well as being able to obtain 'infinite' fringe interferograms one can, by slightly changing the direction of the reference beam between the two exposures, obtain sheared or 'finite' fringe interferograms. These are easier to interpret when studying very small refractive index changes. Apart from the usual interferometric studies the interferometer may also be used for obtaining ordinary single exposure holograms which can then be examined at leisure using conventional optical techniques. These new facilities together with the ability of being able to subtract the effects of optical defects and boundary layers will make interferometry a more versatile diagnostic tool.

APPENDIX 1

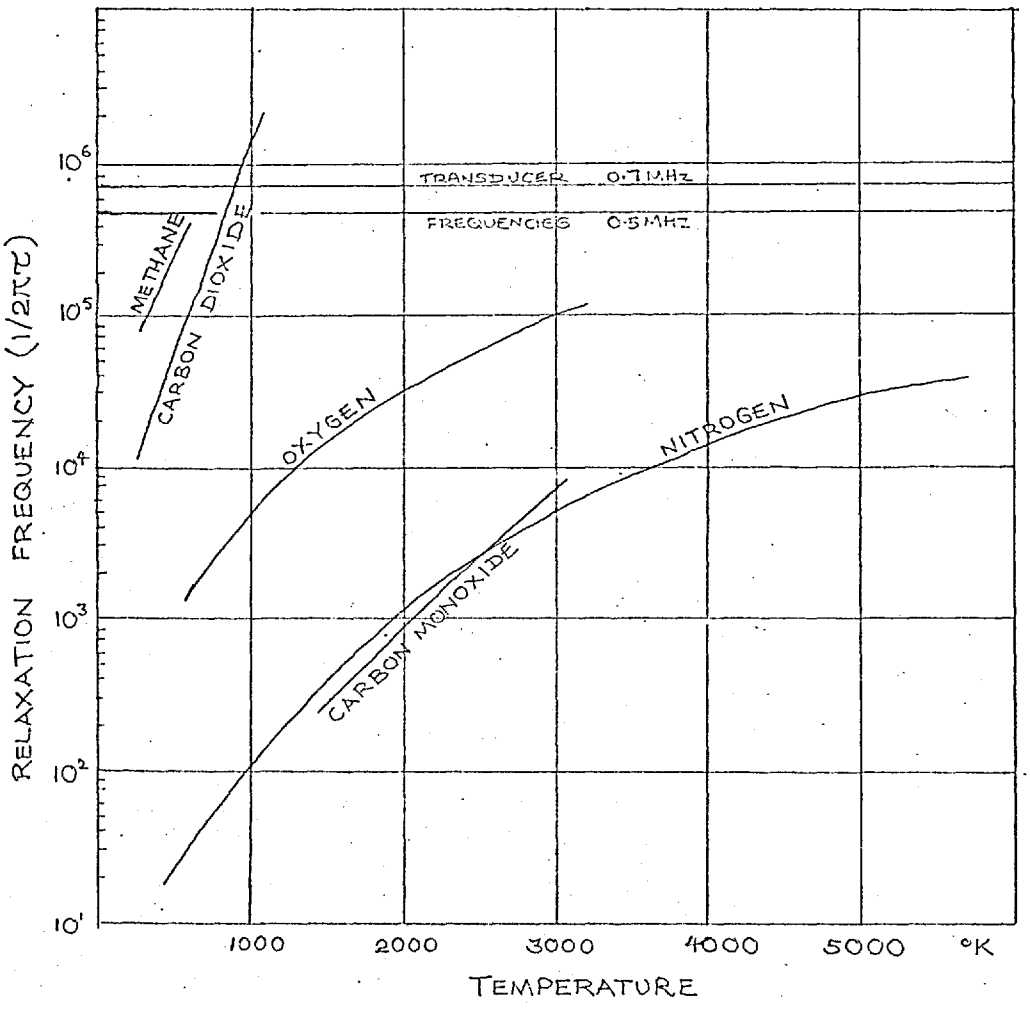

Relaxation frequency $(1/2\pi\tau)$ v. Temperature for carbon dioxide, carbon monoxide, methane, oxygen and nitrogen. (Calculated from data collected by Cottrell and McCoubrey - ref 48).

APPENDIX 2

HEAT TRANSFER COEFFICIENT v. TEMPERATURE AND GAS FLOW VELOCITY FOR 36swg WIRE IN AIR AND ARGON AT ATMOSPHERIC PRESSURE.

For Reynold numbers in the range $0.1 < Re < 1000$ the heat transfer coefficient α can be calculated using the relation[71]

$$Nu = Pr^{0.3}(0.35 + 0.47\ Re^{0.52}),$$

where

$$Nu = \alpha D/K_g$$

$$Pr = C_p \eta / Kg = 4\gamma/(9\gamma - 5)$$

$$Re = D\rho v/\eta$$

where D = diameter of wire (i.e. 1.78×10^{-2}cm), K_g = thermal conductivity of the gas, C_p = specific heat of the gas at constant pressure, ρ = density of the gas, η = viscosity of the gas.

Over the temperature range of interest here Pr and C_p may be taken to be independent of temperature. For air and argon they have the following values:

Air	Argon
Pr = 0.74	Pr = 0.67
C_p = 0.24 cal.gm^{-1}.$^{\circ}$C^{-1}	C_p = 0.12 cal.gm^{-1}.$^{\circ}$C^{-1}

When these quantities are substituted into the above expression it reduces to

$$\alpha_{air} = 16.6\eta + 2.02\eta^{0.48}\rho^{0.52}v^{0.52}$$

$$\alpha_{argon} = 9.15\eta + 0.53\eta^{0.48}\rho^{0.52}v^{0.52}$$

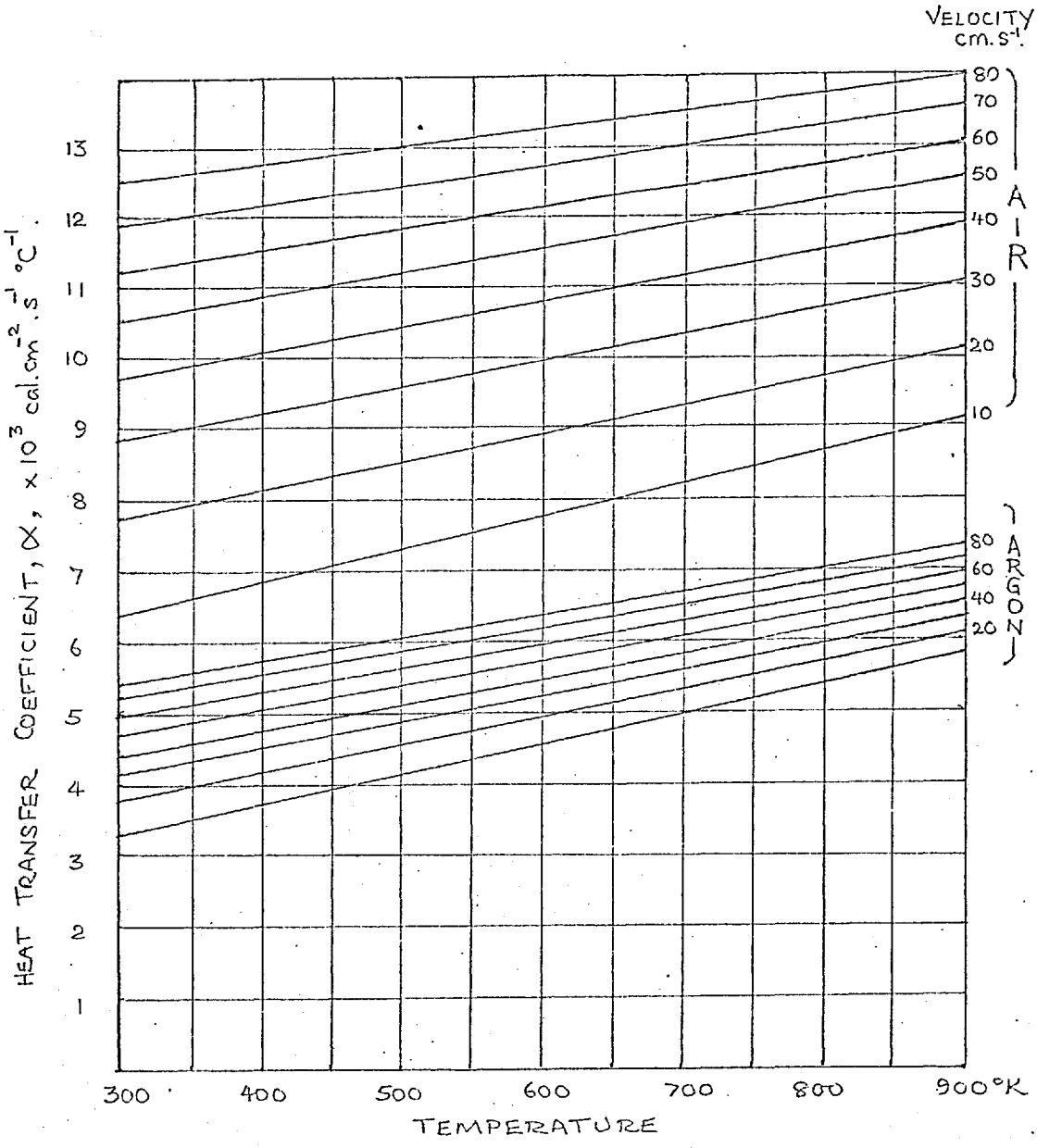

Heat transfer coefficients for 36swg wire in air and argon as a function of temperature and gas flow velocity.

APPENDIX 3

LIST OF SYMBOLS (followed by chapter number in which they are used)

a	distance between reference aperture in schlieren blind and optic axis.	3,4
A	area	5
A	aberration coefficient	2
A	distance between beam splitter and recording plane	7
A(x,y)	amplitude distribution	2
A	'pin-hole'	5
b	distance between selective aperture in schlieren blind and optic axis	3,4
c	velocity of light	3,4
c_o, c_1, c_2	velocity of light in media vacuum, 1, 2.	3,4
C	aberration coefficient	2
C(x,y)	amplitude distribution	2
C_v, C_p	specific heats at constant volume and pressure	5
C_o, C_∞	low and high frequency specific heats	5
d	distance between apertures in schlieren blind	3,4
D	aberration coefficient	2
D	dissociation energy	5
D	diameter of wire	6
d	displacement distance of sheath-flame interface	6
d	distance between interferometer beam splitters	2,7
E(x,y)	exposure distribution	2
f	focal length of lens (f_L in chapter 2 only)	3-7
f_L	focal length of lens (f all other chapters)	2
f	focal length of point hologram	2
f	fraction dissociated	5
F	aberration coefficient	2
F	force	5
G	'grid'	3,4
I	illumination	3-5
ΔI	change in illumination	5

k	reaction rate	5
K, K_g	thermal conductivity, of a gas	5,6
K	'schlieren stop'	5
l	viewing distance between screen and object	5,6
l	distance between viewing screen and reference point source	3
L	'lens'	
L_c	'collimator lens'	5
L_s	'schlieren lens'	5
L	length of thermocouple wire	6
L	difference in geometric lengths of test and reference beams	7
m	distance between viewing screen and Doppler shifted point source	3
M	magnification	3,5,6
M	number of clear rulings on grid	3
M	molecular weight	5
n	number of diffraction orders	3
n_r	refractive index of reference space	7
$n(x,y,z)$	refractive index distribution of phase object	7
$_1n_2$	refractive index (c_1/c_2)	3
$N(x,y)$	absolute fringe order number distribution	7
$N_I(x,y)$	observed " " " " ...	7
$N_d(x,y)$	absolute order number distrib. due to aberrations	7
$N_{dI}(x,y)$	observed " " " " " "	7
N	order number of interference fringes	5
N	number of observed beats in Doppler beat frequency signal	3,4
$O(x,y)$	amplitude distribution	2
p	fringe order number	4
p	pressure	5
p_i	partial pressure of ith constituent	5
p_o, p_a	reference and ambient pressures	5
$p.$	pressure disturbance	5
p_o	amplitude of pressure disturbance	5
P	acoustic power density	5,6

r,R	radius	2,5
$\triangle r$	fringe separation	2
r_h	radius of point hologram	2
r_L	radius of lens	2
R	universal gas constant	5,6
$R(x,y)$	amplitude distribution	2
s	focal spot diameter	2
s_1, s_{ob}	diameters of reference and selective apertures in schlieren blind	3,4
s_{Lt}	diameter of smallest possible selective aperture	3
S	aberration coefficient	2
S	'light source'	
S_1, S_{ob}	'reference and Doppler shifted point sources'	3,4
T	transit time of shadow past photodetector	4
T	temperature	5,6
T_o, T_g, T_w, T_x	temperature of thermocouple junction, gas, surroundings and at a point x respectively	6
T_L	temperature at end of thermocouple wire	6
$T(x,y)$	transmittance distribution	2
u	velocity of test object	3,4
$\triangle u$	uncertainty of velocity measurement	3,4
v	velocity of sound	5,6
v_o, v_∞	low and high frequency velocity of sound	5
v	gas flow velocity	6
v_e	entrainment velocity	6
v_f	fringe velocity	3
v_s	shadow velocity	3
w	radius of Gaussian laser beam	2
w_o	transluminating beam width, or distance over which velocity measurement is made	3,4
w_f	width of fringe system seen by detector	3
x,y,z	spatial coordinates	
X	viewing distance of screen from schlieren blind	3
X	depth of phase object	7
Z	thickness of acoustic beam	5

α	angle between reference beam and optic axis	3
α	maximum spatial frequency resolvable by emulsion	2
α	particle displacement attenuation coeffident	5
$\alpha, \alpha_h, \alpha_d$	viscous, heat conduction and dispersion coeff.	5
α	spatial shear fringe frequency	7
α	heat transfer coefficient	6
γ	C_p/C_v	5,6
γ	angle between velocity vector and normal to moving interface	3
δ	refractivity (n - 1)	5
δ_o	value of δ at some reference state	5
δ_{max}, δ_{min}	maximum and minimum values of δ in an acoustic beam	5
ϵ	emissivity	6
η	viscosity	5,6
θ	angle of deviation (deflection or scatter)	2-5
θ	angle between reference and test beam	7
θ_m	maximum angle between reference and object beams	2
θ_{max}	maximum angle of deflection	5
λ	wavelength of light	
λ_1	wavelength of light in medium 1	
λ^*	fringe separation	3
ν	light frequency	
ν_{ob}	observed Doppler shifted light frequency	3,4
ν_1	frequency of unperturbed light	3,4
ν_2	frequency of light observed in medium 2	3,4
ν_b	beat frequency	3,4
ν_s	sound frequency	5,6
ν_i	frequency of point of infection in sound dispersion curve	5
$\Delta\nu$	line width of radiation	2,4
ξ	particle displacement	5
ξ_o	amplitude of particle displacement	5
ξ	angle between viewing screen and parpendicular to optic axis	3

ρ	density	5,6
σ	Stephan's constant	6
τ	torsion constant	5
τ	relaxation time	5
ϕ_{ob}, ϕ_1	phase angles of light waves at S_{ob} and S_1	3
ϕ^*	resultant phase angle of wave describing moving interference fringes	3
$\phi, \phi(x,y)$	phase distribution at image plane	7
$\phi_d, \phi_d(x,y)$	phase distribution at image plane due to aberrations	7
ϕ	angle between light beam and moving interface	3
ψ	phase aberration	2
ψ	angle between two interfering beams	3
ψ	angle between incident and reflected beams	7
ω	$2\pi\nu_s$	5
Ω	angular width of selective shadow	3

REFERENCES

1. Gaydon, A. G. The spectroscopy of flames. Chapman and Hall, London, 1957.

2. Gaydon, A. G. and Wolfhard, H. G. Flames, their structure, radiation and temperature. Chapman and Hall, London, 1953.

3. Hottel, H. C. and Sarofim, A. F. Radiation transfer. McGraw-Hill, New York, 1967.

4. Chandrasekhar, S. Radiative transfer. Dover, New York, 1960.

5. Jones, A. R. and Schwar, M. J. R. High temperatre - High pressure. 1, 369, 1969.

6. Weinberg, F. J. Optics of flames. Butterworths. London, 1963.
   a) p33, b) p15, c) p156, d) p231

7. Schwar, M. J. R. and Weinberg, F. J. Combustion and Flame, 13, 335, 1969.
   a) p337, b) p339

8. Fristrom, R. M. and Westenberg, A. A. Flame structure. McGraw-Hill, New York, 1965.

9. Bonne, U., Grewer, Th. and Wagner, H. Z. phys. Chem. Frankf. Ansg. 26, 93, 1960.

10. Dixon-Lewis, G. and Isles, G. L. 8th Symposium (Int) on combustion. p448. Williams and Wilkins, Baltimore.

11. Dixon-Lewis, G. and Isles, G. L. Proc. Roy. Soc. A., 308, 517, 1969.

12. Gabor, D. Nature, 161, 777, 1948.

13. Lieth, E. N. and Upatnieks, J. J. Opt. Soc. Am., 52, 1123, 1963.

14. DeVelis, J. B. and Reynolds, G. O. Theory and Applications of holography. Adison-Wesley, New York, 1967.

15. Smith, H. M. Principles of holography. Wiley-Interscience, New York, 1969.

16. Stroke, G. W. Introduction to coherent optics and holography. Academic Press, New York, 1966.

17. Rogers, G. L. Proc. Roy. Soc. Edin. A. 63, 193, 1952.

18. Meier, R. W. J. Opt. Soc. Am., 55, 987, 1965.

19. Schwar, M. J. R., Pandya, T. P. and Weinberg, F. J., Nature, 215, 239, 1967.

20. Kogelnik, H., and Li, T. Appli. Opt., 5, 1550, 1966.

21. Longhurst, R. S. Geometrical and physical optics. Longmans, London, 1957.

22. Emsley, H. H. Aberrations of thin lenses. Constable, London, 1956.

23. Holder, D. W., and North, R. J. Schlieren methods. H. M. S. O., 1963.

24. Leith, E. N. and Upatnieks, J. AFIP SPRING Joint Computer Conf, 28, 43, 1966.

25. Horman, M. H. and Chau, H. H. M. Appl. Opt., 6, 317, 1967.

26. Horman, M. H. Appl. Opt., 6, 1415, 1967.

27. Horman, M. H. Appl. Opt., 6, 2011, 1967.

28. Doppler, C. J. Böhm. Gesell. Abh., 2, 465, 1842.

29. Fizeau, H. L. Comptes Rendus, Paris, 29, 90, 1949.

30. Tolansky, S. High resolution spectroscopy. Methuen, London, 1947.

31. Ramsden, S. A. and Davies, W. E. R. Phys. Rev. Lett., 13, 227, 1964.

32. Yeh, Y. and Cummins, H. Z. Appl. Phys. Lett., 4, 176, 1964.

33. Foreman, J. W., George, E. W. and Lewis, R. D. Appl. Phys. Lett., 7, 77, 1965.

34. Lewis, R. D., Foreman, J. W., Watson, H. J., and Thornton, J. R. Phys. of Fuids (U.S.A) 61, 433, 1968.

35. Goldstein, R. J., and Hagan, W. F. Phys. of Fluids (U.S.A) 10, 1349, 1967.

36. Pike, E. R., Jackson, D. A., Bourke, P. J. and Page, D. I. J. Sci. Instrum (J of Phys E) 1, 727, 1968.

37. Rudd, M. J. J. Sci. Instrum (J of Phys. E) 2, 55, 1969.

38. Schwar, M. J. R. and Weinberg, F. J. Nature, Lond. 221, 357, 1969.

39. Schwar, M. J. R. and Weinberg, F. J. Proc. Roy. Soc. A. 311, 469, 1969.

40. Born, M. and Wolf, E. Principles of optics. Pergamon Press, Oxford, 1965.
a) Chp 10, p491, b) p264

41. Lengyel, B. A. Introduction to laser physics. J.Wiley, New York, 1966.

42. Mayer, A. M. Phil. Mag. 45, 18, 1873.

43. Suits, C. G. Temperature: Its measurement and control in science and industry. Reinhold, New york, 1956, p720.

44. Edels, H. and Whittaker, D. Proc. Roy. Soc. A., 240, 54, 1957.

45. Marlow, D., Nisewanger, C. and Cady, W. J. Appl. Phys., 20, 771, 1949.

46. Hedrich, A. L. and Pardue, D. R. Temperature: Its measurement and control in science and industry. Vol II. Reinhold, New York, 1955, p383.

47. Carnevale, E. H., Poss, H. L. and Yoss, J. M. Temperature: Its measurement and control in science and industry. Vol III, part 2 (Applied methods and intruments) Reinhold, 1962, p959.

48. Cottrell, T. L. and McCoubrey, J. C. Molecular energy transfer in gases. Butterworths, London, 1961.
a) p7, b) p10, c) pp13-18, d) p17, e) p19

49. Roberts, J. K. and Miller, A. R. Heat and thermodynamics. Blackie, London, 1958, Chp. IV.

50. Thorpe, P. L. J. of Phys. E., 2, 1073, 1969.

51. Poritsky, H. and Suits, C. G. Physics, 6, 196, 1935.

52. Bergmann, L. Ultrasonics. Bell, London, 1938.
a) p129

53. Saha, M. N. and Srivastava, B. N. A treatise on heat. The Indian Press, Allahabad, 1958. p175.

54. Wood, A. B. A textbook of sound. Bell, London, 1957.
a) p55, b) p54, c) p294, d) p467, e) p409B

55. Richardson, E. G. Ultrasonic physics. Elsevier, Amsterdam, 1952.
a) p37, b) p14.

56. Arnold, J. W., McCoubrey, J. C. and Ubbelohde, A. R. Proc. Roy. Soc. A., 248, 445, 1958.

57. Naugolnykh, K. A. Sov. Phys. Acoustics, 4, 115, 1958.

58. Carlin, B. C. Ultrasonics. McGraw-Hill, New York, 1960.
a) pp38-136, b) pp137-141

59. Medwin, H. J. Acoust. Soc. Am., 26, 332, 1954.

60. Toepler, M. Ann. Phys. Lpz. (IV) 27, 1043, 1908.

61. Tawil, E. P. C.R. Acad. Sci. Paris. 191, 92 & 168, 1930.

62. Pohlmann, R. Naturwiss, 23, 511, 1935.

63. Bergmann, L. and Goehlich, H. J., Phys. Z. 38, 9, 1937.

64. Hubbard, J. C., Zartmann, I.F. and Larkin, C. R. J. Opt. Soc. Am., 37, 832, 1947.

65. Hilsenrath, J et als(9). Tables of thermodynamic and transport properties of air, argon, carbon dioxide, carbon monoxide, hydrogen, nitrogen, oxygen, and steam. Pergamon, Oxford, 1960.

66. Keenan, J. H. and Kaye, J. Gas tables. Thermodynamic properties of air, products of combustion and component gases. Wiley, London, 1956.

67. Mason, W.P.(ED). Physical acoustics, Vol IIB. Academic Press, New York, 1964.

68. Weinberg, F. J. Geometric optical techniques in combustion research. Progress in combustion science and technology. Vol I. Pergamon, Oxford, 1961.

69. Smith, R. W., Edwards, H. E., and Brinkley, S. R. Rept. of investigations 4938. U.S. Dept. of the interior, Bureau of mines. Jan 1953.

70. Knudsen, V. O., and Ficke. E. F. J. of Acoust. Soc. Am., 10, 89, 1938.

71. McAdams, W. H. Heat Transmission. McGraw-Hill, London, 1951. p222.

72. Kaskan, W. E. Sixth symposium (INT) on combustion. Reinhold, New York, 1957, p134.

73. Heflinger, L. O., Wuerker, R. F. and Brooks, R. E. J. Appl. Phys., 37, 642, 1966.

74. Tanner, L. H. J. Sci. Inst., 43, 346, 1966.

75. Leith, E. N. and Upatnieks, J. J. Opt. Soc. Am., 53, 1377, 1963.

76. Kay, G. W. C. and Laby. T. H. Tables of physical and chemical constant, 13th edition. Longmans, London, 1966.